Fracture of graphite under different stress conditions

Rose, A. P. G.

Award date:
1985

Awarding institution:
University of Bath

FRACTURE OF GRAPHITE UNDER DIFFERENT STRESS CONDITIONS

submitted by A.P.G. Rose
for the degree of Ph.D.
of the University of Bath

1985

ACKNOWLEDGEMENTS

This work has been carried out as a collaborative programme between the Berkeley Nuclear Laboratories of the Central Electricity Generating Board (CEGB) and the School of Materials Science, University of Bath. The author wishes to thank the CEGB for permission to publish this thesis and both bodies for providing laboratory facilities.

The following people are gratefully acknowledged.

Dr. M.O. Tucker for providing valuable ideas, assistance and encouragement throughout the project.

Dr. R.G. Cooke and Dr. B. McEnaney for contributions to useful discussions reviewing progress.

Mr. D.D. Jones for providing skilled technical support.

Miss L.S. Field for assistance with the computing techniques used in Chapter 6.

Finally I wish to thank my wife for keeping me to the discipline required to write this thesis and Mrs. E.A. Fisher for her accurate typing of the manuscript.

ABSTRACT

This work is directed towards establishing a general fracture criterion for graphite bodies. Initially a three-dimensional model is developed based on Linear Elastic Fracture Mechanics and micro-structural information. It assumes fracture to occur when a critical defect is formed by a statistical process of cleavage of contiguous, randomly orientated particles under an external stress. The model is applied to results of bend and tensile tests performed on pitchcoke and IM1-24 graphites. Theoretical bend strengths agree well with experiment but tensile strengths are over-predicted.

In components of complex geometry, the distribution of stress is normally only obtainable from two-dimensional finite element analysis. Therefore a simplified two-dimensional model is developed. This simplification gives good agreement with both bend and tensile results. Further, data from the literature is used to test the simplified model in a wide range of stress conditions.

The bend strengths of pitchcoke beams containing sharp notches are also measured. Again agreement with the two-dimensional model is good. Thus for the first time one model describes fracture in both sharply notched and un-notched beams. Also, a reliable method of determining the critical stress intensity factor K_{Ic}, from notched or un-notched beams is developed.

Results of bend tests on curved beams of pitchcoke graphite irradiated to doses in the range 0.4 - 1.6 x 10^{21} neutrons/cm^2 (DNE) in an Advanced Gas-Cooled Reactor are reported. A method of measuring dynamic Young's modulus of these non-standard specimens is developed. Half the specimens are annealed at 2350^{o}C prior to testing to separate the effects of fast neutron irradiation and radiolytic oxidation. The two-dimensional model is used to predict the effect of fast neutron

irradiation alone on mean failure stress.

Finally, achievements are summarised and further experimental and theoretical work is suggested.

FRACTURE OF GRAPHITE UNDER DIFFERENT STRESS CONDITIONS

CONTENTS

CHAPTER 1

INTRODUCTION

Brocklehurst (1974) begins his authoritative review 'Fracture of Polycrystalline Graphite' with the following sentence. 'One of the outstanding technological problems in engineering designs incorporating graphite components is an adequate quantitative description of the failure criteria under general states of loading'. Although progress has been made towards a solution in the intervening ten years the problem remains.

This thesis considers graphite fracture primarily in nuclear grade materials. Tensile stresses are almost invariably responsible for fracture as graphite is a brittle material with a uniaxial compressive strength three to four times that in tension. Bearing this in mind this work has involved a wide range of laboratory tests under different tensile and bend stress conditions, complemented by results reported in the literature. A model of fracture has been developed and its performance compared with experiment as widely as possible. The majority of work has been carried out on unirradiated graphite. It is only through a sound understanding of virgin properties that changes in fracture behaviour on irradiation may be understood. In a later chapter, results of irradiation experiments performed by the author at Berkeley Nuclear Laboratories are reported and the new fracture model used to explain the observed behaviour.

The extensive literature, reviewed in Chapter 2, is evidence for the many attempts to define a failure criterion for graphite. Simple conditions such as a maximum normal stress theory are over-pessimistic in the presence of a stress gradient when the maximum stress at failure is much greater than the uniaxial strength. A criterion of critical strain energy at fracture fits tensile and

four-point bend strength results well but in tests where there is a stress gradient in more than one direction such as in three-point bend there is a difficulty in defining the volume over which strain energy is summed. The Weibull statistical theory can predict the dependence of strength on volume for large specimens in bend and tension but as it has no physical basis it is unsuited for general application. Fracture mechanics techniques are successful when an artificial defect much larger than the maximum coke particle size is present such that fracture is confined to the main crack. For un-notched or shallow notched beams, much secondary cracking occurs before final failure. Consequently there is significant uncertainty in the size of the critical defect at failure. Buch (1976) in a novel theory based on Linear Elastic Fracture Mechanics (LEFM) has overcome this problem in un-notched beams by first defining the critical defect size (from the material fracture toughness and the applied stress) and then considering formation of such a defect. The treatment is based on the weak bonding between basal planes in graphite crystals. The graphite is assumed to consist of discrete particles which may cleave and link up under appropriate loading. At a given applied stress there is a particular probability of an array of contiguous cracked particles attaining the critical size and consequently a given probability of failure. Using this approach Buch had considerable success in predicting the uniaxial tensile strength of a wide range of graphites.

All the failure criteria mentioned above have been applied to the results of laboratory tests with varying degrees of success. However, their extension to predict lifetimes and failure probabilities of actual components has not been achieved. Loading arrangements and component geometry are usually more complicated

than experienced with laboratory test pieces. Further, in a nuclear reactor significant changes in graphite properties occur as a result of the neutron flux and the local environment. Internal stresses are induced by dimensional changes, differential thermal expansion and irradiation-induced creep. Young's modulus and strength are concurrently increased by neutron bombardment and decreased by radiolytic oxidation by carbon dioxide in the coolant. These changes, discussed fully in later chapters, add to the complexity of the task.

To illustrate the type of problem to be tackled consider two cases of component performance encountered in Civil Advanced Gas-Cooled Reactors (CAGR).

Cylindrical graphite sleeves approximately one metre in length and twenty-five centimetres diameter surround the thirty-six pin fuel cluster in each CAGR fuel element. The elements are stacked in columns of eight which together with ancillary attachments form a fuel stringer. Each reactor contains over three hundred stringers which during normal operation sit throughout the core in individual fuel channels. The sleeve separates hot from cold gas and enables an efficient re-entrant gas flow to operate. This involves cold gas at approximately 350^{o}C passing downwards outside the fuel stringer while inside, gas passes upwards over the fuel reaching a maximum temperature of approximately 650^{o}C at full reactor power. The temperature gradient across the sleeve gives rise to differential thermal expansion which puts the inside of the sleeve in compression and the outside in tension. These stresses are rapidly relieved by the primary component of irradiation creep (Kelly and Brocklehurst, 1977). However, on discharge of the stringer during refuelling the outside of the sleeve is subjected to the hot gas temperature and a

CHAPTER 2

LITERATURE REVIEW

This chapter is included to provide background information and to point out achievements and shortcomings of previous work. The discussion is limited to unirradiated graphites but is extended in Chapter 7 to cover changes on fast neutron irradiation. Initially, very brief comments on deformation mechanisms in single and polycrystals are made to set the scene for detailed criticism of various fracture criteria proposed in the literature. Then a survey of experimental techniques used in study of graphite fracture is carried out. The chapter is concluded with an assessment of current knowledge and identification of areas to which this thesis contributes.

2.1 Deformation Mechanisms

2.1.1 Single crystals

Comprehensive reviews of deformation mechanisms in graphite have been published by Jenkins (1973), Brocklehurst (1974) and Kelly (1981). In each case they underline the dependence of the mechanisms on the very marked anisotropy of graphite crystals, especially in the single crystal elastic constants. The hexagonal symmetry present enables the elastic response of the crystal to be described by five independent stiffness constants defined in relation to two directions, parallel (a-axis) and perpendicular (c-axis) to the basal plane. Following convention, the a-axis is termed '1' and the c-axis '3'. The orthogonal '1' and '2' directions define the basal or 'a' plane. Values of single crystal constants obtained by experiment (Kelly, 1981) are shown in Table 2.1. It is interesting to compare these with a typical value of 10^{10} Pa for the Young's modulus of polycrystalline graphite. Constants C_{11} and C_{12}, related

Table 2.1

Single Crystal Elastic Constants Determined

from Experiment (Kelly, 1981)

Stress component = C_{ij} x strain component.

	STIFFNESS ($\times 10^{10}$ Pa)
C_{11}	106 ± 2
C_{12}	18 ± 2
C_{13}	1.5 ± 0.5
C_{33}	3.65 ± 0.10
C_{44}	0.01 - 0.45*

* True value is between 0.4 - 0.45 x 10^{10} Pa but is drastically reduced by the presence of basal plane dislocations.

to Young's modulus and Poisson's ratio respectively parallel to the 'a' plane, are high being solely determined by the covalent bonding within the basal plane. Constants C_{33}, the Young's modulus in the 'c' plane and C_{44}, the shear modulus in the 'a' plane are much lower as they are a function of the weak interlayer forces. The fifth independent constant C_{13}, a Poisson's ratio effect in both 'a' and 'c' planes is influenced by both forms of bonding. As temperature rises all the crystal modulii decrease, C_{33} and C_{44} the most rapidly as the layer planes move further apart.

Kelly (1981) has reviewed the character of dislocations found in the graphite lattice. In pure unirradiated graphite all experimentally observed dislocations lie in the basal plane and are separated into partial dislocations. They may be edge or screw type and may combine according to reactions of the type

$$\frac{a}{3}[10\bar{1}0] + \frac{a}{3}[1\bar{1}00] \rightarrow \frac{a}{3}[2\bar{1}\bar{1}0].$$

These dislocations provide an easy mechanism for slip on two independent slip systems. Non-basal plane dislocations of Burgers vector $\frac{c}{2}[0001]$ are seen on irradiation. They are formed by interstitial and vacancy loops resulting in stacking faults in the basal plane. Other dislocation loops with a component of Burgers vector in the c-direction have been observed distributed uniformly in boron doped single crystals and near twist boundaries and twins in Ticonderoga flake crystals (Turnbull and Stagg, 1966). Roscoe and Thomas (1966) have used optical microscopy to study large arrays of non-basal plane dislocations forming tilt boundaries. The exact contribution of these various defects to deformation behaviour is not established quantitatively but at room temperature plastic deformation occurs readily in single crystals making them extremely prone to damage during handling.

2.1.2 Polycrystals

The mechanical behaviour of polycrystals may be controlled to a greater or lesser extent by single crystal properties depending on the degree of graphitisation and the size and orientation of graphite crystallites. Nuclear grades are typically well graphitised with crystallites ranging from a few Ångstroms to coke particles which are effectively single crystals up to perhaps 1-2 mm in size. If a random distribution of basal poles in spherical crystals is present then isotropic bulk properties will result. However, if the microstructure consists of preferentially aligned acicular crystals, strength and Young's modulus may be up to twice as large parallel to the basal planes as in the perpendicular direction.

There are many theories summarised by Kelly (1981) relating the elastic constants of polycrystalline aggregates to single crystal values. Problems encountered in the general application of these theories (Jenkins, 1973) are

(i) varying degrees of bulk anisotropy,

(ii) distribution of crystal sizes and basal plane spacing variations,

(iii) amount and distribution of porosity,

(iv) intercrystalline carbon-carbon atom bonding which may negate the importance of single crystal properties.

Despite much careful work, reviewed in detail by Brocklehurst (1974), there is no complete description of the deformation mechanisms involved prior to final fracture. Nevertheless, several comments may be made. The stress-strain curve of polycrystalline graphite is non-linear. On removal of the load a permanent set remains which can be recovered on annealing at greater than 2000°C.

The elastic modulus decreases with increasing stress and on reloading a hysteresis effect is observed with energy lost by damping. Fracture is essentially brittle with upwards of 80% of the deformation being elastic, this proportion increasing with neutron irradiation.

As reviewed by Kelly (1981) many workers have seen glissile dislocations within the basal plane which provide an easy mechanism for slip on two independent systems. However, this is less than the five independent slip systems required for ideal plastic flow in a polycrystal (von Mises, 1928). With irradiation or thermal activation dislocation climb processes may operate but there are still insufficient slip systems for plastic flow. Green et al. (1970) in formulating a theory of creep in polycrystalline graphite at temperatures greater than 2000^{o}C deduced that plastic deformation based on slip alone could not explain observed behaviour but rather, almost all the creep occurs by the opening up of many small cracks. Even at ambient temperature microcracking is an important deformation mechanism. It accounts for most of the decrease in elastic modulus with prestress at high stress levels although at lower stresses there may be a contribution from increased dislocation density (Brocklehurst, 1974). The recovery in modulus on annealing occurs by healing of stress induced microcracks such that the material displays a memory for its original state. Further, the modulus increases by 10-15% at 1000^{o}C and reaches a maximum of 30-40% greater than the room temperature value at 2000^{o}C (Price, 1975) despite the single crystal modulii all decreasing with temperature. Again this increase is due to microcrack closure, in this case the cracking arising from anisotropic crystal contraction from the graphitisation temperature (Mrozowski, 1956). In an inert atmosphere strength increases with temperature by up to 50% at 2000^{o}C. The mechanisms

proposed for this increase are relief of internal stress and increase in plasticity (Brocklehurst, 1974). Green (1951) has reported an increase in the fatigue limit with increasing temperature.

The microcrack lengths vary in accordance with the distribution of particle sizes present and are of a similar nature to microcracks seen in ceramics (Hoagland et al., 1975; Evans, 1976; Cooke, 1978). From an early stage in deformation, dislocation pile-ups at obstacles such as grain boundaries or impurity particles are expected. These pile-ups may nucleate cracks or may extend pre-existing flaws. Additionally, microcracks may develop according to the Griffith (1920) elastic energy balance criterion. It is likely that a combination of dislocation and Griffith cracking mechanisms is operative, the result being cleavage on the planes of lowest surface energy - that is the basal planes. Many studies, summarised in section 2.3.3, of these microcracks have been reported in the literature. It is clear that there is much sub-critical cracking in a polycrystal from early in a fracture test. The growth of the final failure crack involves the creation of a continuous path by breaking the bridges between microcracks by the lowest energy route. These bridges contribute significantly to the fracture resistance of polycrystalline graphite.

2.2 Failure Criteria

The deformation processes in polycrystalline graphite emphasise the importance of the inhomogeneous microstructure in determining fracture behaviour. Many suggested failure criteria treat graphite as a continuum. This may be adequate in specific simple cases but is inaccurate in complex stress systems encountered in engineering components. The various approaches are now discussed.

2.2.1 Maximum normal stress

This criterion states that failure will occur when the uniaxial tensile or bend strength is exceeded in any part of the structure. It is simple and commonly used e.g. Yahr et al., (1973); Tucker and Webster, (1982). A difficulty is encountered in that there is no unique tensile or bend strength of any graphite but both quantities are size (Brocklehurst, 1974), strain rate (Smith, 1964; Bazaj and Cox, 1969), temperature (e.g. Price, 1975) and environment (Diefendorf, 1959; Rowe, 1962; Logsdail, 1968) dependent. Considering size effects alone, data given by Darby (1978) shows that use of a lower limit bend strength as a failure criterion may lead to underestimates of failure stress in other bend tests of more than 25%. This is an example of the general point that stress at failure increases with severity of stress gradient although no simple relation exists. On the other hand, Jortner (1972) has found that the strength in biaxial tension of fine grained AXF-5Q graphite is approximately 15% less than the uniaxial tensile strength. The maximum normal stress criterion is useful when actual components are tested under simulated service loading (e.g. Metcalfe, 1982). However, this is expensive and frequently impracticable.

2.2.2 Maximum normal strain

In a similar manner to stress, a critical strain at failure may be defined. However, similar objections apply. Examination of tensile data from groups of identical samples show larger standard deviations for fracture strains than fracture stresses (Price, 1975) thereby lessening the precision of the strain criterion. Furthermore, a constant strain criterion implies higher strength in biaxial tension which is contrary to observation. There is evidence that failure occurs at constant strain before and after thermal oxidation (Kelly,

1981) but overall there is little justification for a maximum normal strain criterion.

2.2.3 Maximum shear stress (Coulomb, Tresca or Mohr criterion)

Uniaxial compression tests often give shear type failure with the fracture plane inclined to the applied stress (Gillin, 1967; Taylor et al., 1967). Shear of basal planes leading to dislocation pile-ups can nucleate cracks but subsequent crack growth is likely to depend on tensile stresses. Broutman et al. (1970) and Jortner (1972) have obtained good agreement with a maximum shear stress condition for biaxial failure results in the tension-compression quadrant of the failure envelope. Generally, the shear strength is found to be greater than half the uniaxial tensile strength and hence it must be assumed that resistance to shear is increased by friction between the shear planes. Although there is evidence for shear deformation the same objections as for maximum normal stress apply to any universal criterion based on shear.

2.2.4 Maximum stored strain energy

The stored strain energy density U, in a tensile specimen is

$$U = \sigma^2/2E \qquad (2.1)$$

where σ is the applied stress and E is the static Young's modulus. Brocklehurst and Darby (1974) proposed that fracture occurs in other tests when the average strain energy density over the region of tension is equal to this value. Results from four-point bend and internal pressure tests on thin-walled cylinders where there is a stress gradient only in the direction of crack propagation agree well with this criterion. However, the three-point bend test presents difficulties in defining the extent of the volume over which the averaging should be performed as there is also a stress gradient perpendicular to the crack growth direction.

An earlier maximum strain energy theory (Ely, 1968) gave good agreement with failure data from tubular specimens under biaxial stress but this treatment is not as versatile as that of Brocklehurst and Darby.

2.2.5 Weibull theory

The statistical analysis most often employed in the fracture of brittle solids is due to Weibull (1951). It assumes a homogeneous material containing a random distribution of flaws of varying size. When subjected to a tensile stress, strength is controlled by a combination of the highest local stress and the largest flaw. Thus it is frequently termed the 'weakest link' theory.

The probability of survival $S(\sigma)$ of a small volume element under a tensile stress σ is assumed to be of the form

$$\ell n\ S(\sigma) = - \left(\frac{\sigma - \sigma_\alpha}{\sigma_o} \right)^m$$

where σ_α is the stress below which failure probability is zero, σ_o is a normalising parameter obtained from the mean failure stress and m, the Weibull modulus is a homogeneity factor characteristic of the material (high values of m indicate a greater uniformity in the crack distribution). Values of these three parameters are obtained from experiment. The failure probability P, of the bulk specimen is then

$$P = 1 - \exp \int_V \ell n\ S(\sigma)\ dV \qquad (2.2)$$

where V is the specimen volume.

The most comprehensive testing of the theory against experimental data for nuclear graphite has been by Price (1976) and Brocklehurst and Darby (1974). Both investigations found that m was not a material property as predicted for a Weibull solid, lower values ($m \sim 9$) being found in tensile tests than in bend tests

($m \sim 16$). Price concluded that the cumulative strength distribution of his series of more than two thousand tensile and four-point bend tests could be fitted equally well by a normal (Gaussian) distribution or a Weibull distribution.

Brocklehurst (1976) has investigated the effect of specimen volume on tensile and four-point bend strength of IM1-24 graphite. Experimental results are shown in Figure 2.1, each point representing the mean and standard deviation of six samples. The drop in strength at low specimen volumes indicates a particle size effect such that sections of less than approximately ten particles across are unrepresentative of bulk behaviour. According to Weibull, either strength will decrease with increasing volume or if the maximum flaw is certainly sampled, strength will remain constant. The tensile data of Figure 2.1 tend to support the latter and the bend data the former but either alternative if applied equally to both tension and bend predicts a constant tension/bend strength ratio. The figure shows that the experimental tension/bend ratio is not unique but varies from approximately 0.5 at low specimen volumes to 0.8 at the highest volumes tested. With $m = 16$ Weibull theory predicts a value of 0.8 at all volumes. In addressing this problem Ho (1979) has added a fourth parameter, the maximum particle size, to the Weibull theory to account for the decrease in strength at small specimen volumes. An approach to explain the observed ratios using the couple-stress theory of elasticity (Tzung et al., 1981) is considered further in Chapter 4 of this thesis.

The attraction of the Weibull theory is that it may be incorporated into engineering design assessment using finite element calculations (Batdorf and Crose, 1974; Cords et al., 1977). However, its fundamental problem is lack of consistency in empirical parameters

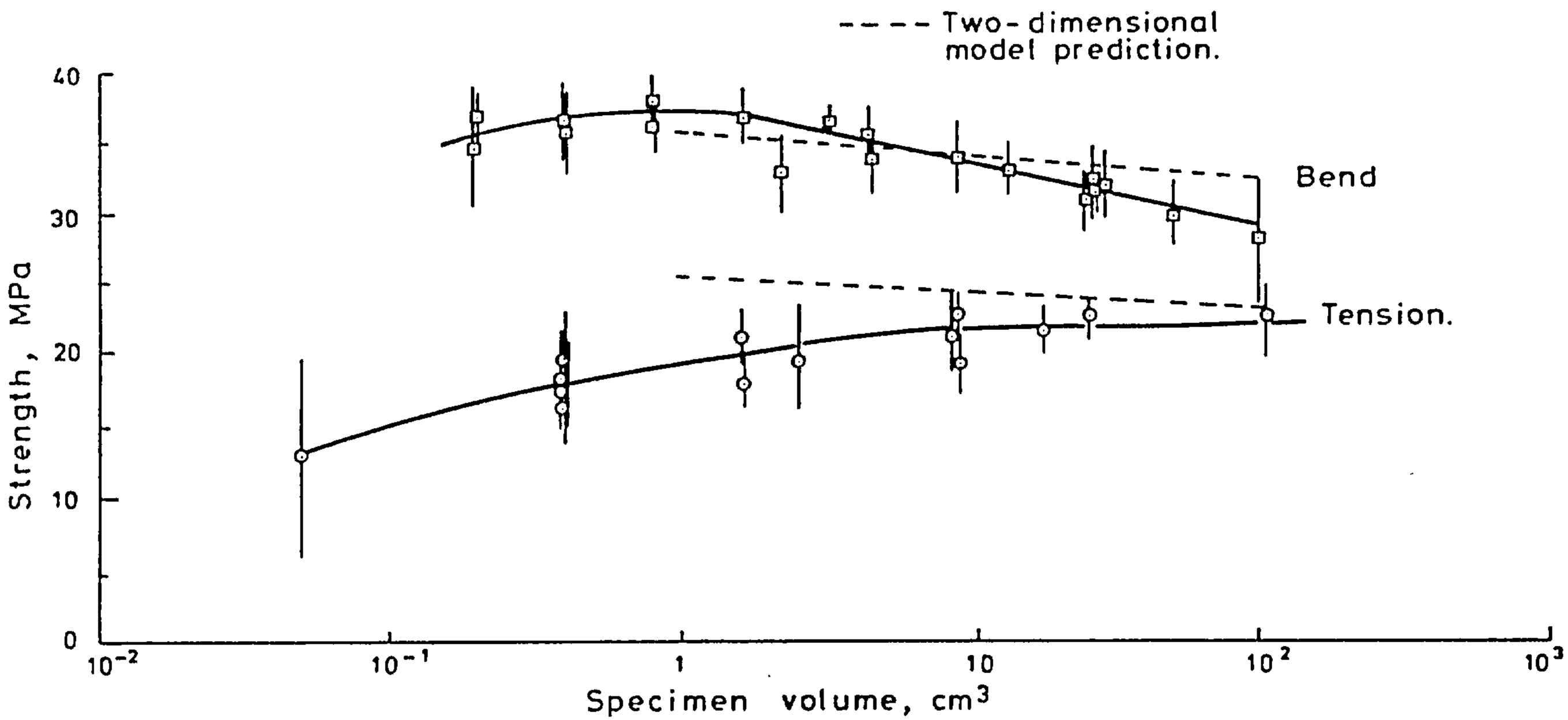

Figure 2.1: The effect of specimen volume on strength of IM1-24 graphite (i) rectangular beams in 4-point bend with varying span and (ii) cylindrical tensile specimens of diameters 2.5 → 30 mm. Also shown are the two-dimensional model failure predictions (Chapter 5).

for any one material under different stress conditions.

2.2.6 Linear elastic fracture mechanics

The methods of LEFM (e.g. Liu, 1982) are used to predict the nominal stress levels at which a sharp crack in a material propagates and causes brittle failure. For conditions of plane strain, under which a crack most easily propagates, the basic equation relating the fracture stress σ, to the critical crack size c, in a specimen of depth h is

$$\sigma = K_{Ic}/[f(c/h)\sqrt{\pi c}] \qquad (2.3)$$

where the form of the function f(c/h) depends on the loading geometry and K_{Ic} is a material property known as the critical stress intensity factor. The subscripts denote simple tensile crack opening and the critical value of K at failure respectively.

An extensive series of fracture mechanics tests on ATJ and AXM graphites (both listed in Table 3.2) was performed by Yahr and Valachovic (1972). They defined a parameter K_c calculated according to an equation of the form of (2.3) and assessed its dependence on notch sharpness and test geometry to deduce the lower limit K_{Ic}. Values of K_c decreased as the notch root radius decreased, the sharpest notches being induced by tapping the specimen with a chisel. Sharply notched beams and compact tension specimens gave valid determinations of K_{Ic} but geometrical conditions on notch and specimen sizes were different for each material. K_{Ic} was determined as 1.3 MPa $m^{\frac{1}{2}}$ for fine grained isotropic AXM, and for ATJ 0.8 MPa $m^{\frac{1}{2}}$ parallel and 0.9 MPa $m^{\frac{1}{2}}$ perpendicular to the moulding direction.

Sato et al. (1978) measured the temperature dependence of K_{Ic} in four reactor graphites using a diametral compression test on a centrally slotted circular disc. Tensile failure occurred from the slot to the outside diameter. At 2000°C a 50% increase in failure stress

and critical stress intensity factor compared with room temperature values was obtained in each case.

Rodig et al. (1978) investigated the effect of specimen volume, material anisotropy and multiple loading on K_c. It was found that K_c increased with specimen volume which is opposite to the behaviour observed in metals. The effect is due to more secondary cracking away from the main failure crack and hence a greater energy dissipation the larger the specimen. A further important conclusion reached was that for any graphite at ambient temperature a high uniaxial strength does not necessarily produce a corresponding increase in K_{Ic}, that is fine grain graphites are more sensitive to small defects. Hence the work of Rodig et al. illustrates that a failure criterion based on LEFM alone is inadequate.

Tucker (1979) concluded on the basis of experimental notched beam tests that fracture mechanics theories are successful when the specimen notch depth is large compared with the maximum coke particle or pore size. In attempting to find a more universal application of LEFM, Corum (1967) introduced the idea that the effective crack depth in a notched specimen is greater than the initial machined notch depth by an 'inherent' defect length equal to that of the largest pore present. Marshall and Priddle (1973a) used this approach to predict the tension/bend strength ratio of reactor graphites. However, they predicted the ratio to tend to unity in large specimens which is contrary to observation. Buch (1982) presented a theory considering the LEFM of surface flaws in conjunction with a distribution of surface flaws present but this suffers from exactly the same limitation.

Many authors use equations of the form of (2.3) with known σ and K_{Ic} to determine the critical crack size and assume that this

corresponds to the 'inherent' defect, namely the maximum pore size of the material. Confusion of the critical crack size with the maximum pore size is common in the literature. Their equivalence is not consistent with observed sub-critical cracking before fracture. Pickup (1984) has pointed out that the critical crack area is much larger than the area of the largest pore indicating the 'build-up' of the critical crack which occurs with increasing applied stress. However, this calculational method using equation 2.3 is useful. Brocklehurst (1974) established the size of artificial defect that just becomes distinguishable from naturally occurring flaws in four-point bend and tensile tests. For very shallow notches failure does not always occur from the notch root but when the notch failure probability reaches one, it is assumed that the 'inherent' defect size has been exceeded. For example in SM2-24 graphite (listed in Table 3.2) values of 'inherent' defect size obtained by this method are 0.5 mm in bend and 0.8 mm in tension. The usefulness of this approach was examined by Darby (1976) who concluded that for a given graphite there is no single 'inherent' defect size which may be used with a constant K_{Ic} value in different laboratory tests to predict fracture using expressions of the form of equation 2.3. Rather, the length of the 'inherent' defect decreases with increasing stress gradient, indicating high strength in high gradients. In a series of bend tests on beams containing notches of various depths, Birch et al. (1983) found that a consistent value of K_{Ic} was obtained by defining an 'inherent' defect size equal to the maximum particle or pore size present. Sakai et al. (1984) in tests on pyrolytic graphite have found that the value of c in equation 2.3 is a factor of 16 different in the two possible orientations parallel to the basal planes. Thus for a given stress gradient and a given orientation an

'inherent' defect size may be determined but it is not equivalent to the maximum particle or pore size. This is discussed further in Chapter 6.

Kennedy (1983) in studying the physical processes contributing to fracture toughness found an exponential decrease in the critical stress intensity factor with increase in porosity after oxidising Stackpole 2020 and H-451 graphites (listed in Table 3.2) in steam at 900°C and 1000°C. Results for the critical crack extension force G_{Ic}, in plane stress equal to K_{Ic}^2 divided by Young's modulus, all extrapolate back to the high value of 750 Jm^{-2} at zero porosity. This suggests that the ideal strength of fully graphitised binder is constant but in practice is reduced by the flaw distribution present. For H-451 critical crack sizes calculated from LEFM increased linearly with oxidation in agreement with microstructural observation of largest pore size, although Kennedy does not make the distinction above between these two quantities. For 2020 grade the critical crack size remained constant at 0.5 mm for all tests compared with the largest pore size of 0.1 mm. In this case impurity clusters of approximately 0.5 mm diameter were deduced to act as catalytic oxidation sites. It is probable that these clusters do represent the critical defect size and are responsible for failure before the linkage of sub-critical cracks which would cause failure in the absence of such clusters.

The methods of LEFM have also been used in fatigue (Marshall and Priddle, 1973b) and impact (Birch and Brocklehurst, 1983) studies. The crack growth range per cycle is found to be proportional to the stress intensity range (ΔK) for crack propagation to the fourth power. Birch and Brocklehurst have integrated this expression to predict fatigue and impact endurance curves using different constants of

proportionality.

Buch (1976) developed a model of polycrystalline graphite fracture using LEFM but with the addition of microstructural input. The model is based on the weakness of graphite grains in the c direction. The graphite is considered to consist of discrete particles each with a single cleavage plane which, under appropriate loading, link up to form a critical defect according to LEFM. Buch had considerable success in predicting the uniaxial tensile strength of a wide range of commercially available graphites based on input parameters of critical stress intensity factor, particle size, particle orientation, particle cleavage stress, porosity and specimen volume.

2.3 Experimental Techniques

2.3.1 Surface energy and work of fracture

The Griffith (1920) theory for the plane strain failure of a body containing a sharp surface crack of length c gives the failure stress σ, as

$$\sigma \approx \frac{1}{f(c/h)} (2E\gamma/\pi c)^{\frac{1}{2}} \qquad (2.4)$$

where γ is the effective surface energy per unit area of crack face and f(c/h) is as defined in equation 2.3. Combining this expression with equation 2.3 gives

$$K_{Ic}^{2} = 2E\gamma. \qquad (2.5)$$

Hence the critical stress intensity factor is simply a function of Young's modulus and effective surface energy. Taylor et al. (1967) determined values of γ at crack initiation in several nuclear graphites of 7-25 Jm^{-2} with a mean value of 15 Jm^{-2}. Using equation 2.4 with an estimate of c = 1 mm (again no distinction between maximum pore size and critical defect size was made), values of elastic

strain energy ($\sigma^2/2E$) were obtained in good agreement with those derived from tensile stress-strain curves. However, from equation 2.5, use of γ = 15 Jm^{-2} leads to a low estimate of K_{Ic} indicating that further energy absorption beyond crack initiation contributes to K_{Ic}. The effective surface energy at crack propagation (termed the work of fracture) may be obtained from the area under the load-deflection curve to maximum load in a notched beam test divided by the ligament area beneath the notch. Values obtained decrease with increasing notch depth and for PGA graphite lie between 220-80 Jm^{-2} (Davidge and Tappin, 1968; Turner, 1973). Substituted in equation 2.5 these overestimate K_{Ic} for the following reasons (Taylor et al., 1967)

(i) the true crack surface area is many times the nominal fracture area,

(ii) there is much secondary cracking away from the final failure crack,

(iii) in unirradiated graphite crack growth is modified by plastic flow around the crack tip,

(iv) crack interaction occurs.

Pickup et al. (1982) calculated work of fracture values in a study of the fracture properties of IM1-24 graphite thermally oxidised at up to 6% weight loss. The effective surface energy was found to decrease slightly with burn-off, while K_{Ic} decreased exponentially. They concluded that the change in K_{Ic} was controlled by the Young's modulus which decreases due to the development of fine filamentary pores.

2.3.2 Non-destructive tests

The design and specification of manufacturing route for graphite moderator bricks has been described by Prince (1979). Kennedy et

al. (1984) have outlined non-destructive examination techniques namely measurement of bulk density, dynamic Young's modulus, ultrasonic attenuation, eddy current response and radiography. They developed an experimental graphite H-451-I, with improved properties over H-451, the reference grade for the United States designed high temperature gas-cooled reactor (HTGR). No correlation was found between the dynamic Young's modulus measured from sonic velocity (ASTM, 1974) and subsequent tensile strength of individual specimens. This result is expected as the whole structure contributes to the modulus whereas strength is influenced by the largest defects present. However, using ultrasonics the attenuation coefficient α, was found to be proportional to the maximum pore size such that failure stress and modulus obey the relation

$$\sigma = A(E/\alpha)^{\frac{1}{2}} \qquad (2.6)$$

where A is a constant related to the square root of the effective surface energy. Note the dimensions of this expression agree with the Griffith equation, 2.4.

In the United Kingdom, the integrity of CAGR fuel sleeves is assured by proof pressure testing (Glendinning and Stacey, 1981). Eddy current testing in isolation, has been found to be inadequate as an acceptance/rejection criterion for fuel sleeves (Chapman, 1982).

Acoustic emission in conjunction with mechanical tests has also been investigated (Gilchrist and Wells, 1969; Kraus and Semmler, 1978). The onset of acoustic emission occurs at a characteristic stress for any graphite of between 10-40% of the final failure stress. This onset has been associated with basal plane cleavage (Pickup et al., 1981). Generally, large well orientated coke particles cleave easily such that coarser graphites show earlier and greater amounts of sub-critical cracking than fine grained material. Recent tests

using more sensitive equipment have detected emission at lower onset stresses (Burchell et al., 1984) but consistency with earlier results has been maintained by rejecting very low amplitude events near the electrical noise level.

2.3.3 Microscopic analysis

Jenkins (1962) bonded thin plates of PGA graphite to thicker brass bars such that there was a uniform strain field in the graphite during four-point bend tests performed in situ on an optical microscope. Sub-critical fracture occurred easily along striations within coke particles which were favourably orientated to the applied stress. Measured dynamic modulus decreased with increasing strain. The final fracture of graphite beams involved crack propagation through the binder phase. Similar although more sophisticated experiments were performed by Taylor et al. (1967) and Knibbs (1967). Smith (1970) has given a qualitative summary of microfracture observations from experiments such as these. Microcracks of a characteristic size according to the crystal and defect structure form early in a fracture test. Eventually there is a linking of microcracks and catastrophic fracture occurs but early cracks do not necessarily propagate directly to fracture. The non-recovery of strain observed on unloading indicates that slip must occur adjacent to opening cracks to accommodate outward bowing of crack surfaces. Otherwise if crack opening were completely elastic full strain recovery is expected. On heating to the graphitisation temperature, any residual strain from a low temperature test is partially or completely recovered. Smith assumes that the mechanism of slip is basal plane dislocation motion which is reversed at high temperature by thermally activated back motion of the dislocations under the driving force of elastic energy stored remote from the crack. He

also suggests that the progressive development of back-stresses from this stored elastic energy is responsible for the arresting of individual microcracks at small lengths. Although this provides a reasonable picture of deformation behaviour no quantitative model at present relates microscopic mechanisms to macroscopic stress-strain behaviour.

Marsh (1978) describes the use of a polarised light microscope with a quartz sensitive tint inserted between the specimen surface and the analyser to create interference colours - yellows, blues and purples - which characterise the structure. The colours represent the orientation of basal planes with respect to the polished surface. Yellow and blue are indicative of planes intersecting the surface and purple of basal planes lying parallel to the surface. This technique might be informative in studying preferred crack growth directions relative to the crystal structure (Burchell, 1984).

Meyer et al. (1974) used a scanning electron microscope to observe controlled crack growth in a wide range of graphites. They noted that

(i) the growth of cracks within coke particles is coincident with the basal plane direction,

(ii) short microcracks link up as the stress increases,

(iii) the orientation of microcracks varies by up to 50^{o} from the tensile plane,

(iv) pores may act as crack stoppers or crack nucleii.

Thus the microstructure was observed to control the direction and rate of fracture. These conclusions are supported by a transmission electron microscope study on AXF-Q1 graphite (Stevens, 1971).

Quantitative optical image analysis using impregnation techniques to enhance the contrast of open pores in the microstructure has mainly

been developed for studies of porosity development during radiolytic or thermal oxidation (Stephen, 1984; Pickup, 1984). This is now being adapted to study the relation between porosity development and reduction in strength (Burchell, 1984).

2.4 Summary

Kelly (1981) has defined two characteristic lengths for a given polycrystalline graphite

(1) the maximum coke particle size ℓ, also equal to the maximum pore size,

(2) a length L, approximately 10 ℓ or greater over which physical property measurements are representative of bulk behaviour.

Also Kelly classifies the severity of stress gradients in terms of σ_t/L where σ_t is the tensile strength measured on samples of length greater than L in all directions. This terminology provides a useful framework to list present ability to define a failure criterion in the four extreme cases quoted by Kelly.

(i) Component dimensions > L stress gradients all < σ_t/L. Continuum theories may be formulated but must be verified in different stress conditions. No one theory can adequately explain all observed behaviour.

(ii) Component dimensions < L stress gradients all < σ_t/L. Decreasing strength with decreasing volume (see Figure 2.1) is found. In specific situations, tensile strength may be determined for the relevant specimen size and a maximum normal stress criterion applied as in section 2.2.1. However, the drawbacks listed in section 2.2.1 will apply.

(iii) Component dimensions > L stress gradients all > σ_t/L. There is benefit to be gained as strength is greater than σ_t but no

quantitative theory is available for the general case.

(iv) Component dimensions < L stress gradients all > σ_t/L. Comments are as for (ii) except a lower limit bend strength may be more applicable as a maximum stress failure criterion.

Cases (i) and (iii) are most frequently encountered in practice and therefore most attention will be focussed on them in subsequent chapters. When deep notches of small root radius are present LEFM methods are adequate. However, real components cannot be designed with such defects as their strength would obviously be drastically reduced. The Buch model (1976) offers the potential of building on the LEFM approach with a simple yet physical microstructural input. Furthermore, it is in principle compatible with numerical stress analysis methods such as finite element techniques to evaluate stress distributions in arbitrary components under general loading.

This thesis extends the Buch model initially to bend stress distributions and then more widely to cases of biaxial tension and combined bend and tensile stresses. Fracture from a notch in bending, making use of finite element predictions of stress ahead of the notch, is then considered followed by application of the model to explain changes in strength on irradiation. Experimental results obtained as part of this project are reported and used at each stage in the development and application of the model.

CHAPTER 3

MANUFACTURE AND PHYSICAL PROPERTIES OF POLYCRYSTALLINE GRAPHITES

3.1 Manufacture

All graphites are nearly pure carbon and therefore are not practicably melted and cast. Polycrystalline graphites are made by the common ceramic technique of mixing a solid particulate filler with a liquid binder, compacting and heat treating to expel volatiles and produce the phases desired in the finished body.

The usual filler is coke obtained as a by-product of the petroleum industry or from natural sources. For nuclear applications a very low level of impurity content is desired particularly of elements with high neutron capture cross sections such as boron. Either a very pure coke source or a chemical purification process based on exposure to a halide must be used. Filler cokes vary widely in particle size and shape distributions, depending on the required properties. There is typically 30% porosity between the particles to permit good wetting by the binder during manufacture.

The steps in manufacture are shown schematically in Figure 3.1. Calcination is a heat treatment process at between 900-1300^{o}C designed to reduce the volatile content and to prevent excessive shrinkage of the coke in subsequent operations. Following calcination the coke is crushed, milled and sieved into fractions ranging from fines known as 'flour' of about 0.4 mm diameter to particles of perhaps 10 mm diameter or greater. From these the required distribution of sizes is selected, mixed with the binder pitch at temperature and formed into shape by extrusion or moulding. The pitch contains elements other than carbon, principally hydrogen to ensure good flow between the individual coke particles. On forming, the coke particles tend

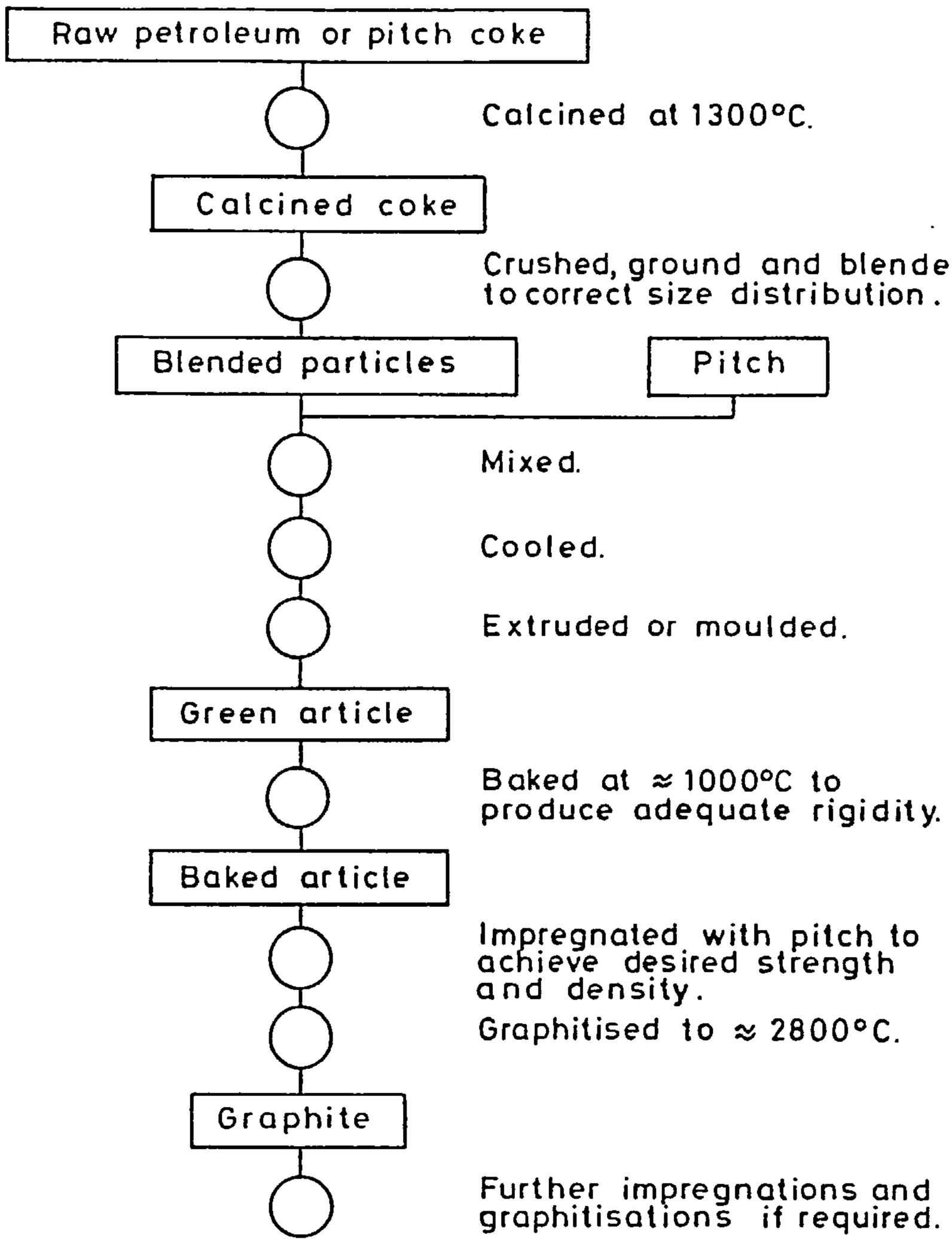

Figure 3.1: A Schematic diagram of the manufacturing route for polycrystalline graphite (Kelly, 1978).

to align with their basal planes parallel to the extrusion direction or perpendicular to the pressing direction so producing at least a symmetry in properties about the forming axis, termed orthotropy, in the finished article. In the U.K. it is customary to refer to properties parallel or perpendicular to the forming direction. However, in the U.S.A. reference is made to the orientation of basal planes. Table 3.1 indicates the relation between the two terminologies for extruded and moulded pieces. Graphite splits most easily parallel to the basal planes as then only the weak inter-layer bonding has to be overcome.

After forming, the green article is baked at between 800-1000^{o}C. This involves a slow heating cycle between 30-70 days during which some $\frac{1}{3}$ of the binder is volatilised. The eventual yield of solid carbon from the binder is only 50-60% and as it loses mass it also loses volume producing shrinkage cracks and voids. Therefore to avoid a grossly porous and cracked body, venting porosity must be established early during the bake. Any gas which cannot reach the surface will produce blow-holes if the material is still plastic or large cracks if it is not. During baking approximately 5% shrinkage takes place. The filler coke does not contribute to this as it has been previously calcined at a higher temperature.

The baked product may be graphitised directly particularly for coarse electrode material. However, density may be increased by impregnation usually with coal tar pitch and then rebaking to pyrolyse the impregnant in the pores. Normally two or three impregnations are performed. Above this number their effectiveness rapidly decreases.

The final graphitisation is carried out in an Acheson furnace at temperatures in the range 2600-3000^{o}C. .Heating takes approximately three days and cooling and unloading a further 8-10 days.

Table 3.1

Relation between the forming process, alignment of coke particles and relative strength.

DIRECTION OF APPLIED STRESS	EXTRUSION	MOULDING
Parallel to forming direction	with grain (stronger)	against grain (weaker)
Perpendicular to forming direction	against grain (weaker)	with grain (stronger)

Graphitisation is a two stage process of converting the initial organic material to solid carbon by the elimination of side chains at below 1000°C, followed by the conversion of carbon to graphite by annealing out interlayer defects. The mechanisms are extremely complicated and there are only limited techniques available for their study (Fitzer et al., 1971), namely controlled pyrolysis in sealed tubes, autoclaves or flow cells. However, one feature is evident (Kelly, 1981). At 400-500°C the aromatics present segregate into a mesophase and a fluid matrix. As heating continues the mesophase spheres grow at the expense of the matrix. This gives the material the mobility necessary to nucleate orientated regions such that the conversion of carbon to graphite may occur. It is notable that the degree of ordering increases over a wide temperature range unlike most solid state transformations which occur at a characteristic temperature.

Recent advances in graphite manufacture have been made in the forming and impregnation stages in response to demands for high strength isotropic materials mainly for aerospace applications. These involve large compressive stresses on the body to obtain better densification and hence improved strength. The most commercially successful of these techniques is hot isostatic pressing (Ragan and Marsh, 1983).

3.2 Structure and Mechanical Properties

Manufactured polycrystalline graphites are brittle solids which contain from 15-30% porosity in the form of cracks, shrinkage cavities and blow-holes. This gives typical densities between 1.6-1.9 g/cm^3 compared with a theoretical value of 2.26 g/cm^3 for perfect graphite. The porosity may be loosely divided into two types (Brocklehurst, 1974); large pores which determine the internal stress distribution

during external loading and small microcracks related to the crystal structure.

Pores in the larger category vary from approximately 10^{-2} mm to the maximum filler particle size and exist either as closed voids or open porosity. There is always a distribution of large pores present due to the requirement for adequate venting during manufacture, although the largest ones termed 'disparate' flaws may be avoided by careful processing. Smaller pores (approximately 10^{-2} mm or less in length) arise from anisotropic crystal contraction during cooling from the graphitisation temperature. They relieve internal stress within crystallites and always lie parallel to the basal plane. Their existence was first postulated by Mrozowski (1956).

Table 3.2 lists mean strength and modulus data for various grades of polycrystalline graphites in common usage (Brocklehurst, 1974). The strength values quoted are intended as a guide only, as size effects are not considered. Due to the inhomogeneous material structure, physical properties of a series of pieces of any grade will be distributed around these mean values. Typical standard deviations are ± 5% on modulus and ± 10% on strength. The precise variations are dependent on the control of raw materials, degree of processing technology and non-destructive test procedures carried out on finished components.

The new work reported in this thesis is directed towards two graphites. Firstly, an extruded pitchcoke grade and secondly, isotropic IM1-24 moderator graphite. Both are included in Table 3.2. However, the fracture model developed is suitable for use with any graphite or brittle ceramic material.

Table 3.2

Density, strength and Young's modulus of common graphite grades

GRADE	SOURCE	FORMING METHOD E-EXTRUSION M-MOULDING	BULK DENSITY (g/cm^3)	YOUNG'S MODULUS (GPa) $\parallel/\perp$ TO FORMING AXIS	STRENGTH (MPa) PARALLEL/ PERPENDICULAR TO FORMING AXIS		
					TENSILE	BEND	COMPRESSIVE
PGA	UK	E	1.7	11/6	10/6	14/9	30/30
SM2-24	UK	M	1.7	8.0/8.5	12	19	47
PITCHCOKE	UK, FRANCE	E	1.8	13/10	25/17	32/26	70/63
IM1-24	UK	M	1.8	10	22	33	85
AGOT	USA	E	1.7	10/8	10/9	16/13	41/41
ATJ	USA	M	1.75	8/10	10/12	25/28	59/57
H-451	USA	E	1.75	10/8	13/8	20/24	
GRAPHITITE-G	USA	E	1.9	10/7	23	38	78
STACKPOLE 2020	USA	M			24/25		
AXF-Q1	USA	M	1.85	10/10	33	96	138
AXM	USA	M	1.75		51		
CARBON FIBRES				200/	1000/		

Data from Brocklehurst (1974) or literature references listed in the text which quote specific grades.

CHAPTER 4

A THREE-DIMENSIONAL MODEL OF FRACTURE

4.1 Introduction

The Buch model of fracture (1976) is capable of predicting the uniaxial tensile strengths of polycrystalline graphites. In this chapter a three-dimensional fracture mechanics analysis is presented which extends the Buch model to non-uniform stress states in three- and four-point bend. The results of theory and experiment for pitchcoke and IM1-24 graphite are compared.

4.2 Experimental

Tensile, three-point and four-point bend tests were carried out on both graphites. All tests were such that on pitchcoke the direction of maximum stress was perpendicular to extrusion and on IM1-24 perpendicular to the moulding axis. A schematic diagram of the test arrangements is shown in Figure 4.1. Specimen sizes, number of tests and mean failure stress from standard elastic formulae are given in Table 4.1 for pitchcoke and Table 4.2 for IM1-24.

The end pieces for each tensile specimen were individually machined to ensure that any misalignment during the pull was minimised. Figures 4.1(b) and (c) show the bend test configurations. The three-point results listed in Table 4.1 show a drop in mean strength from 34.0 MPa at the narrowest knife edge spacing (19 mm) to 30.1 MPa at the widest. This drop corresponds to a decrease, in the absence of a crack, in stress gradient parallel to the tensile surface of the beam as ℓ_3 increases. The four-point result provides a lower limit to bend strength. This is expected as the outer ligament stress is at a constant maximum value between the inner knife edges, a state which is approached in three-point bend as the knife edges become widely spaced. It is also evident that the three-point bend strength

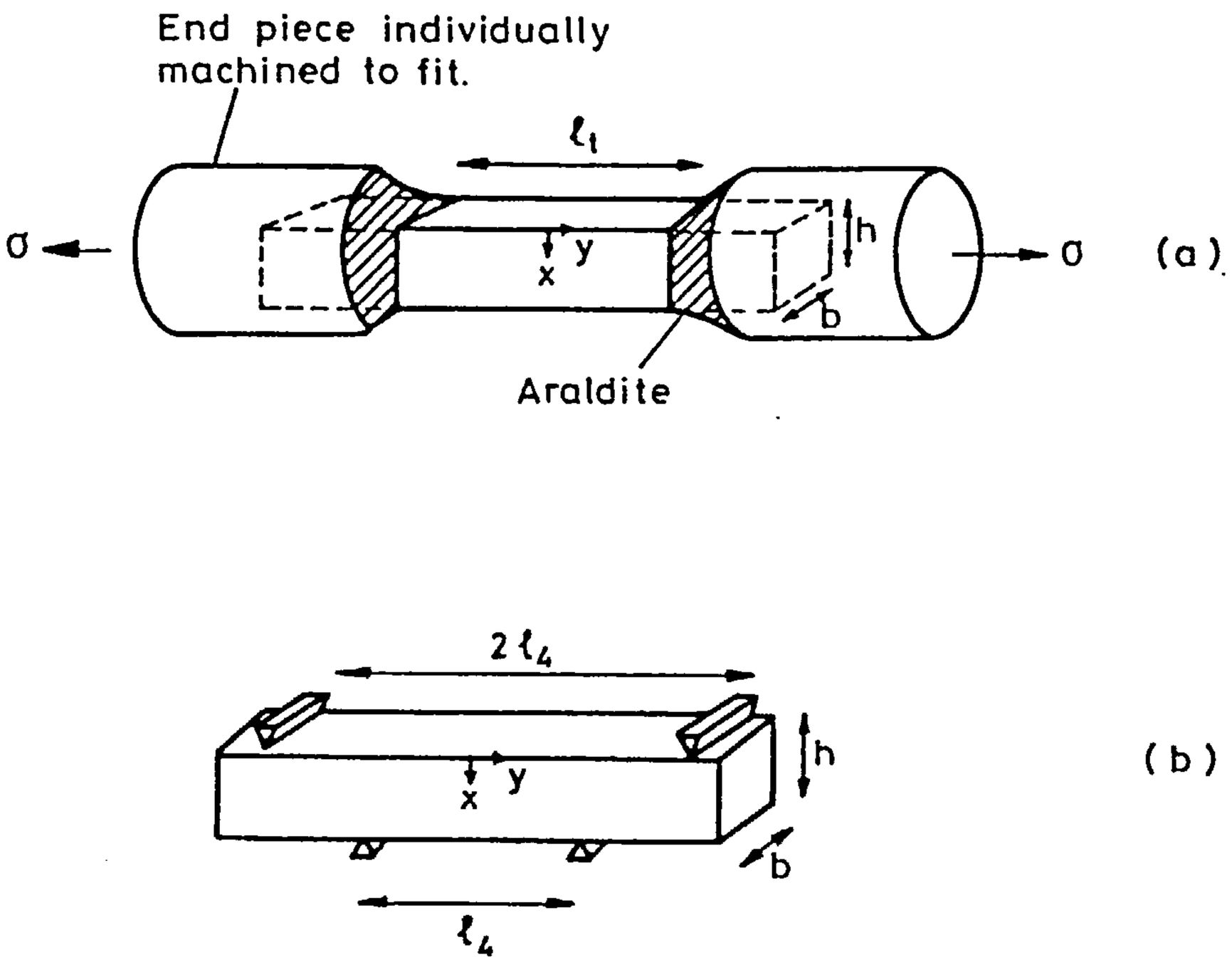

Figure 4.1: Schematic diagram of tensile and bend arrangements.

Table 4.1

Comparison of experimental results and theoretical predictions for Pitchcoke graphite.

All specimens 9.0 x 9.0 x 75 mm. ℓ_3, ℓ_4 and ℓ_T are as defined in Figure 4.1.

Three Point Bend

ℓ_3 (mm)	NUMBER OF SPECIMENS TESTED	MEAN FAILURE STRESS (MPa)		
		MEASURED*	3-D PREDICTIONS	2-D PREDICTIONS
19	100	34.0 ± 3.0	33.5	33.6
32	10	31.9 ± 1.8	32.6	32.6
51	20	31.1 ± 1.5	32.0	31.8
64	20	30.1 ± 1.9	31.8	31.5

Four-Point Bend

ℓ_4 (mm)	NUMBER OF SPECIMENS TESTED	MEAN FAILURE STRESS (MPa)		
		MEASURED*	3-D PREDICTIONS	2-D PREDICTIONS
19	12	30.1 ± 1.2	29.5	28.8
32	25	29.1 ± 1.7	29.1	28.2

Tension

ℓ_T (mm)	NUMBER OF SPECIMENS TESTED	MEAN FAILURE STRESS (MPa)		
		MEASURED*	3-D PREDICTIONS	2-D PREDICTIONS
30	7	20.6 ± 1.6	25.0	20.8 (invalid region)

* ± 1 standard deviation

Table 4.2

Comparison of experimental results and theoretical predictions for IM1-24 graphite.

TEST	NUMBER OF SPECIMENS TESTED	SPECIMEN DIMENSIONS UNDER TEST	MEAN FAILURE STRESS (MPa)		
			MEASURED*	3-D $PRED^{NS.}$	2-D $PRED^{NS.}$
3-Point Bend	70	32 x 10 x 10 mm	40.2 ± 3.8	39.6	39.6
4-Point† Bend	252	38 x 19 x 19 mm (within inner span)	33.6 ± 3.3	33.2	34.9
Tension†	126	60 mm x 12.5 mm dia.	22.9 ± 2.0	28.9	24.6

* ± 1 standard deviation.

† Metcalfe, 1981.

shows a greater volume dependence than the four-point strength over the range examined.

A required input parameter to the fracture model is the basal plane cleavage stress S_c, of a coke particle. This was obtained using an acoustic emission method (Pickup et al., 1981) such that the onset of continuous emission (taken to be a count rate greater than one count per second) during a test was assumed to represent cleavage of the most favourably orientated particle. It may be that the first emissions represent frictional sliding of material but in bend tests done in situ on an optical microscope, cleavage cracks were formed at the same low stress levels as the acoustic emission onset. Emission was detected using a lead zirconate titanate piezoelectric transducer attached to the specimen with vacuum grease and held in position by a small clamp. Output from this transducer was amplified and monitored with standard Endevco acoustic emission equipment set in the amplitude distribution mode. The onset of continuous emission occurred within the stress range 4.5-6 MPa for all bend tests on pitchcoke graphite and 5-10 MPa for similar tests on IM1-24. The lowest figure, 4.5 MPa (approximately 15% of the final failure stress) was taken to be the cleavage stress of the most favourably aligned coke particle for both graphites.

4.3 Model of Fracture

The model is developed initially for pitchcoke. Its application to IM1-24 is discussed in section 4.4.2.

4.3.1 Stress distribution

Consider a defect free beam of depth h and width b. When loaded as in Figure 4.1 the stress distribution may be written in the convenient form

$$\sigma(x,y) = \sigma_o \left(1 - \frac{2a_1 x}{h}\right)\left(1 - \frac{2a_2|y|}{\ell_3}\right) \qquad (4.1)$$

where $a_1 = 0$, $a_2 = 0$ (tension)

$a_1 = 1$, $a_2 = 0$ (4-point bend) $|y| < \ell_4/2$

$a_1 = 1$, $a_2 = 1$ (3-point bend).

In each case σ_o is equal to the maximum tensile stress in the specimen. In four-point bend, failure is assumed to occur between the inner knife edges.

4.3.2 Microstructure

Figure 4.2 shows an optical micrograph of a pitchcoke specimen during a three-point bend test. The surface shown is the ligament at maximum tensile stress as indicated in Figure 4.1 (c) and the stress acting upon it is approximately 0.4 of the final failure stress. Note that a crack (A) of length equal to the particle size has formed within the central coke particle parallel to the basal plane direction. Further sub-critical cracks at particle/matrix boundaries (B), starting or finishing in a pore (C) and traversing a binder region (D) are also evident. This graphite contains approximately 18% porosity with pore sizes ranging from sub-micron to approximately 1 mm in length. From the evidence of sub-critical fracture in Figure 4.2, which is typical of this and many other graphites, it appears that fracture behaviour is determined by the coke particles and the large pores present. For the purpose of the model the material is therefore taken to consist of a series of large particles embedded in a compact of smaller ones some of the smaller particles being pores. The following assumptions are made

(i) Large particles alone act as microcrack initiation sites.

(ii) Microcracks form when the component of applied tensile stress acting on the randomly orientated plane of weakness of the particle exceeds the cleavage stress S_c. That is a plane inclined at an angle ϕ to the applied stress σ will fail when

Blank

In

Original


B
D
A
C

$$\sigma \cos^2 \phi \geq S_c . \qquad (4.2)$$

(iii) Crack propagation occurs by cleavage of small particles adjacent to the initiation site.

(iv) The presence of microcracks does not enhance the likelihood of cleavage in neighbouring particles.

(v) Porosity present is modelled as an equivalent volume of particles having zero cleavage stress.

(vi) Failure occurs when a critical crack according to LEFM is formed by a contiguous array of microcracks.

4.3.3 Crack initiation

Consider the large particles as spheres of radius A, constituting a volume fraction F of the material. The number N of large particles per unit volume may thus be written

$$N = 3F/4\pi A^3 . \qquad (4.3)$$

On the basis of assumption (i), for uniaxial tensile loading it is assumed that each large particle is a potential failure site. For simplicity, cracks in particles penetrating the surfaces of the beam are taken to behave essentially as interior cracks. This is because a semi-circular crack of radius A in the surface will be elastically almost equivalent to an embedded circular disc crack of the same radius. Thus the number of possible initiation sites associated with unit length of the beam in tension is $z_t = Nbh$. In the bending modes, although totally embedded cracks could act as initiation sites the stress distribution across the beam renders them of negligible importance compared with defects intersecting the tensile surface. For simplicity in the present calculation therefore, all interior defects are assumed to have a zero probability of giving rise to failure in bending. Consequently the number of possible initiation sites per unit length of beam in the bending modes is $z_b = 2NAb$.

For all deformation modes, consider the probability of a particle cleaving under the influence of the applied stress field. Figure 4.3 shows a schematic presentation of the failure envelope under an applied stress σ. From assumption (ii) those planes of weakness whose normals lie within a cone of apex angle ϕ are considered to have failed, ϕ increasing with σ according to equation 4.2. The probability P_c of a particle of random orientation cleaving is therefore equal to the ratio of the area of the part-spherical surface cut out by the cone to the surface area of the hemisphere, that is

$$P_c = \frac{1}{2\pi} \int_0^{\phi} 2\pi \sin \phi d\phi = 1 - \cos \phi. \qquad (4.4)$$

Hence from assumption (ii)

$$\begin{aligned} P_c &= 1 - \sqrt{S_c/\sigma} && \sigma \geq S_c \\ &= 0 && \sigma < S_c. \end{aligned} \qquad (4.5)$$

4.3.4 Crack propagation

A cracked large particle must be surrounded by cracked small particles to a critical size if catastrophic failure according to LEFM is to occur. The choice of critical defect is considered in section 4.3.6 but the treatment is here developed for a semi-circular crack.

Following assumption (iii) above, define the small particles as spheres of radius a. A microcrack originating in a large particle will propagate a distance a when all adjacent small particles fail. A pore is considered to be equivalent to a small particle with zero cleavage stress. Figure 4.4 shows a plane at $y = y'$ containing a fracture initiation site surrounded by small particles to a critical radius c, all of which must cleave if, according to assumption (vi), this site is to be responsible for failure. Consider the probability

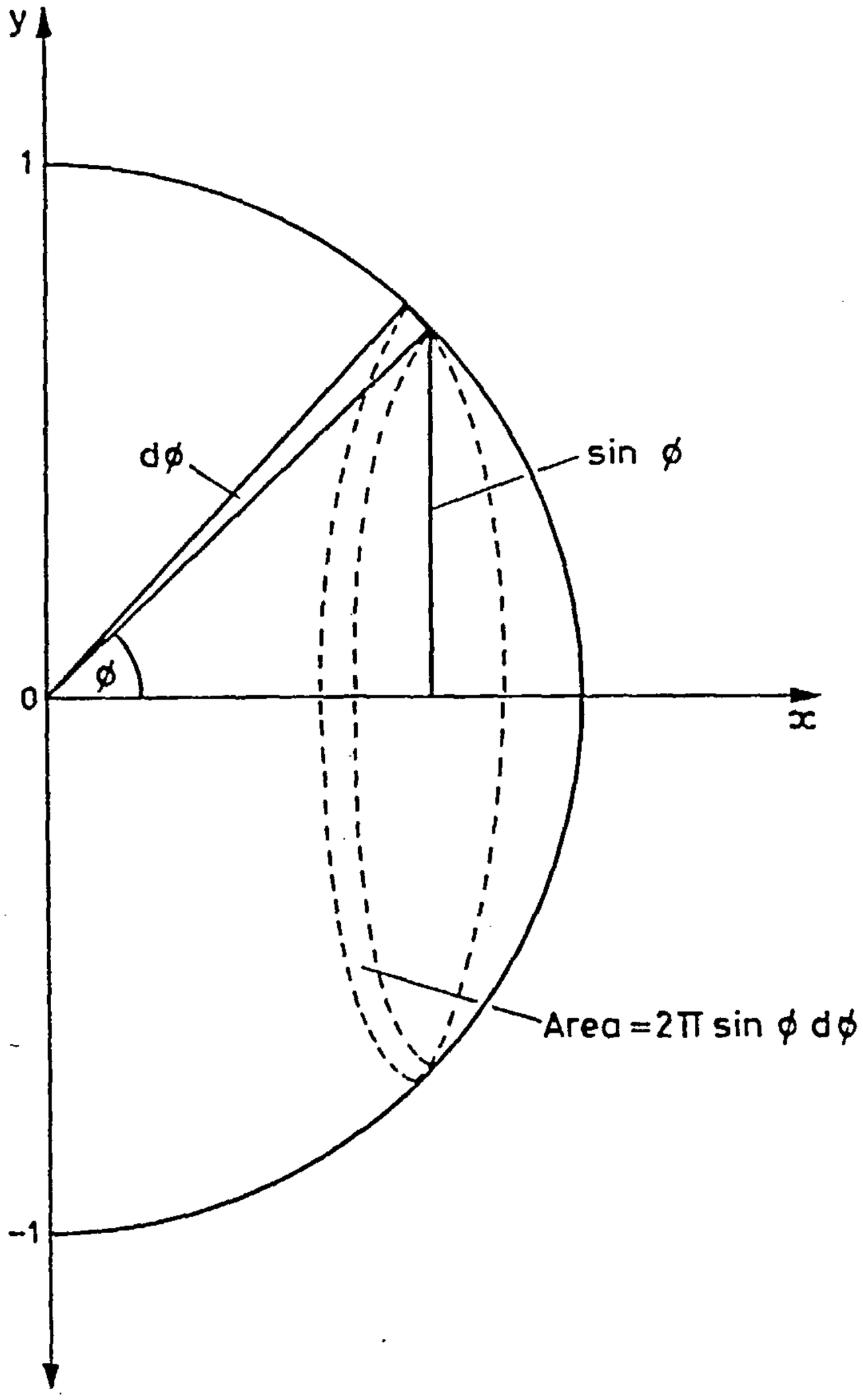

Figure 4.3: A schematic representation of the failure envelope at an applied tensile stress σ. All cleavage planes whose normals lie within the failure cone of apex angle ϕ are considered to have failed.

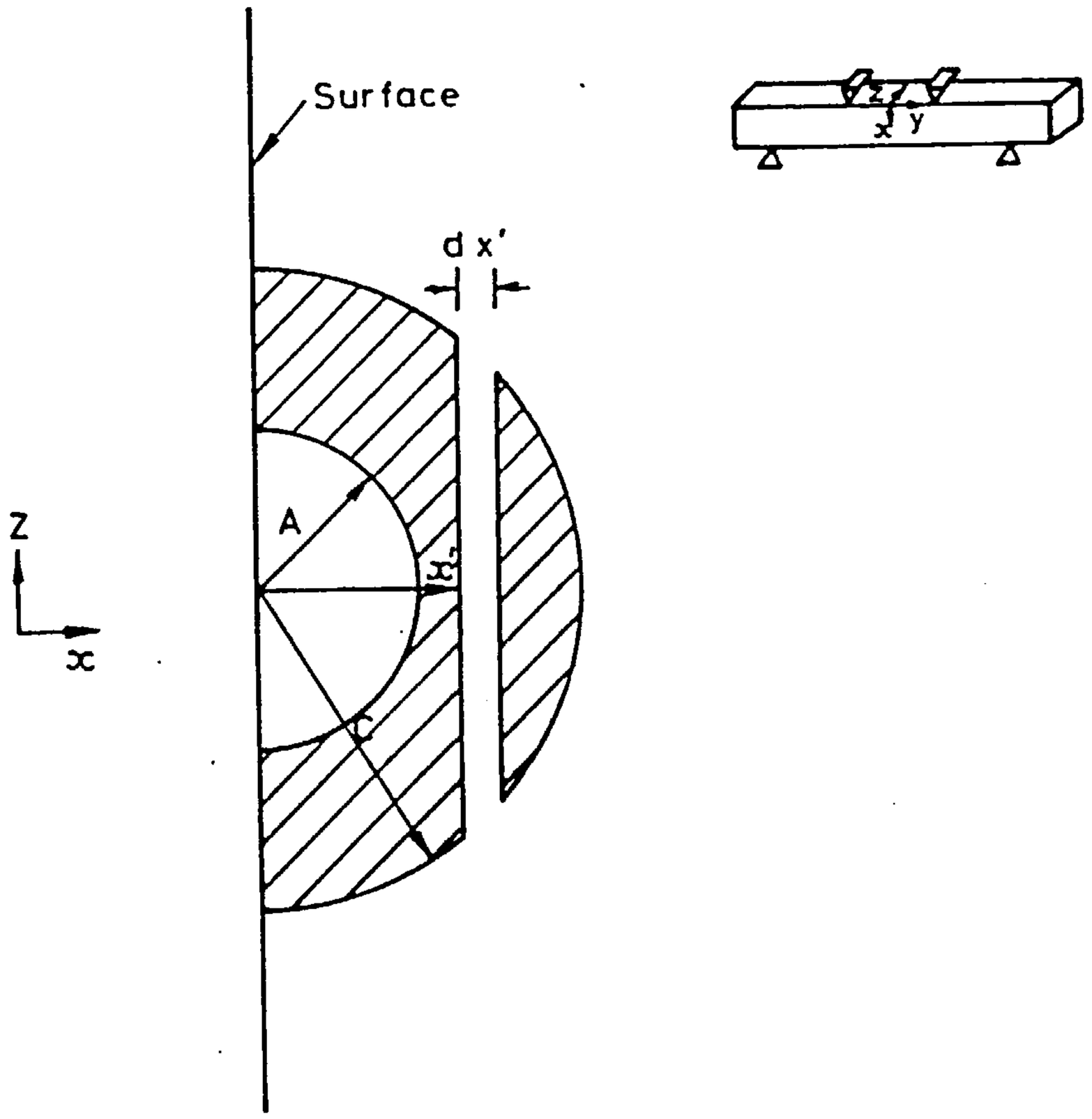

Figure 4.4: A fracture initiation site, radius A, surrounded by a semi-circular region, radius c, which must all be cleaved if this site is to be responsible for failure.

of this happening. If P is the probability that a small particle is a pore, then the probability P_a that the particle at position (x',y') will be cracked is

$$P_a = P + (1 - P)[1 - \sqrt{S_c/\sigma(x',y')}] \qquad \sigma(x',y') \geq S_c$$
$$= P \qquad \sigma(x',y') < S_c. \tag{4.6}$$

As may be seen from Figure 4.4 the number of particles present in the elemental strip at depth $x = x'$ of the propagating crack is

$$dm = 2[(c^2 - x'^2)^{\frac{1}{2}} - (A^2 - x'^2)^{\frac{1}{2}}]\, dx'/\pi a^2 \qquad x' < A$$
$$= 2\,(c^2 - x'^2)^{\frac{1}{2}}\, dx'/\pi a^2 \qquad c \geq x' \geq A. \tag{4.7}$$

The probability P_s that all the particles in the strip are cracked is

$$P_s = P_a^{\,dm}, \tag{4.8}$$

and thus the probability P_g, that the whole of the shaded area of Figure 4.4 is cracked is given by the integral

$$\ln P_g = \int_{m(x'=0)}^{m(x'=A)} \ln(P_a)dm + \int_{m(x'=A)}^{m(x'=c)} \ln(P_a)dm. \tag{4.9}$$

Combining equations 4.5 and 4.9 the total probability P_f that a cracked large particle will be surrounded by a critical defect of radius c may be written

$$P_f = P_g \cdot P_c. \tag{4.10}$$

Strictly, this expression is only valid for a surface defect. However, for simplicity it is assumed to apply equally to surface and interior defects in the same manner as the critical defect radius for tensile loading.

4.3.5 Overall probability of failure

From the above analysis each large particle has an associated probability P_f (which is a function of the local stress distribution)

that it will be a crack nucleation site and be responsible for failure. It remains to determine the manner in which all these quantities may be combined to give an overall probability P_F of the specimen failing.

Let $P_f(n)$ be the value of P_f associated with the nth large particle in the specimen. The probability that the plane containing the particle will not fail is $(1 - P_f(n))$ and hence the overall fracture probability is given by the expression

$$P_F = 1 - \prod_{n=1}^{n} (1 - P_f(n)) \qquad (4.11)$$

where n is the total number of initiation sites which from section 4.3.3 is equal to ℓ times z_t or z_b as appropriate. Rearranging equation 4.11 and taking logarithms

$$\ln (1 - P_F) = \sum_{n=1}^{n} \ln (1 - P_f(n)) \qquad (4.12)$$

which may be evaluated approximately by replacing the summation with an integral, giving

$$\ln (1 - P_F) \approx \int_0^n \ln (1 - P_f(n))dn. \qquad (4.13)$$

$P_f(n)$ may be obtained from expression 4.10 once the critical crack radius c has been determined by the method of section 4.3.6. The left hand logarithm may then be evaluated after integration to give P_F, the overall probability of failure.

Of particular interest in most applications is the mean stress at failure, that is the average value of σ at which the graphite fractures. If there are $D(\sigma)d\sigma$ failures between σ and $\sigma + d\sigma$, the mean failure stress $\bar{\sigma}$ is given by

$$\bar{\sigma} = \frac{\int_0^\infty \sigma\, D(\sigma)\, d\sigma}{\int_0^\infty D(\sigma)\, d\sigma} .$$

that it will be a crack nucleation site and be responsible for failure. It remains to determine the manner in which all these quantities may be combined to give an overall probability P_F of the specimen failing.

Let $P_f(n)$ be the value of P_f associated with the nth large particle in the specimen. The probability that the plane containing the particle will not fail is $(1 - P_f(n))$ and hence the overall fracture probability is given by the expression

$$P_F = 1 - \prod_{n=1}^{n} (1 - P_f(n)) \qquad (4.11)$$

where n is the total number of initiation sites which from section 4.3.3 is equal to ℓ times z_t or z_b as appropriate. Rearranging equation 4.11 and taking logarithms

$$\ln (1 - P_F) = \sum_{n=1}^{n} \ln (1 - P_f(n)) \qquad (4.12)$$

which may be evaluated approximately by replacing the summation with an integral, giving

$$\ln (1 - P_F) \approx \int_0^n \ln (1 - P_f(n))dn. \qquad (4.13)$$

$P_f(n)$ may be obtained from expression 4.10 once the critical crack radius c has been determined by the method of section 4.3.6. The left hand logarithm may then be evaluated after integration to give P_F, the overall probability of failure.

Of particular interest in most applications is the mean stress at failure, that is the average value of σ at which the graphite fractures. If there are $D(\sigma)d\sigma$ failures between σ and $\sigma + d\sigma$, the mean failure stress $\bar{\sigma}$ is given by

$$\bar{\sigma} = \frac{\int_0^\infty \sigma\, D(\sigma)\, d\sigma}{\int_0^\infty D(\sigma)\, d\sigma} .$$

If $D(\sigma)$ is normalised so that

$$\int_0^\infty D(\sigma)\, d\sigma = 1$$

then

$$P_F = \int_0^\sigma D(\sigma)\, d\sigma$$

and the mean failure stress may be written in the useful form

$$\bar{\sigma} = \int_0^1 \sigma\, dP_F. \qquad (4.14)$$

4.3.6 Calculation of critical crack size

It is now necessary to decide the shape of the critical defect for a given applied load. In general a crack will have an associated stress intensity factor under tensile loading K_I, which varies from point to point along the crack front. For instance in both tension and bending the value of K_I for a semi-circular crack is greatest where the crack front meets the surface. On the other hand when the crack is shallow and extends far along the specimen surface the maximum value of K_I will be associated with the deepest part of the crack front. Whatever the defect geometry, the crack begins to grow when the maximum value of K_I reaches the critical value K_{Ic}. Then, under the influence of the applied load, the values of K_I everywhere increase until they too reach K_{Ic}, when the crack front at these points will also begin to advance.

For simplicity, it is assumed that the critical defect is semi-circular of radius c and that unstable crack growth occurs when the value of K_I at the surface exceeds K_{Ic}. For such a crack the dimensionless quantity K^* may be defined by the equation

$$K_I = \sigma(0,y)\, h^{\frac{1}{2}}\, K^* \qquad (4.15)$$

and is dependent only on the ratio c/h. This dependence is illustrated in Figure 4.5 for both tension and bending using the results of the computer code FRACPAC (Chell, 1977). For calculational

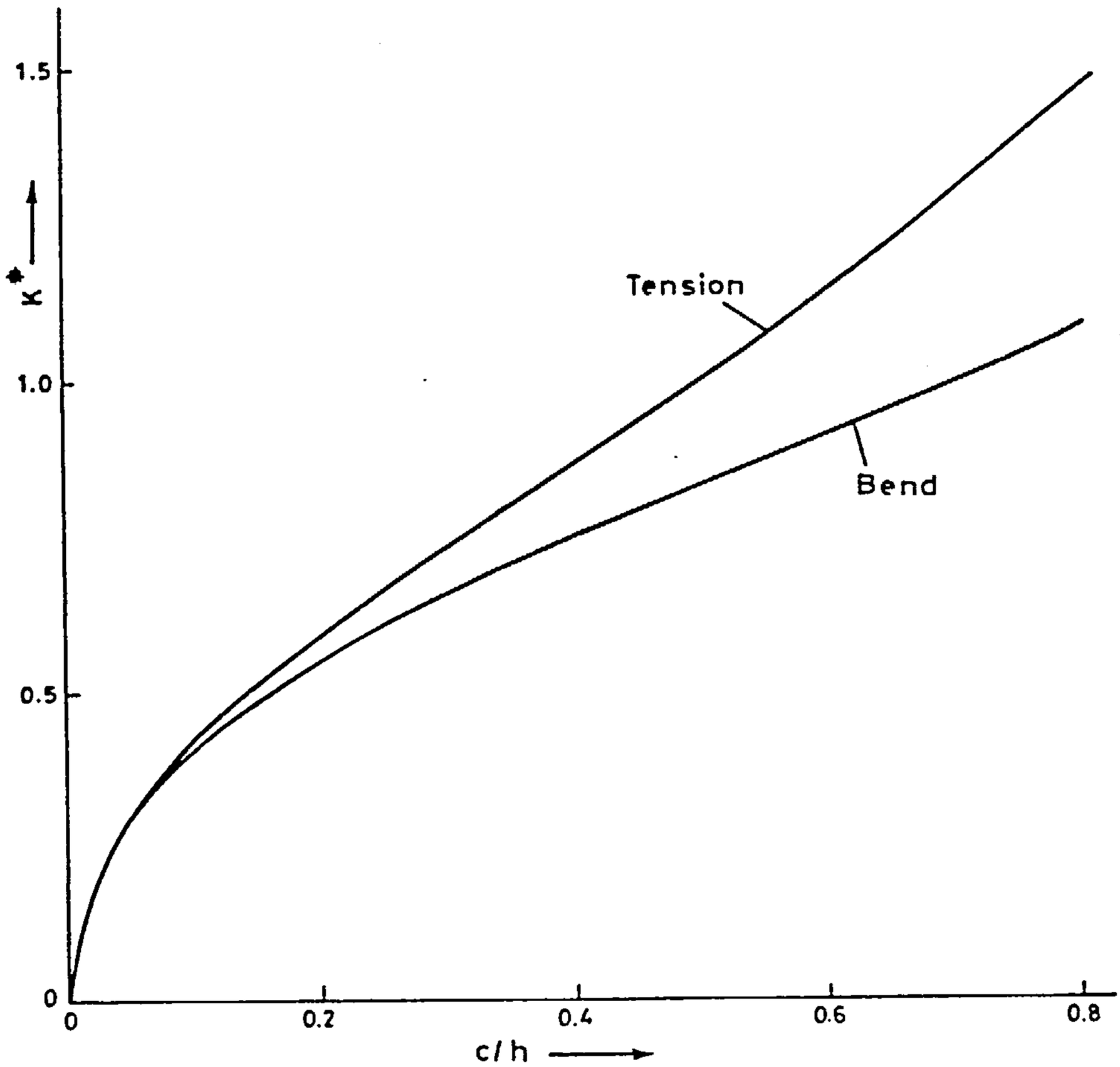

Figure 4.5: The variation of stress intensity factor with crack depth expressed through the dimensionless quantities $K^* = K_I/\sigma(0,y)h^{\frac{1}{2}}$ and c/h.

convenience the variation of c with K^* may be expressed in the polynomial forms

$$c = h\,[0.637\,K^{*2} - 0.132\,K^{*4}] \quad \text{(tension)} \quad c/h < 0.7$$
$$c = h\,[-0.055\,K^{*} + 0.775\,K^{*2}] \quad \text{(bend)} \quad c/h < 0.7. \qquad (4.16)$$

This equation allows the calculation of c for given values of $\sigma(0,y)$ and h, where for a critical defect, K^* is given by equation 4.15 in which $K_I = K_{Ic}$. Modified forms of the bend polynomial exist to allow for the shearing forces present in three-point loading at specific span-to-width ratios (Brown and Srawley, 1966). These predict critical crack sizes within 5% of the pure bending expression and this decrease has been ignored in the present calculation. Inclusion of the effect does not significantly change the predicted failure stresses in three-point bending.

4.4 Results and Discussion

4.4.1 Pitchcoke graphite

Together with specimen dimensions the following values were used as input data

(i) K_{Ic} 1.2 MPa $m^{\frac{1}{2}}$ - determined from single edge notched bend tests described in Chapter 6.

(ii) Particle cleavage stress S_c 4.5 MPa - obtained from acoustic emission measurements.

(iii) Large particle radius 0.75 mm and volume fraction 0.2.
Small particle radius 0.4 mm - both radii estimated from microstructural observation.

(iv) Volume fraction porosity 0.18 - obtained from density measurements.

In the calculation of failure probabilities, fracture toughness is the highest ranked variable. A 20% increase in K_{Ic} leads to a 16% increase in predicted mean fracture stress whereas similar changes

in any one other parameter alters this mean by less than 4%. Thus the model is relatively insensitive to the particular values deduced from microstructural observation. Figure 4.6 illustrates the predicted probability of failure from equation 4.13 compared with experimental data from Table 4.1. Two examples are shown, a three-point bend test at knife edge spacing ℓ_3 = 19 mm and a four-point bend test with ℓ_4 = 32 mm. Agreement is close but not exact. The four-point strength is lower and the failure probability curve steeper than the three-point case because all initiation sites within the inner knife edges are subjected to the maximum fibre stress. In three-point bend, only sites immediately opposite the central knife edge are so loaded. The model tends to underpredict the number of failures in the low probability/low stress region in both examples indicating that the material variation, for example in pore and particle sizes, is greater than that assumed.

The agreement between theory and experiment is further illustrated in Figure 4.7, which shows the variation of three-point bend strength with knife edge spacing. The falling strength with increasing span arises as the stress gradient in the direction of the beam axis becomes more gradual such that a larger number of initiation sites is subjected to high stress.

Considering the tensile case, the experimentally determined strength of 20.6 ± 1.6 MPa as in Table 4.1 is lower than the value of 25.0 MPa predicted from equation 4.14. It is conceivable that there was some misalignment between the specimen and the grips which would distort the uniaxial stress field and hence give a lower apparent tensile strength. More likely however, the assumptions made in the model lead to an over-estimate of tensile strength. The predicted tensile/bend strength ratio of 0.79 (taking the three-

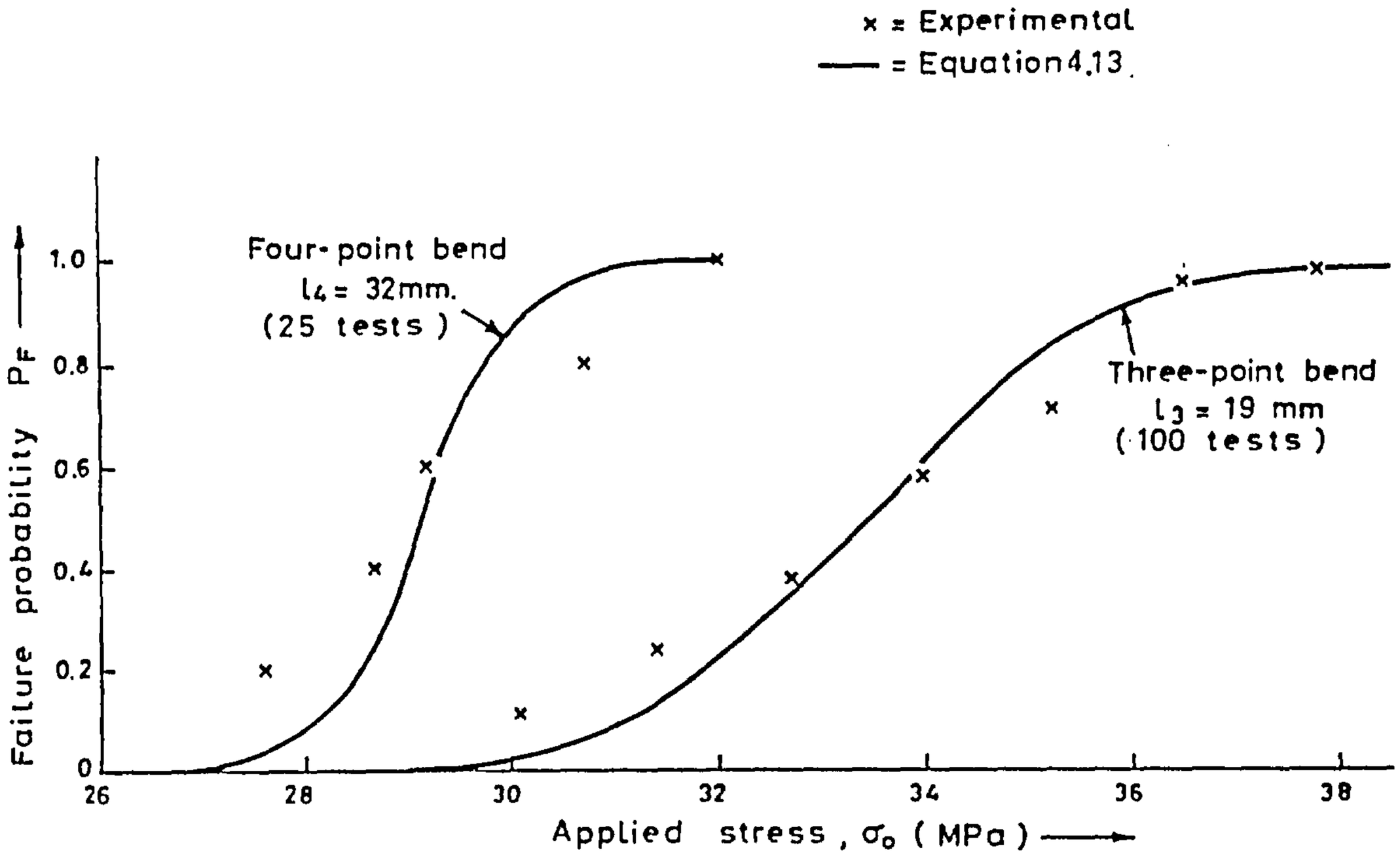

Figure 4.6: A comparison of measured and predicted failure probabilities for pitchcoke graphite in three- and four-point bend.

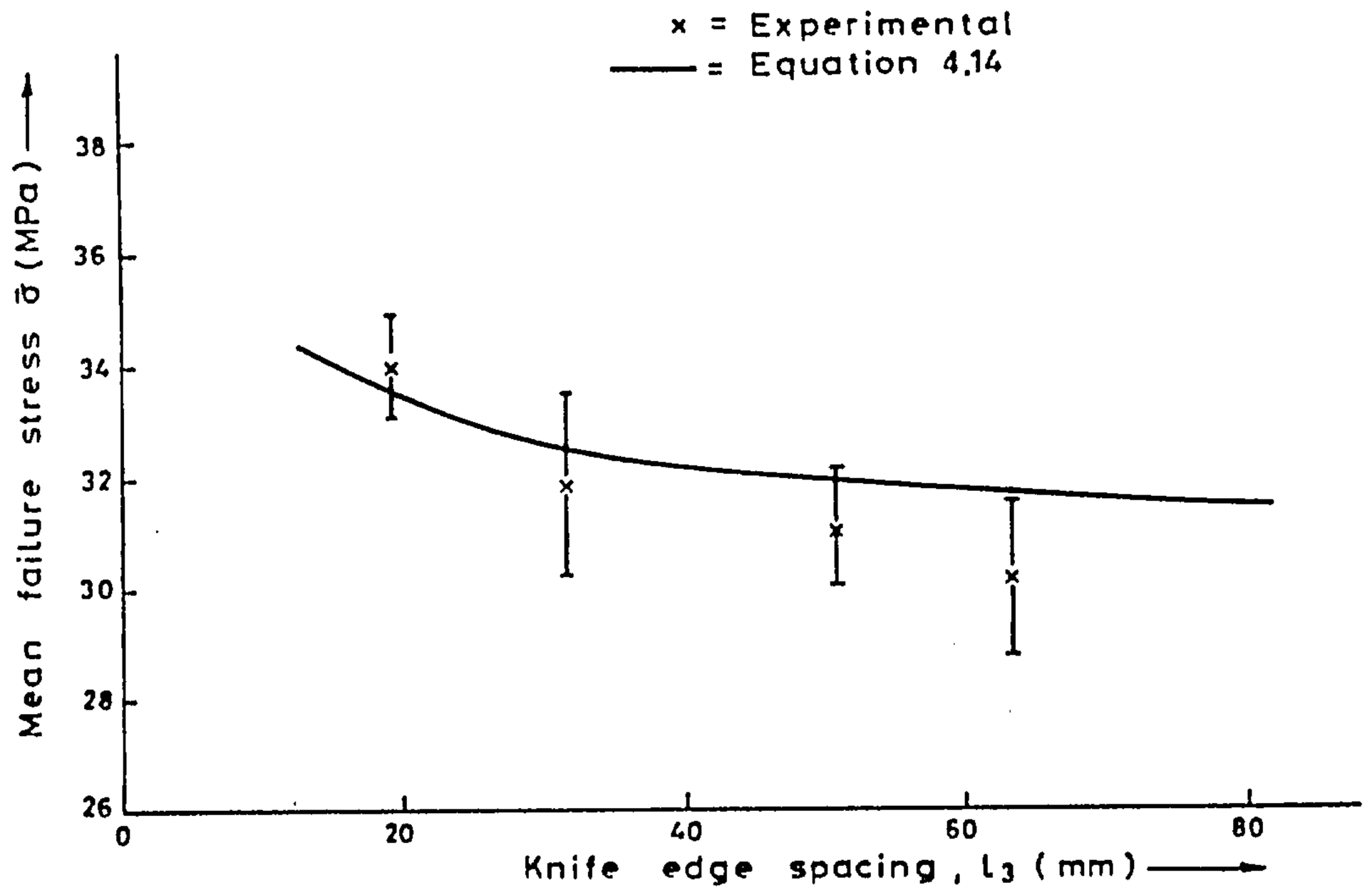

Figure 4.7: The variation of mean failure stress with knife edge spacing for pitchcoke graphite in three-point bend.

point bend strength at the widest knife edge spacing used as the bend strength) is high compared with the experimental ratio of 0.68. Data from other graphites (Brocklehurst, 1974) indicates that the latter value is typical for specimens of this size. This is strong evidence that the theoretical tensile strength is over-estimated. In comparison, a non-linear elastic treatment (Tzung et al., 1981) using couple-stress theory predicts a tensile/bend stress ratio of 0.8 for the specimens used.

4.4.2 IM1-24 graphite

Fracture toughness tests on IM1-24 graphite give a typical K_{Ic} value of 1.5 MPa $m^{\frac{1}{2}}$ (Birch et al., 1983) which is therefore used in the model. The microstructure of IM1-24 is slightly finer than pitchcoke but from the above discussion any differences are second order effects in the model such that all other input parameters are assumed unchanged.

A comparison of experimental and theoretical mean failure stresses is shown in Table 4.2. Agreement in the bend cases is very good but again the tensile strength is over-predicted. The distribution of strengths about the mean is not shown but it is similar to the pitchcoke results in that a wider spread than the model predicts is obtained. Thus the tests on IM1-24 reveal essentially the same deficiencies in the model as found for pitchcoke graphite.

4.5 Conclusions

The three-dimensional model accurately predicts both mean failure stress in bending and the variation of bend strength with test and specimen geometry. Against this, the tensile/bend strength ratio is over-predicted and the distribution of strengths is under-predicted. The reasons why this is so lie in the simplifying

assumptions made. For example there is a distribution of particle sizes in the graphite whereas two discrete values have been chosen. Furthermore, no account has been taken of defect interactions, that is the possibility that the stress field ahead of a sub-critical crack will enhance the probability of cleavage failure in surrounding particles. However, the fundamental physical basis of the model has been justified with the results obtained.

CHAPTER 5

A TWO-DIMENSIONAL MODEL OF FRACTURE

5.1 Introduction

It is paradoxical to develop the three-dimensional model of the previous chapter into a two-dimensional calculation but there is a good reason for adopting this approach. The point was made at the outset that the objective of this work is to develop a general fracture criterion. As a consequence of the complex geometry of graphite components it is usually only possible to determine in-service stresses using finite element computational techniques. In such calculations it would be impossibly complex to attempt to include a semi-circular crack in the calculation as required by the three-dimensional model. Indeed finite element methods are restricted whenever possible to two-dimensional representations and insertion of a defect in a third dimension is inappropriate.

The statistical approach of section 4.3 is still entirely valid in two dimensions and so this is retained in the new model. However, the microstructural input parameters are rationalised such that only a single particle radius, taken to be 0.5 mm, is considered. This change has minimal effect on the previous predictions and removes an unnecessary complication from the analysis.

5.2 Number of Initiation Sites

A drawback to the previous model is that the number of initiation sites is rigidly defined in bend and tension. Under general loading this assumption is untenable as some fraction of particles will be subjected to a tensile stress greater than the cleavage stress and will therefore be possible initiation sites.

Consider the column of material residing beneath a single particle situated in the most tensile surface of the beam. In

calculating the nucleation probability exactly it would be necessary to consider the individual probabilities associated with each particle in the column in which the applied stress exceeded S_c. Although this in itself creates no great difficulty the subsequent treatment of propagation from each nucleation site would be prohibitively complex. Therefore, the simplifying assumption is made that with each particle in the most tensile surface there is an associated total of m nucleation sites, where m is chosen to give the same probability of nucleation as in the exact calculation. The value of m, chosen as described below, may vary between zero and h/2A, this latter quantity being the number of particles across the beam height.

Consider a bar under a tensile stress σ_t and pure bend stress σ_b as shown in Figure 5.1. The total stress at position x is

$$\sigma(x) = \sigma_b \ (2x/h - 1) + \sigma_t \qquad (5.1)$$

x being measured from the position of minimum stress. Using equation 4.5 and taking a line of particles from x = 0 to x = h associated with a single particle on the top surface, the total probability of there being a nucleation site on the line is

$$1 - \prod_{n=x_o/2A}^{h/2A} [1 - (1 - \sqrt{S_c/\sigma(x)})] \qquad (5.2)$$

where $x = 2An$ and x_o is the position at which $\sigma(x_o) = S_c$. Thus x_o is defined by the equation

$$\sigma_b \ (2x_o/h - 1) + \sigma_t = S_c \ ,$$

or

$$x_o = \frac{h}{2} \ (1 + (S_c - \sigma_t)/\sigma_b) \quad x_o > 0. \qquad (5.3)$$

Since all nucleation sites are treated as surface ones, and there are m of these per line of particles the total probability of a single site being activated is

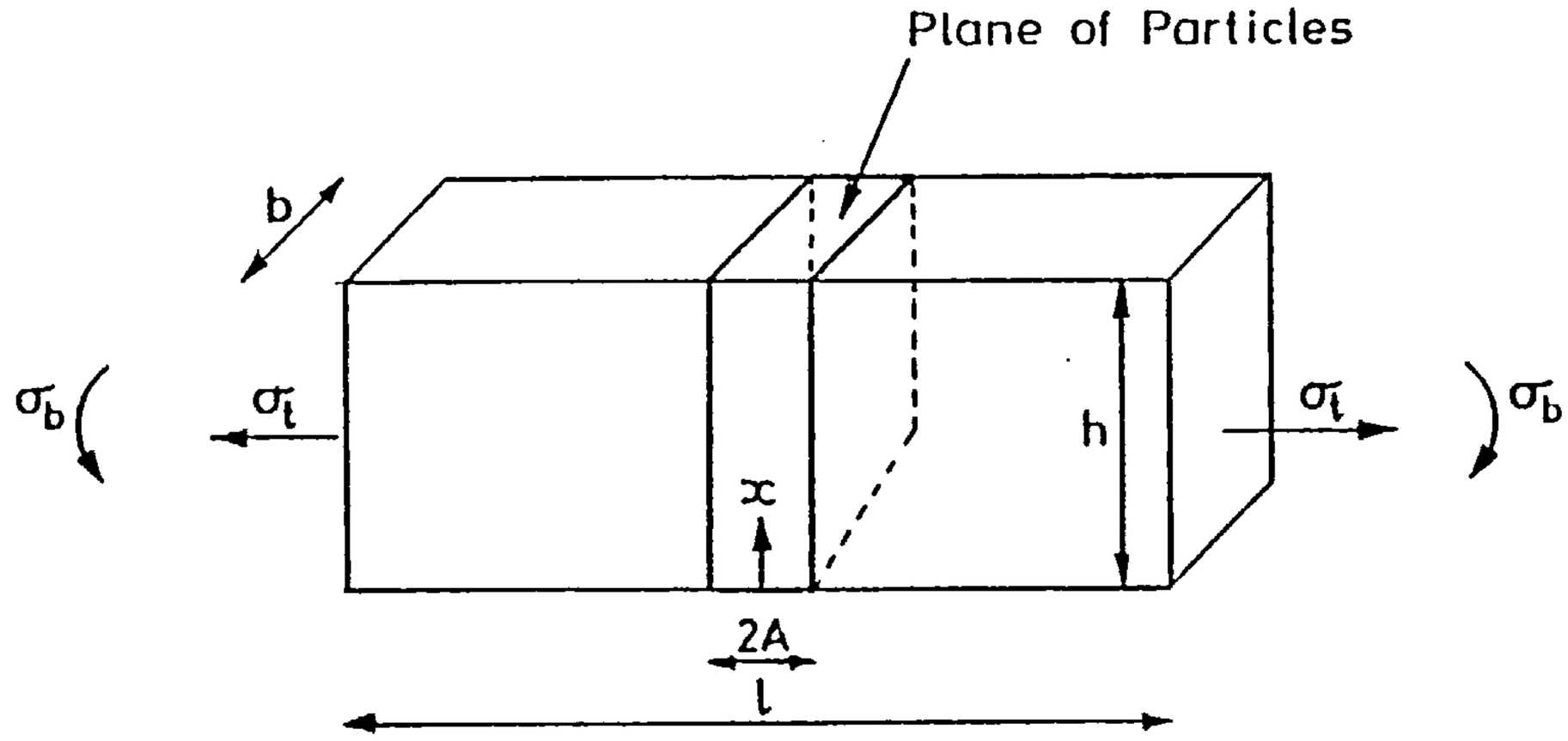

Figure 5.1: A schematic representation of a beam under combined tension and pure bending.

$$1 - [S_c/\sigma(h)]^{m/2} \tag{5.4}$$

where $\sigma(h) = \sigma_b + \sigma_t$ and this will be identical to (5.2) if

$$[S_c/\sigma(h)]^{m/2} = \prod_{n=x_o/2A}^{h/2A} [S_c/\sigma(x)]^{\frac{1}{2}} . \tag{5.5}$$

Squaring both sides and taking logarithms

$$m \ln [S_c/\sigma(h)] = \sum_{n=x_o/2A}^{h/2A} [\ln S_c/\sigma(x)] . \tag{5.6}$$

This may be alternatively evaluated by replacing the summation with an integral giving

$$m \ln [S_c/\sigma(h)] = \int_{x_o/2A}^{h/2A} \ln [S_c/\sigma(x)]dn$$

$$= \frac{1}{2A} \int_{x_o}^{h} \ln [S_c/\sigma(x)]dx$$

Thus

$$m = \frac{\int_{x_o}^{h} \ln [S_c/\sigma(x)]dx}{2A \ln [S_c/\sigma(h)]} . \tag{5.7}$$

The total number of initiation sites under tension, bend or combined stress is then given by

$$n = m \ 3b\ell/2\pi A^2 \tag{5.8}$$

and the inconsistency in the value of n in different stress distributions has been removed.

5.3 Calculation of Critical Crack Size

To develop a failure criterion capable of inclusion in a finite element calculation the critical defect must be represented as a two-dimensional slot, that is one extending to infinity in the direction perpendicular to the plane section under consideration. Such a slot of depth c has a much larger stress intensity factor K_{2D}, than that

for a semi-circular crack K_{3D}, of radius c. Yet to apply the statistical model of fracture it is essential to determine the radius c previously calculated from the fracture mechanics condition $K_{3D} = K_{Ic}$. If from finite element techniques we only have a knowledge of K_{2D} then c is under-estimated if the condition $K_{2D} = K_{Ic}$ is applied. The appropriate value of c is available if an effective critical stress intensity factor YK_{Ic} is defined where $Y = K_{2D}/K_{3D}$, but this is only valuable if it can be shown that Y is reasonably constant for different loading conditions and different crack depths. Let us adopt this approach and following equation 4.15 define K^*_{2D} at criticality by the equation

$$K_{Ic} = \sigma h^{\frac{1}{2}} K^*_{2D}/Y \ . \qquad (5.9)$$

As for the three-dimensional case K^*_{2D} depends only on the ratio (c/h), and does so according to the equations

$$K^*_{2D} = \left(\frac{\pi c}{h}\right)^{\frac{1}{2}}\left[1.12 - 0.23\left(\frac{c}{h}\right) + 10.6\left(\frac{c}{h}\right)^2 - 21.7\left(\frac{c}{h}\right)^3 + 30.4\left(\frac{c}{h}\right)^4\right]$$

$$\text{(tension)} \quad \frac{c}{h} < 0.6$$

$$= \left(\frac{\pi c}{h}\right)^{\frac{1}{2}}\left[1.12 - 1.39\left(\frac{c}{h}\right) + 7.32\left(\frac{c}{h}\right)^2 - 13.1\left(\frac{c}{h}\right)^3 + 14.0\left(\frac{c}{h}\right)^4\right]$$

$$\text{(bend)} \quad \frac{c}{h} < 0.6 \qquad (5.10)$$

(Brown and Srawley, 1966).

Figures 5.2 and 5.3 illustrate the variation of K^*_{2D} and K^*_{3D} with (c/h) for tension and bend respectively as given by equations 5.10 and 4.16. In both cases K^*_{2D} is larger than K^*_{3D} at a given (c/h) ratio demonstrating as expected that the two-dimensional K_{Ic} value will always be the greater. Also shown on each figure is the variation of Y with (c/h). In bend Y = 1.5 for (c/h) < 0.2 and for the same range in tension Y tends to 1.6 although it is slightly greater in the range 0.1 < (c/h) < 0.2. For simplicity, it is a reasonable

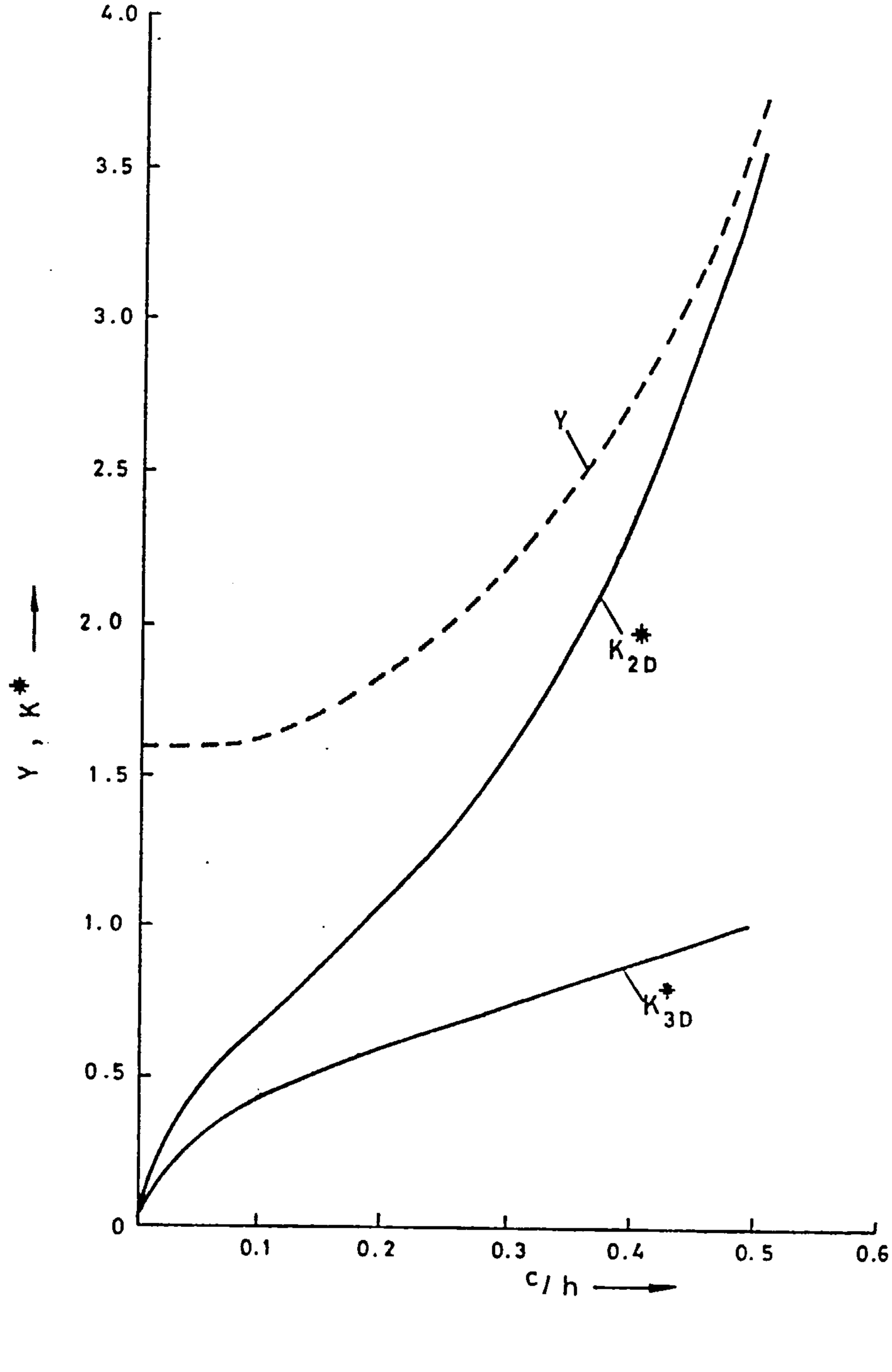

Figure 5.2: The variation of two- and three-dimensional stress intensity factors for defects in tension expressed through the dimensionless quantities $K^* = K_I/\sigma h^{\frac{1}{2}}$ and c/h.

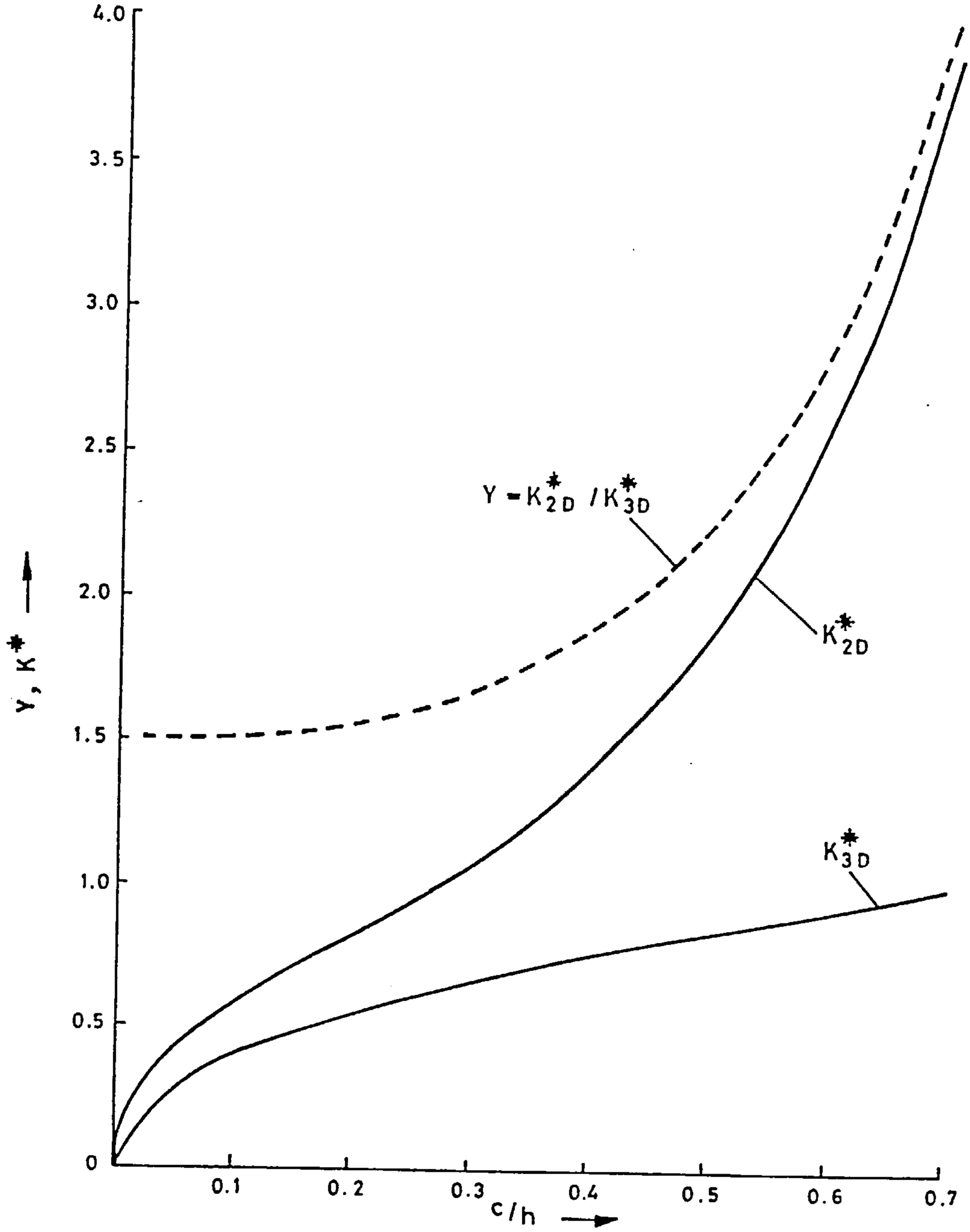

Figure 5.3: The variation of two- and three-dimensional stress intensity factors for defects in bend expressed through the dimensionless quantities $K^* = K_I/\sigma h^{\frac{1}{2}}$ and c/h.

assumption to define a constant value of Y equal to 1.55 for both bend and tension with (c/h) < 0.2. From equations 5.9 and 5.10 the conditions for a valid comparison between the two-dimensional theory and experiment are then

$$\sigma h^{\frac{1}{2}} \gtrsim 1.7 \text{ MPa } m^{\frac{1}{2}} \text{ (pitchcoke)}, \quad \sigma h^{\frac{1}{2}} \gtrsim 2.1 \text{ MPa } m^{\frac{1}{2}} \text{ (IM1-24)} \quad \text{(tension)} \tag{5.11}$$

$$\sigma h^{\frac{1}{2}} \gtrsim 2.2 \text{ MPa } m^{\frac{1}{2}} \text{ (pitchcoke)}, \quad \sigma h^{\frac{1}{2}} \gtrsim 2.8 \text{ MPa } m^{\frac{1}{2}} \text{ (IM1-24)} \quad \text{(bend)}.$$

Hence confidence in this approach improves with larger specimens or stronger graphites. From Table 4.1 for pitchcoke graphite, the lowest measured bend strength is 29.1 ± 1.7 MPa. At the 95% confidence level (two standard deviations lower than the mean) $\sigma h^{\frac{1}{2}} = 2.4$ MPa $m^{\frac{1}{2}}$ which is in the valid region. For tension, the equivalent value is $\sigma h^{\frac{1}{2}} = 1.65$ MPa $m^{\frac{1}{2}}$ which from equation 5.11 is invalid. However, the agreement between theoretical and experimental mean tensile strengths indicates that there is no sharp discontinuity in the model performance and therefore that the definition of validity is arbitrary. From Table 4.2 for IM1-24 graphite, all bend test predictions are valid and for the tensile tests listed $\sigma h^{\frac{1}{2}} = 2.1$ MPa $m^{\frac{1}{2}}$ which is within the acceptable range. Hence with the exception of the tensile data on pitchcoke graphite all the tests done may be modelled with a two-dimensional critical defect.

5.4 Results and Discussion

5.4.1 Input parameters

Changes in parameters from the three-dimensional model are that the effective fracture toughness is increased by a factor of 1.55 and a single particle radius of 0.5 mm is considered. Figure 5.4 lists all the values used for pitchcoke graphite together with the resulting change in three-point bend strength on adjusting each one

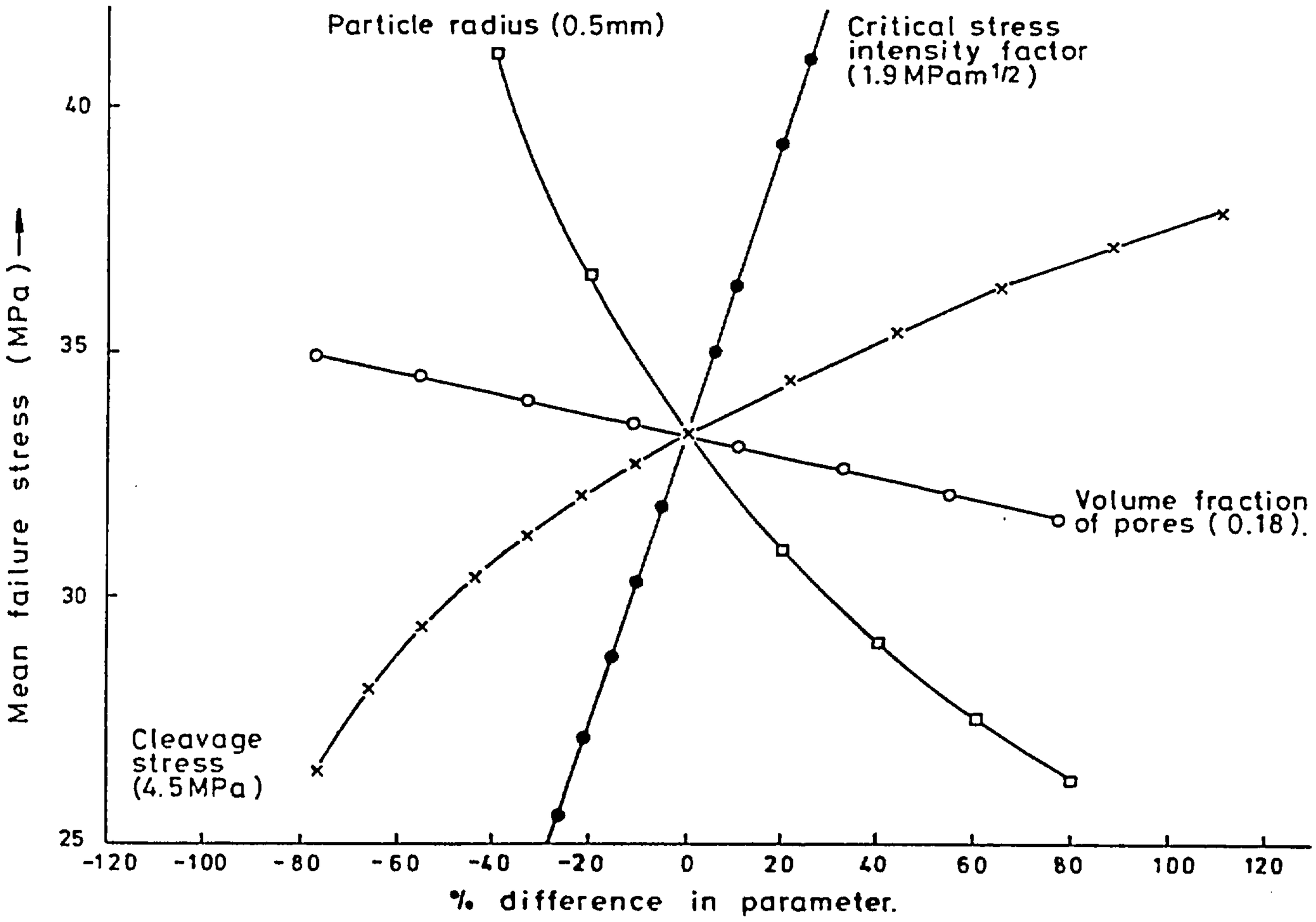

Figure 5.4: The effect of individually varying each input parameter for pitchcoke graphite on predicted mean failure stress in three-point bend.

independently. This figure should be treated with caution as some parameters are interlinked. However, the figure does show the relative ranking of each quantity. The sensitivity to K_{Ic} is dominant with strength rising linearly with toughness as expected from the Griffith relation (equation 2.4). The particle size and volume fraction parameters of the three-dimensional model have been combined such that the single particle radius becomes the second ranked variable. Note the insensitivity to porosity changes. This arises from the assumption that pores are particles with zero cleavage stress. Pickup (1984) has shown that thermal oxidation develops fine crack-like porosity causing an exponential decrease in fracture toughness with burn-off, largely controlled by the exponential decrease in Young's modulus. Hence a change in both the volume fraction of porosity and K_{Ic} is required to model the resulting strength change. He also confirms that radiolytic oxidation tends to increase the diameter of existing smaller pores which does not reduce the strength as severely as thermal oxidation to the same burn-off. This situation is closer to that of Figure 5.4 showing an increase in porosity without change in fracture toughness.

5.4.2 Stresses at failure

Tables 4.1 and 4.2 show the two-dimensional model predictions for mean failure stresses of previously described tests on pitchcoke and IM1-24 graphites respectively. It is seen that the bend results show the same close agreement as before. The only valid comparison for tensile data is for IM1-24 and this again over-predicts tensile strength although by an amount reduced from the previous 26% to only 7%. Consequently, the theoretical tension/4-point bend ratio of 0.70 is close to the experimental value of 0.68. The reason for the better agreement lies in the method of determining the critical crack

size explained in section 5.3. Choosing a composite value of Y equal to 1.55 has the effect of weakening the material in tension relative to bending and brings prediction better into line with observed behaviour.

Figure 5.5 illustrates the cumulative failure probability distribution in three-point bend for both graphites examined. The close agreement between the two models is evident. For pitchcoke the failure probability is under-estimated at low stress by both models. For IM1-24 this is not as evident but the predicted mean failure stress is slightly low which disguises the fact that the spread of strengths is greater than the models allow.

5.4.3 Specimen volume effects

The extensive series of bend and tensile tests on IM1-24 graphite discussed in Chapter 2 (Brocklehurst, 1974) may be used in a comparison with the two-dimensional model predictions of mean failure strength, as shown in Figure 2.1. From this figure it is evident that the reducing strength at smaller specimen volumes is not predicted in either stress state. Thus there is no account taken in the model of the weakening that occurs when any linear dimension of the specimen is less than approximately ten particle diameters. In bend at larger volumes (> 1 cm^3), the dependence of strength on volume is slightly under-predicted but reasonable correlation between theory and experiment is obtained. Exact specimen dimensions are not quoted by Brocklehurst such that the two-dimensional model prediction may be displaced approximately ± 1 MPa from the line drawn, depending on the specimen depths and widths, although the slope of the line remains unchanged. The variation in tensile strength with volume is predicted to be similar to that in bend. This is contrary to. observation. It is probable that the different experimental

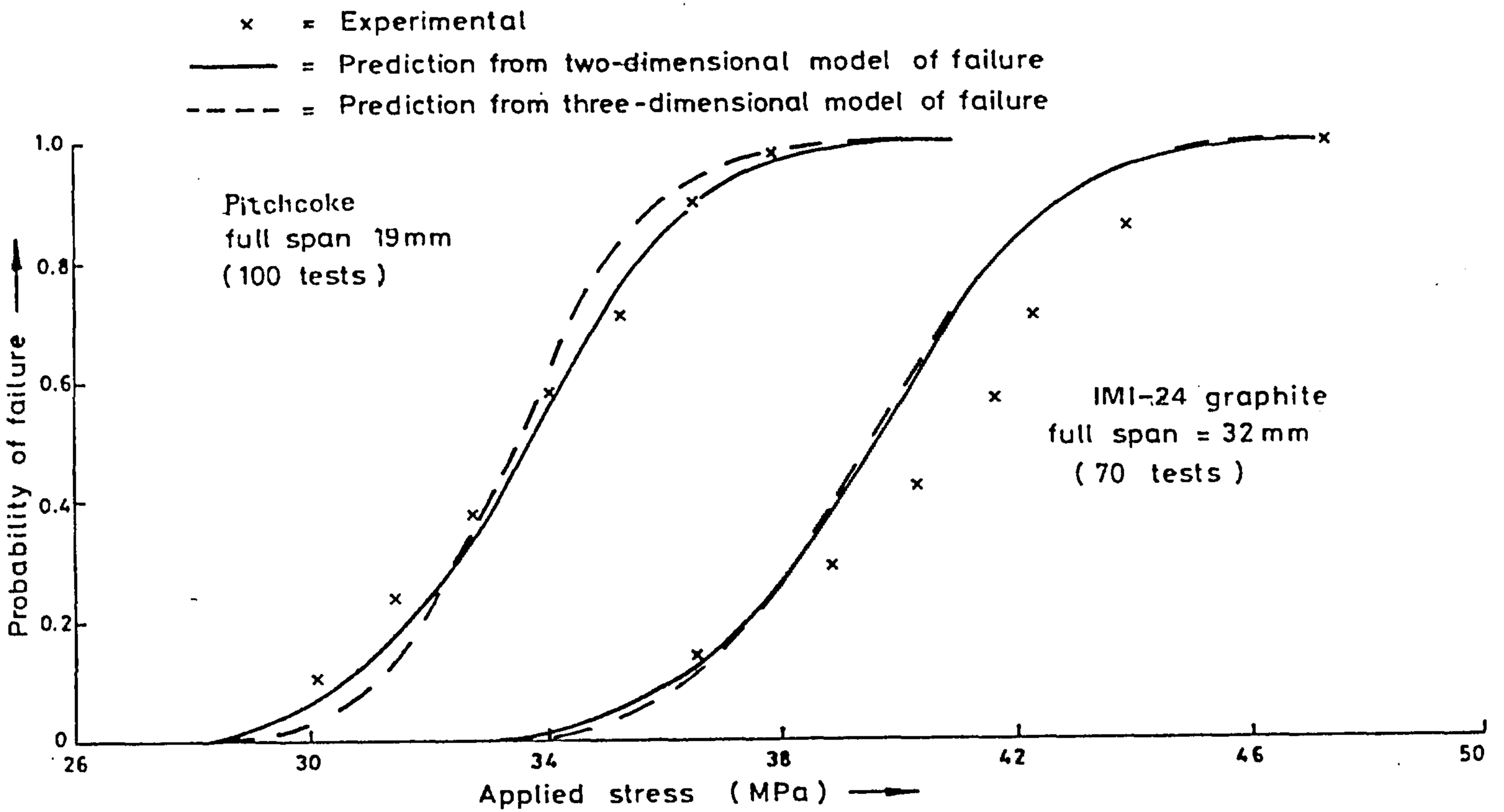

Figure 5.5: A comparison of measured and predicted failure probabilities in three-point bend tests on pitchcoke and IM1-24 graphites.

behaviour between the two cases is due to the greater weakening effect in a uniform stress field of a small number of particles across the specimen section. That is in tension, failure of a particle causes a more severe stress intensification upon its neighbours than in bend. The mechanism by which this occurs is not taken into account in the model so resulting in the discrepancy between theory and experiment.

5.4.4 Stress gradient effects

It has been shown that the decrease in three-point bend strength with decrease in stress gradient in the direction normal to the crack is well predicted. However, it is also possible to decrease the stress gradient in the direction of crack growth by using specimens of greater depth. Brocklehurst (1974) has reported failure data for such specimens of IM1-24 graphite at a constant volume of 24.6 cm^3 and depth 3.2 → 50.8 mm. Again, strength decreases as the stress gradient is reduced, results ± one standard deviation from sets of six specimens being shown in Figure 5.6. As in the case of the volume data, specimen sizes are not known so that the model prediction may be displaced by approximately ± 1 MPa. With this proviso, the predicted strength variation is similar to that observed in practice. At lower stress gradients the strength is reduced as the stress in the crack propagation region tends to the maximum ligament tensile stress. At stress gradients $\gtrsim$ 9.6 GPa $m^{\frac{1}{2}}$ (beam height $\lesssim$ 7 mm) the relevant condition (5.11) is no longer met and therefore the model is invalid. Ideally more data of this type is necessary for a thorough comparison of theory and experiment.

5.5 Biaxial Tension

Consider principal stresses σ_1 and σ_2 (= $x\sigma_1$ where $x < 1$) acting on a particle with its cleavage plane at angle ϕ to σ_1. Following

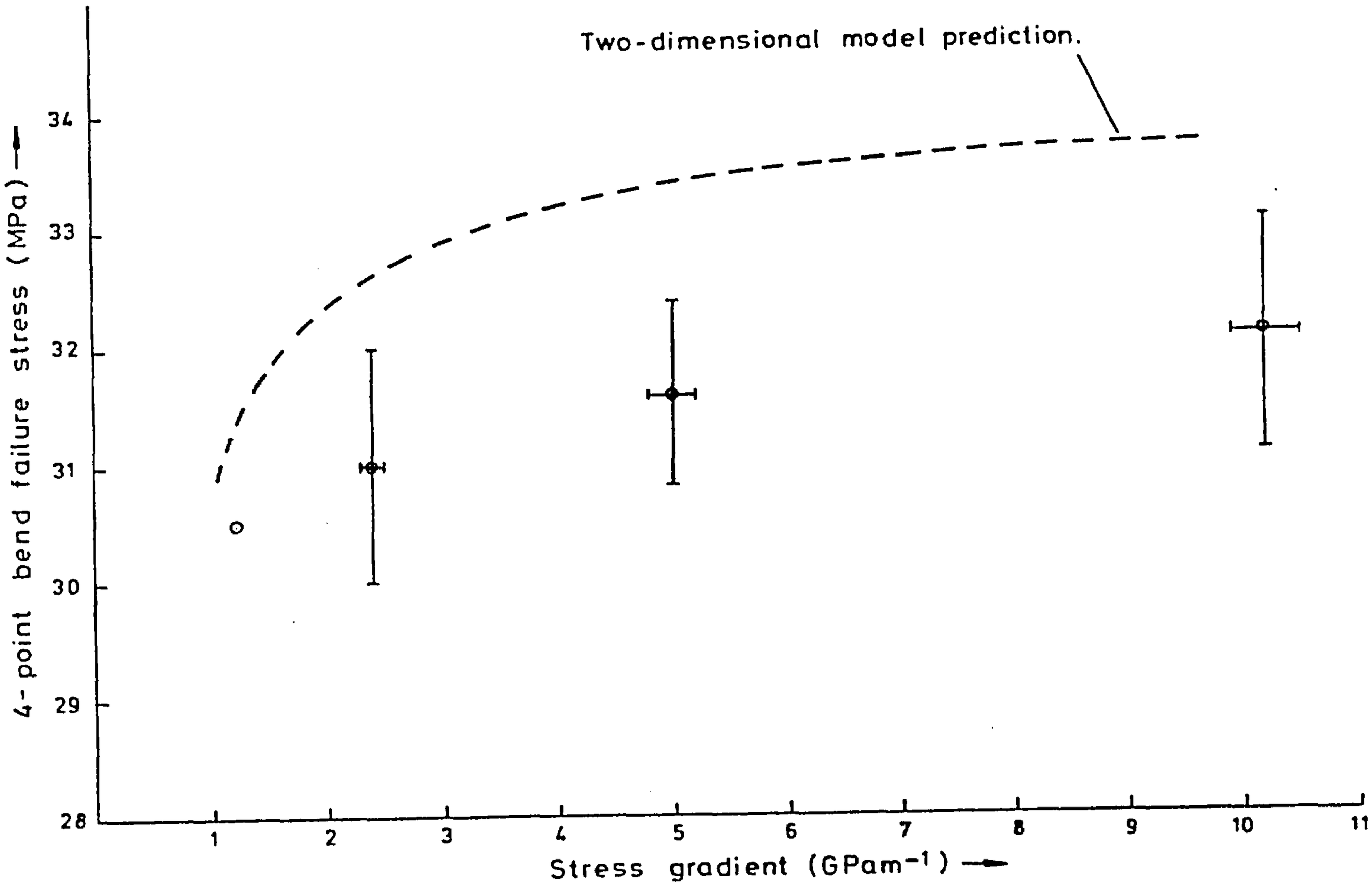

Figure 5.6: Mean failure stress of constant volume four-point bend specimens of IM1-24 graphite as a function of stress gradient in the direction of crack growth.

equation 4.2 for uniaxial stress, the cleavage condition in biaxial tension is

$$\sigma_1 \cos^2\phi + x\sigma_1 \sin^2\phi \geq S_c$$

which may be written

$$\cos^2\phi \geq 1 - \left(\frac{1 - S_c/\sigma_1}{1 - x}\right) . \qquad (5.12)$$

Hence using equation 4.4, the probability of the particle cleaving is

$$\begin{aligned} P_c &= 1 - \left[1 - \left(\frac{1 - S_c/\sigma_1}{1 - x}\right)\right]^{\frac{1}{2}} && x \leq S_c/\sigma_1 \leq 1 \\ &= 0 && \sigma_1 \leq S_c \\ &= 1 && S_c/\sigma_1 < x. \end{aligned} \qquad (5.13)$$

When x = 0 this equation reverts to the uniaxial case of equation 4.5. Crack propagation may be considered in an identical manner replacing the square root term in equation 4.6 and the appropriate regions of validity with equation 5.13. Thus the fracture statistics of section 4.3 may be applied to biaxial tension.

It is now necessary to define the critical defect size. In a rigorous treatment all orientations of the critical defect should be considered such that the overall probability of failure is given by

$$P_F = 1 - \prod_{\phi=0^o}^{\phi=90^o} (1 - P_f(\phi)) \qquad (5.14)$$

with the critical crack size used in the calculation of each $P_f(\phi)$ chosen according to the resolved tensile stress on each plane ϕ. However, when $\sigma_1 >> \sigma_2$, the only significant contribution to failure will come from the maximum principal stress σ_1. Hence equations 5.9 and 5.10 with $\sigma = \sigma_1$ may be used to give the critical crack radius. When $\sigma_2 \rightarrow \sigma_1$ this breaks down and it is strictly necessary to integrate over all planes to determine the overall probability of failure. A first approximation to this is to use equations 5.9 and

5.10 and consider failure from the two principal stress directions alone. In this case the overall probability of failure is

$$P_F = 1 - (1 - P_{f(\phi=0^o)})\ (1 - P_{f(\phi=90^o)}). \qquad (5.15)$$

Figure 5.7 shows a comparison of equation 5.15 with experiment using biaxial data normalised to a uniaxial tensile strength of unity. The failure criteria listed are all discussed in section 2.2. Specimens used in these tests are hollow cylinders which are concurrently pulled axially and pressurised internally. A coating or thin protective sleeve is placed around the inner wall of the cylinder to prevent hydraulic fluid entering the open pores. It is evident that there is a large uncertainty in the experimental data but for $\sigma_1 \approx \sigma_2$ the biaxial strength is generally lower than uniaxial. The microcrack model predicts a small decrease in mean failure stress in this region although with the limited data available it is impossible to choose any one criterion which best represents the failure envelope.

5.6 Combined Bend and Tension

As the analysis of section 5.2 has been incorporated into the model there is now no discontinuity in the number of initiation sites in bend or tension. A combination of these two loadings is not typical of any laboratory test but it is a likely situation in actual components. For example, a cylinder such as a CAGR fuel element sleeve may see a tensile stress component due to internal pressurisation and a simultaneous bending component due to an impact. In cases of this nature it is difficult to test the whole component and therefore a model of failure is highly desirable. By defining the critical defect radius from a superposition of equations 5.9 and 5.10 for the tensile and bend components respectively, the combined

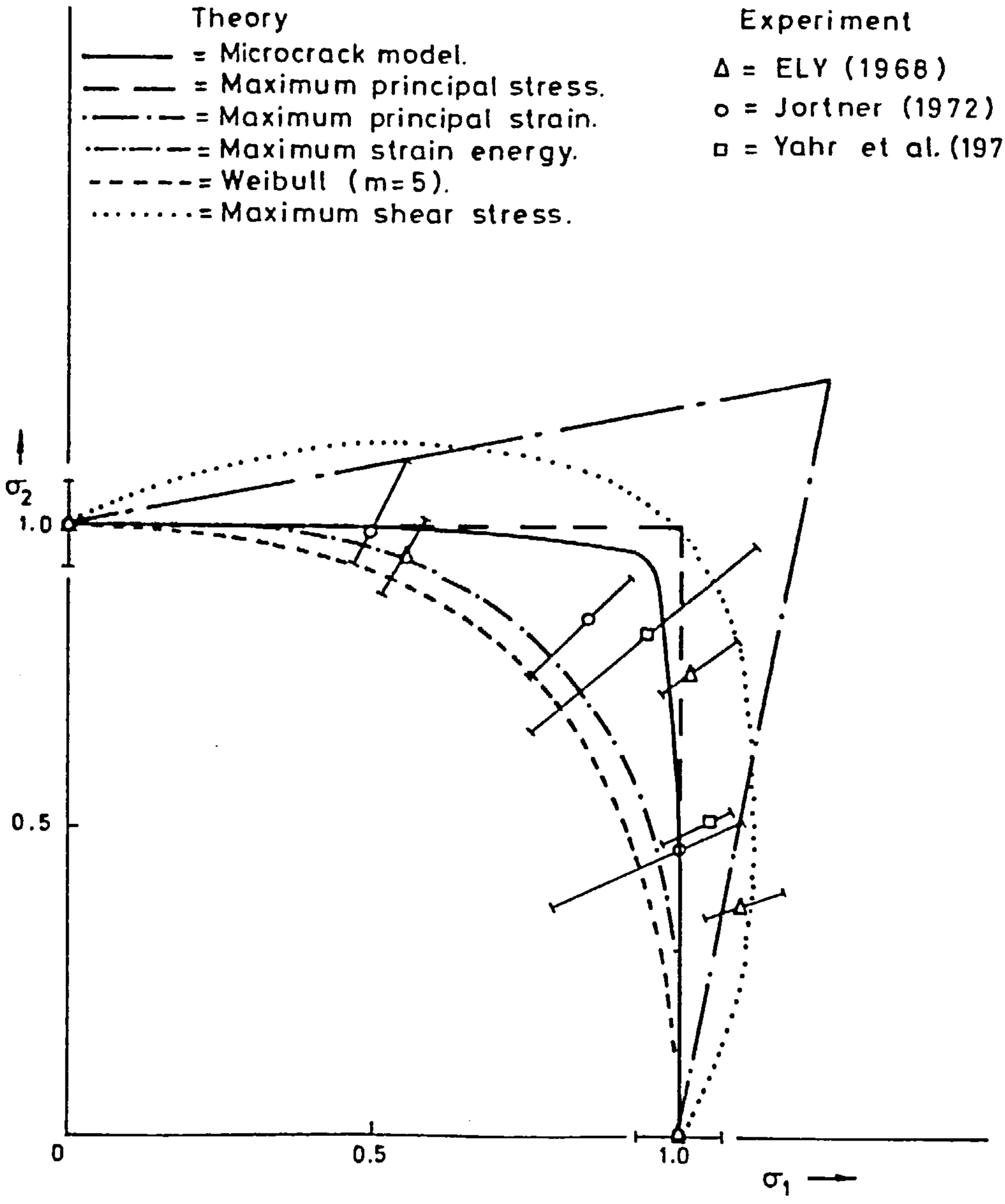

Figure 5.7: Experimental and theoretical failure envelopes in biaxial tension.

stress case may be considered with the model developed.

Figure 5.8 shows the two-dimensional model predictions of mean failure stress under combined loading for specimens of IM1-24 graphite of size equal to the four-point bend specimens of Table 4.2. The mean tensile and four-point bend strengths are as expected from Figure 2.1. The model suggests that it is appropriate to assume a linear failure envelope between the two intercepts, the linear criterion being slightly pessimistic in regions of approximately equal bend and tension.

5.7 Conclusions

The simplification involved in developing the two-dimensional model from the previous three-dimensional model has resulted in virtually identical predictions of probability of failure and mean failure stress in bend and has improved similar predictions in tension. The two-dimensional model has been applied to cases of biaxial tension and combined bend and tension with reasonable success. A deficiency in both models has been identified in that they do not predict the observed decreases in bend and tensile strengths at small specimen volumes. However, the versatility of the two-dimensional treatment is such that there is benefit to be gained by applying it to further situations.

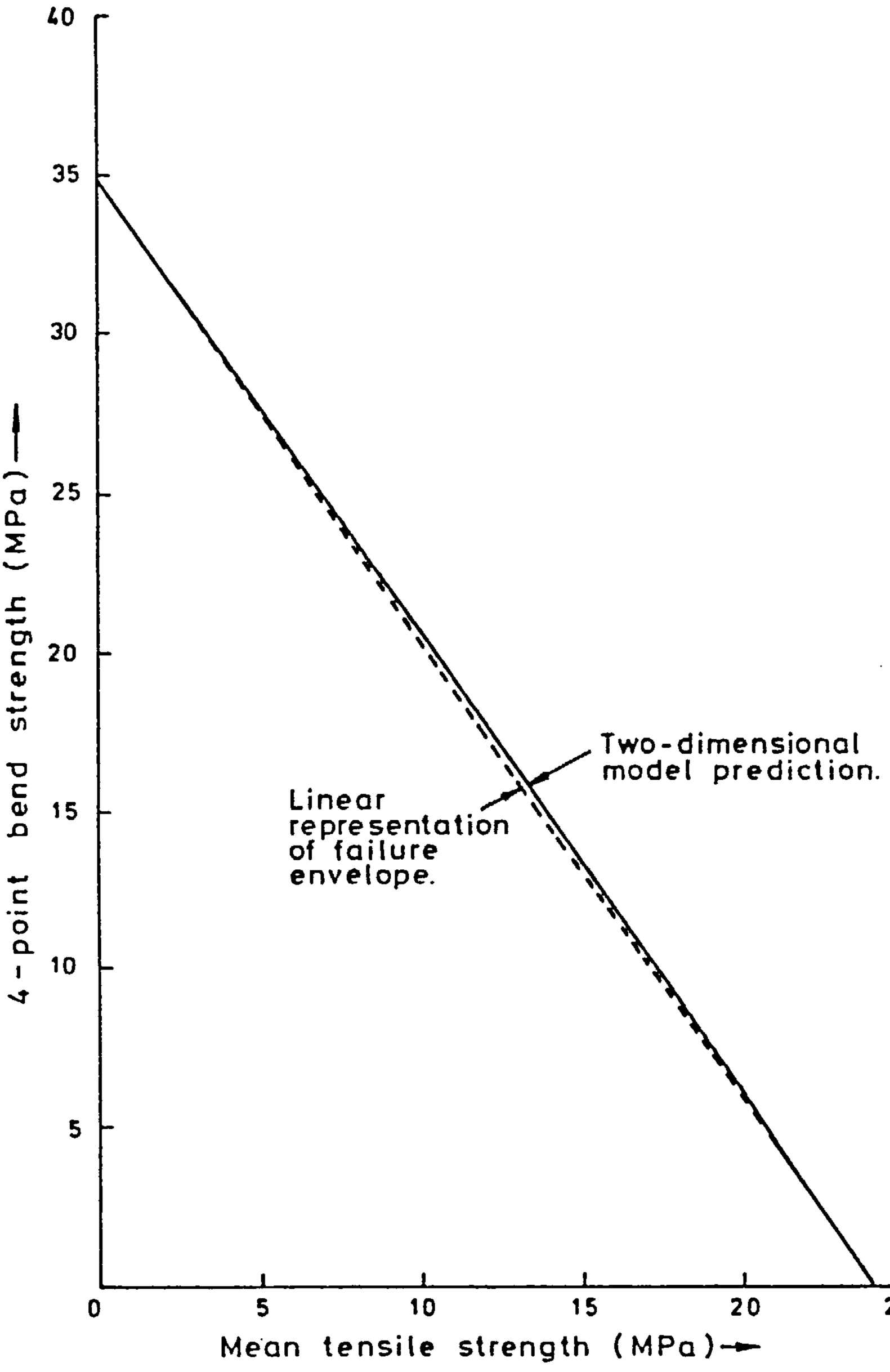

Figure 5.8: The predicted mean failure stress of IM1-24 graphite in combined tension and pure bending.

CHAPTER 6

FRACTURE FROM A NOTCH

6.1 Introduction

Up to now only fracture from undefected material has been considered. This chapter extends the failure model to cover the case of fracture from a sharp notch in the specimen. Although graphite is not as sensitive to notches as elastic theory predicts, stress concentrations of up to twice the applied stress may be present in some components. Hence it is desirable that any failure criterion is continuous in its application to un-notched and notched material in different stress distributions. Initially, a series of notched bend tests are discussed with the object of determining the critical stress intensity factor K_{Ic}. Use of small beam specimens is highly cost effective if it can be shown that reliable fracture toughness measurements are obtained and the importance of K_{Ic} to the fracture model has been well established. In the light of these tests failure from a notch is considered, so advancing the analysis of Chapter 5 to a more general specimen.

6.2 Experimental

All experiments were performed on pitchcoke graphite. Details of specimen dimensions, machined notches and bend tests performed are shown in Figure 6.1. Tests were such that the direction of tensile stress was perpendicular to the extrusion direction. Thirty curved bar specimens were tested without notches and eighty were notched with defects of 0.5 mm root radius and depth from 0.5 to 7.9 mm. From Figure 6.1, type (i) notches had an included angle of 60^{o} and type (ii) vertical sides (0^{o} included angle). No difference in failure loads between these types of notches of the same depth a_{o}, was obtained. Measurements of failure deflection for samples at

(1) 3-Point Bending of Curved Bars, Width b = 12.0 mm.

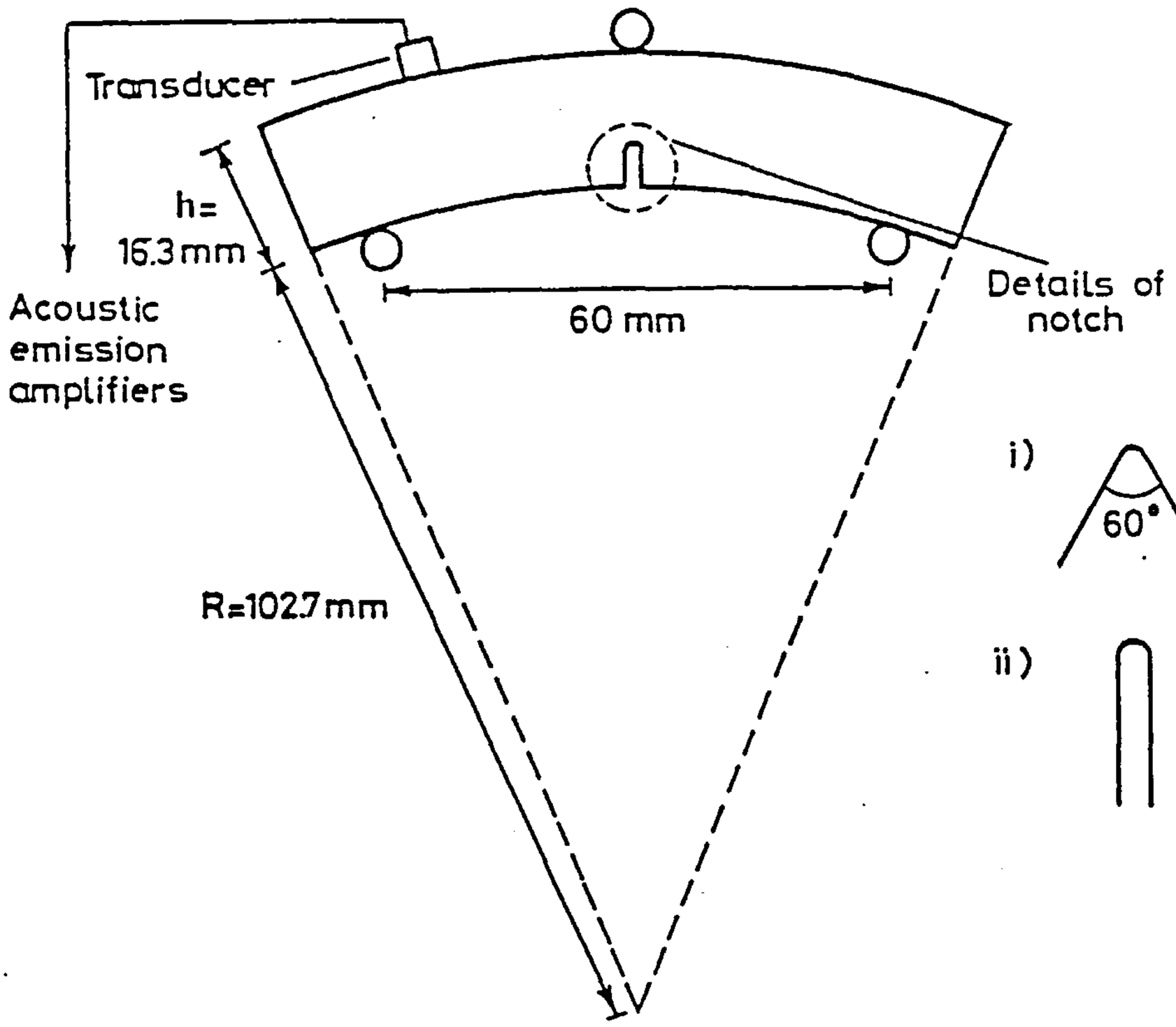

(2) 4- Point Bending of Straight Bars, Width b = 10.0 mm.

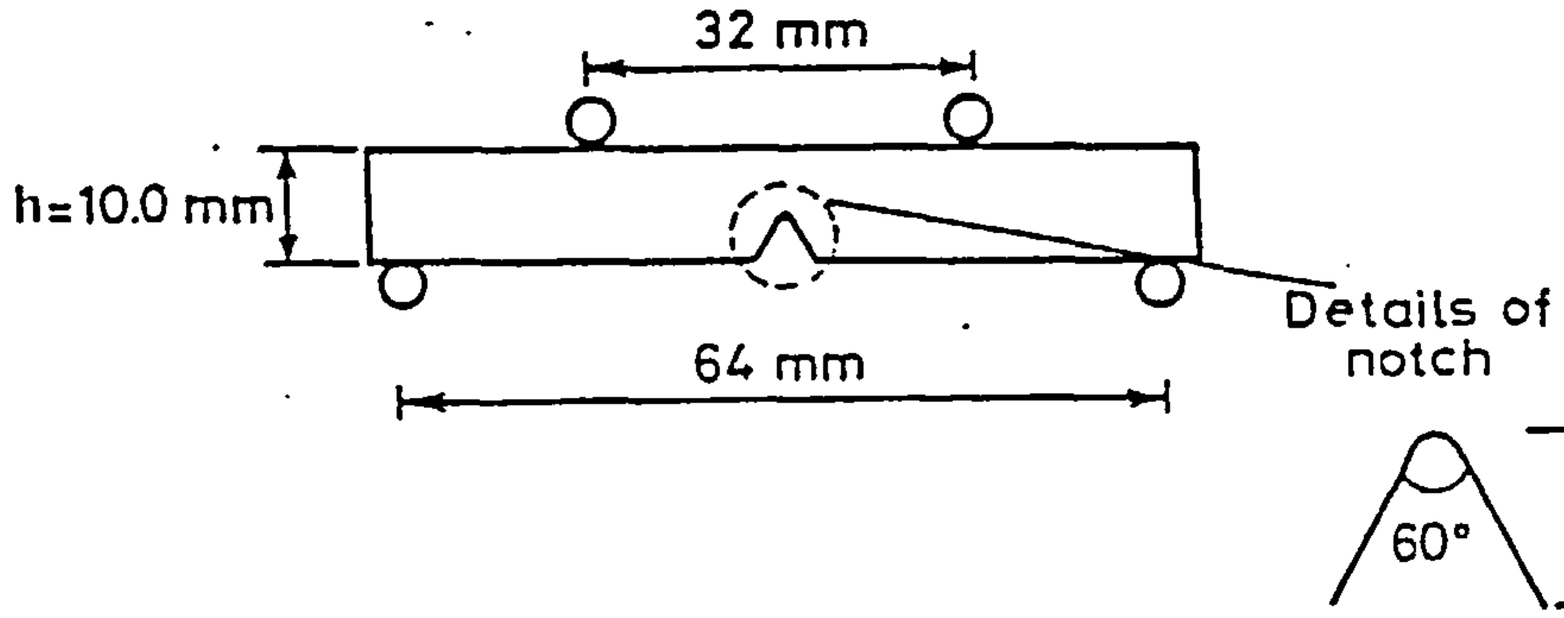

Figure 6.1: A schematic representation of bending tests performed on notched small specimens of pitchcoke graphite.

selected values of a_o throughout the range examined were also made. The variation of acoustic emission response with increasing notch depth was determined using the method described in section 4.2.

Twenty five straight bars were tested intact and sixty were notched with type (i) notches of again 0.5 mm root radius and depth from 0.1 to 3.0 mm. For an elastic test the maximum tensile stress in bending in a curved bar of Figure 6.1 is 5% higher than that in a straight beam of the same thickness and width under identical loading (Timoshenko and Goodier, 1951). Where required therefore the failure stresses of curved beams have been corrected to those of equivalent straight beams.

A small amount of quantitative image analysis of large pore sizes was carried out. The contrast between pores (dark) and material (light) was enhanced by evaporating a thin layer of gold onto a polished graphite surface cut parallel to the extrusion axis. The maximum chord lengths of all pores above a minimum cut off value of 0.3 mm were determined.

6.3 Methods of Assessing Fracture Toughness

6.3.1 Polynomial expressions

Equations 5.9 and 5.10 may be used to calculate fracture toughness from bend tests on notched beams if the notch can be related to a particular sharp crack. In the critical case, K_{Ic} values may then be obtained from the nominal failure stress and the crack depth/specimen depth ratio of the specimen. For equations of this type to be of use in graphite two assumptions are necessary to relate a notch to a crack. Firstly, that there is an effective additional crack below the machined notch due to the flaw distribution present. This is discussed fully in section 6.4 where it is deduced that consistent values of K_{Ic} from bend specimens containing notches of various depths

are obtained by assuming a through thickness additional crack length a_1, of 0.6 mm. Secondly, as there is a distribution of pores already present it is impossible to obtain the normal fatigue sharpened crack used in metallic specimens and therefore a machined defect of length a_o mm and root radius $\sim$ 0.5 mm with a crack of length 0.6 mm at its root is taken to be equivalent to a sharp crack of overall length $(a_o + 0.6)$ mm. The validity of this assumption has been tested using the BERSAFE finite element code and good agreement of calculated stress intensity factors from these two cases was obtained.

6.3.2 Critical crack extension force

A second method of calculating the critical stress intensity factor is to evaluate the critical crack extension force, G_{Ic} per unit length of crack front (equal to the rate of change of energy release with crack extension). In an elastic test the load displacement record may be used to evaluate this quantity. Consider Figure 6.2 which shows a schematic load displacement plot of two elastic lines for samples containing notches of length (a_o) and $(a_o + da_o)$ respectively. The gentler slope of the $(a_o + da_o)$ line reflects the lower effective modulus at an increased notch depth. The specimen notched to length (a_o) fails at load P and deflection δ, and the $(a_o + da_o)$ notched specimen fails at a lower load and deflection, point E. If the specimen (a_o) is loaded to point A then it contains a greater stored energy than specimen $(a_o + da_o)$ at the same deflection, point E, by an amount equal to the area shaded, triangle OAE. Hence going from notch size (a_o) to size $(a_o + da_o)$ the release of energy that provides the crack extension force is given by this area such that for a small increment of crack growth da_o

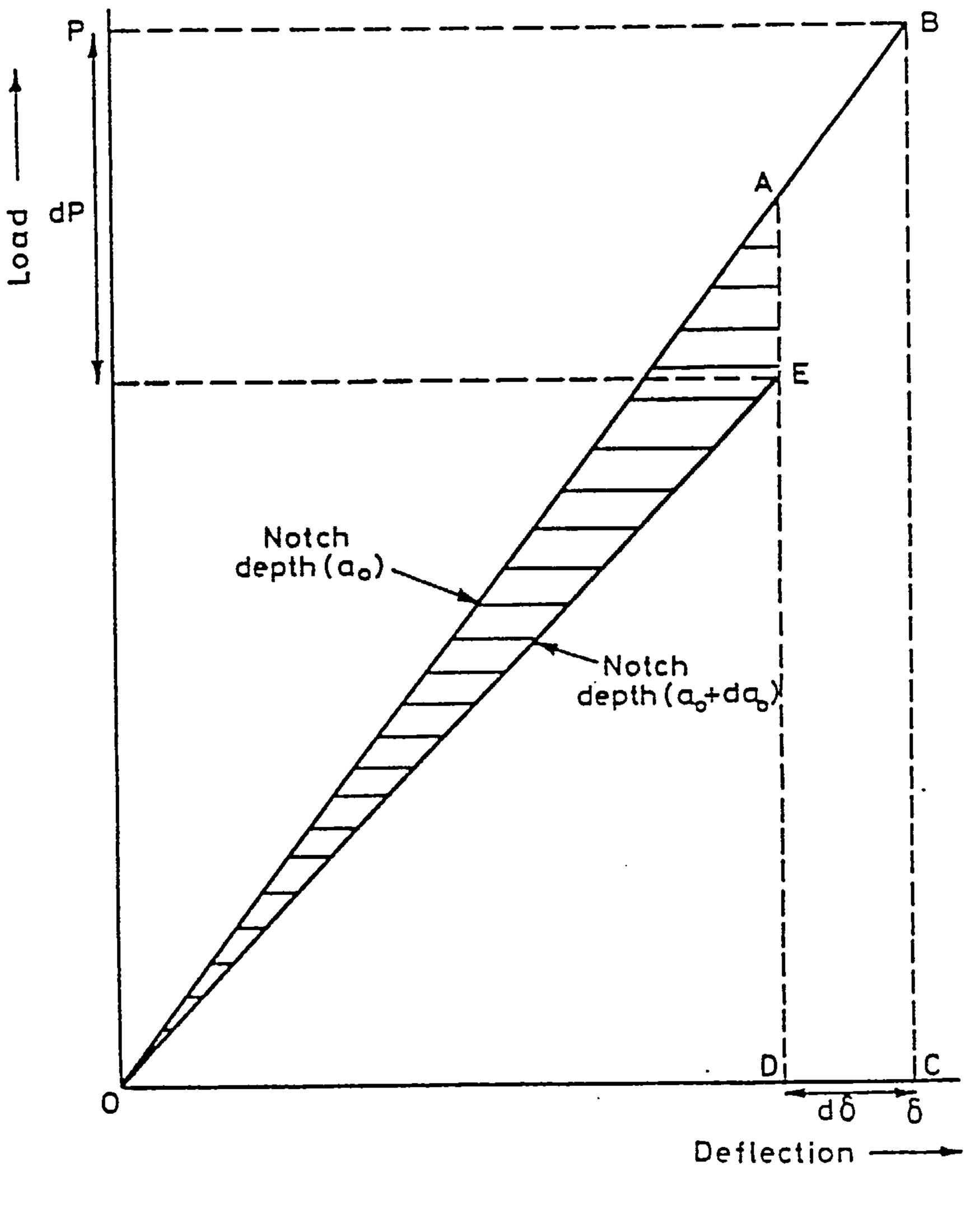

Figure 6.2: A schematic representation of load deflection curves for specimens containing notches of depth (a_o) and (a_o + da_o) respectively.

Energy release = Area triangle OAE = triangle OBC - triangle OED

- rectangle ABCD

$$= \delta dP/2 - Pd\delta/2 \qquad (6.1)$$

where dP and dδ are the associated <u>decreases</u> in failure load and extension. The rate of change of energy release with crack extension in a specimen of width b is then

$$G_{Ic} = (\delta dP/da_o - Pd\delta/da_o)/2b. \qquad (6.2)$$

Thus knowing failure loads and deflections and their variation with notch depth the critical crack extension force may be calculated.

In plane stress G_{Ic} is simply equal to K_{Ic}^2/E where E is Young's modulus. Under plane strain conditions the modulus is replaced by $E/(1 - \nu^2)$ although the low value of Poisson's ratio $\nu < 0.2$, normally assumed for graphite means that this correction may be neglected.

6.4 Results and Discussion

In comparing results from specimens of different geometry it is useful to non-dimensionalise the load and deflection data as a function of notch depth so as to obtain one normalised curve in each case. This may be most conveniently achieved in terms of the failure load P_o and failure deflection δ_o, of identical un-notched beams. Then the non-dimensional failure loads and deflections may be defined as $P' = P/P_o$ and $\delta' = \delta/\delta_o$ respectively. Figure 6.3 shows the variation of P' and δ' with increasing notch aspect ratio. It is seen from the figure that failure deflections remain constant at ~ 0.9 of the un-notched value independent of notch aspect ratio over the range examined. From this data it is possible to a first approximation to simplify equation 6.2 by taking $d\delta/da_o = 0$ and non-dimensionalising dP/da_o such that

$$G_{Ic} = \delta P_o \, (dP'/dx')/2bh \qquad (6.3)$$

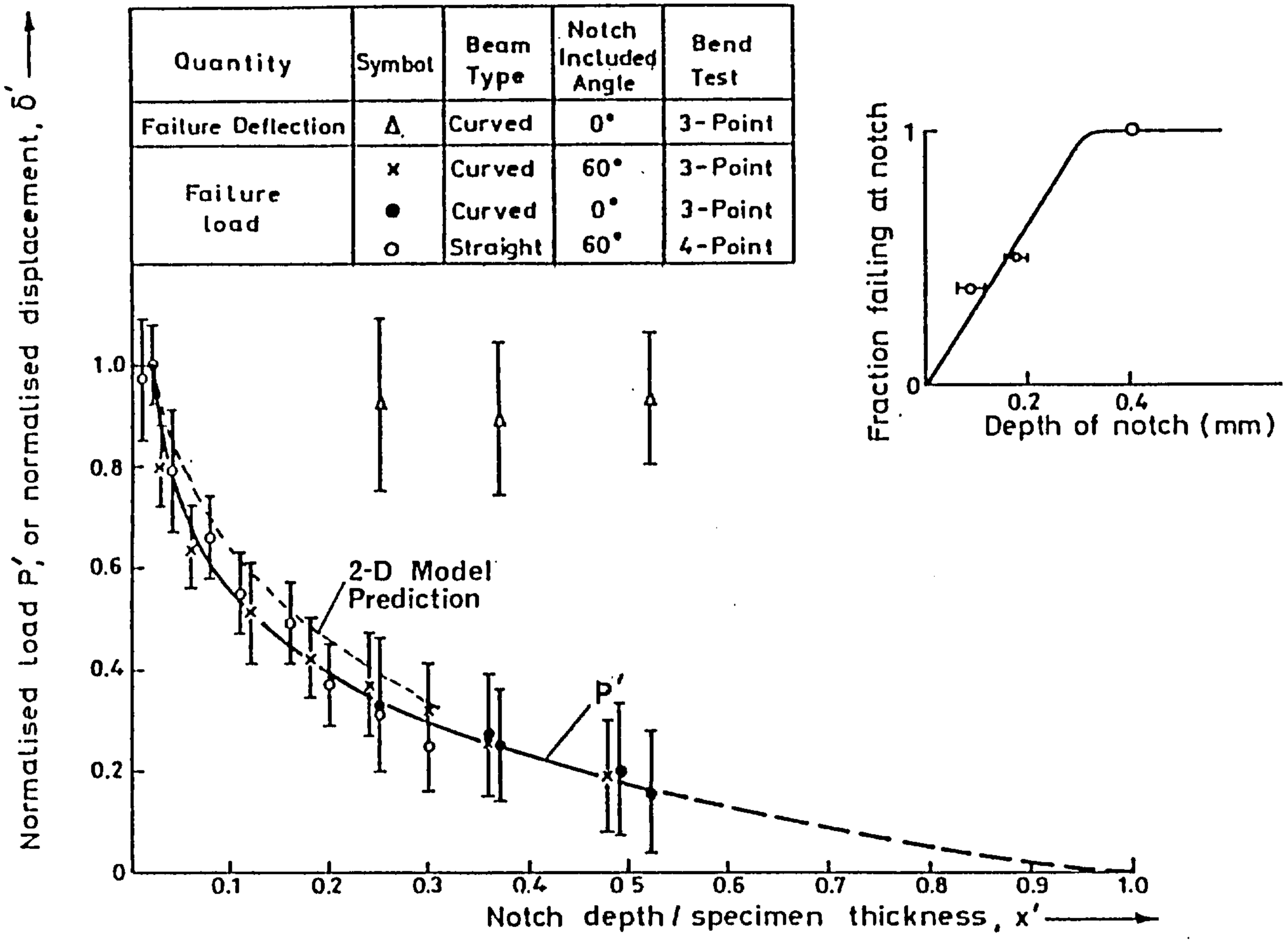

Figure 6.3: The variation of normalised failure loads and deflections with aspect ratio of notch (extrapolated beyond x' = 0.52).

where x' is the ratio of notch depth to specimen thickness. This simplified form may be readily used to evaluate G_{Ic}. If additional deflection measurements were available it would be possible to include a non-zero dimensionless term $d\delta'/dx'$ although the shallow slope suggested means that this would be small in comparison with the dP'/dx' term. Thus equation 6.3 has been used to calculate the critical crack extension force.

Consider further Figure 6.3. At x' values of 0.01 and 0.02 not all samples failed from the notch. The insert to the figure indicates that certain failure from the notch root occurs only for notch depths > 0.3 mm in a 10 mm thick bar. This value must be regarded as approximate as it is based on a limited number of results. However, it does give a measure of the largest cracks present within the material at fracture and indicates the dividing line between one of these cracks and the machined notch being the more severe defect. From approximately x' > 0.03 the specific loads P', fall off along a smooth curve. Error bars shown represent variations of ± one standard deviation in both P and P_o. Results from straight and curved beams containing notches of the same root radius tested in three- and four-point bend all lie on the same experimental curve and thus allow (dP'/dx'), required in equation 6.3, to be obtained. The agreement of the notched beam results with this single curve is very good. For x' > 0.52 the P' curve is extrapolated to zero failure load at a through thickness notch.

The failure deflection measurements corrected for the testing machine deflection, are also plotted in a dimensionless form on Figure 6.3. The error bars include ± one standard deviation in both δ and δ_o. Unlike the load results, as mentioned above the deflections remain constant at approximately 0.9 of the un-notched

value independent of notch aspect ratio. There is a slightly larger amount of scatter in the deflection measurements and no correlation between load and deflection at failure was found. It appears to be a reasonable assumption as outlined above that failure deflection is independent of notch depth within the range examined.

In using equation 6.3 to calculate G_{Ic}, account must be taken of the effect of root radius of the notch on the term (dP'/dx'). Brocklehurst (1974) has reported four-point bend tests on beams of fine grained Gilsocarbon graphite containing notches of different aspect ratios and root radii from ∿ 0.003 mm to 10.2 mm. These results are illustrated in Figure 6.4. Not all the standard deviations on failure loads are given in the source paper therefore these are omitted but appear from the original to be of the same order as those of Figure 6.3. Also shown on Figure 6.4 are the P' curve from Figure 6.3 and the expected decrease in normalised failure load for an un-notched beam as its thickness is reduced. This is obtained from the elastic bend stress formula such that P' is proportional to thickness squared assuming that failure occurs at a constant maximum ligament stress. The elastic line falls more gently than the P' curve over the range of aspect ratios examined indicating the greater stress intensification at a notch root compared with a flat beam of thickness reduced by the notch depth.

The finest root radii of ∿ 0.003 mm were obtained by tapping a coarser notch root with a razor blade. It is seen in Figure 6.4 that this produces little further stress intensification than the 0.5 mm root radii notches in the pitchcoke graphite. This is in agreement with observations made by Brocklehurst in that the material effectively blunts any sharper notches to a limiting value of root radius. Hence, it is correct to evaluate (dP'/dx) from the P' curve.

Key

Symbol	Root radius (mm)
×	0.003
o	0.1
□	0.6
Δ	2.5
∇	10.2

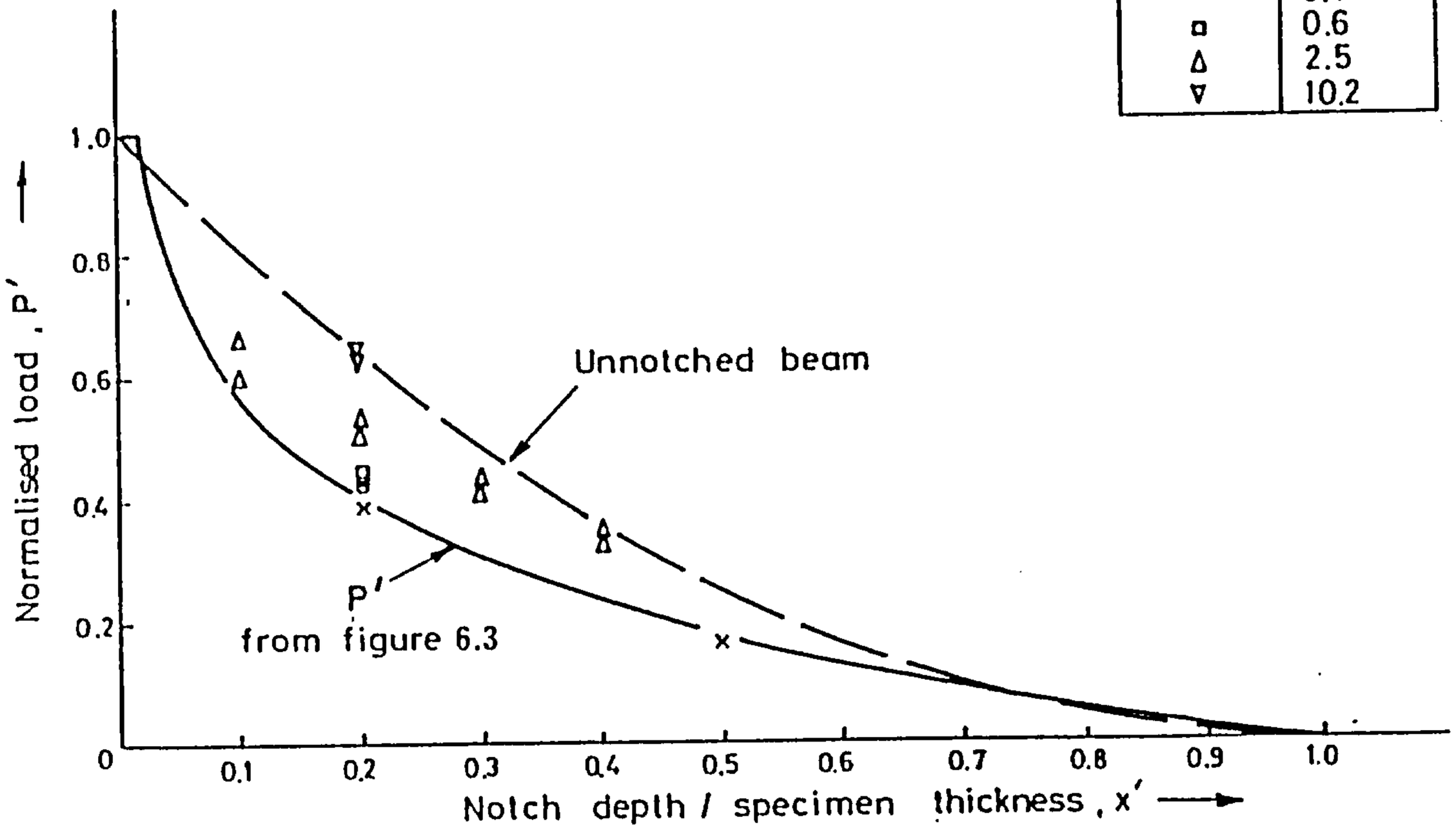

Figure 6.4: Brocklehurst (1974) data on the effect of notch root radius on failure loads of Gilsocarbon beams containing notches of various aspect ratios.

Considering the results at x' = 0.2, for which most data is available, the stress intensification is seen to reduce as the notch becomes blunter until at the largest radius of 10.2 mm the beam is equivalent to an un-notched elastic specimen of the same thickness as the ligament length below the notch root. Results for notches of other aspect ratios are also well enveloped by the P' curve at the 'sharp' extreme and the elastic curve for un-notched beams.

In order to justify the first assumption made in section 6.3.1 it is now necessary to evaluate the length a_1, of the additional crack below the notch root. The insert to Figure 6.3 seeks to do this by defining the minimum depth at which the artificial notch acts certainly as the fracture initiation site. This approach was first adopted by Brocklehurst and Kelly (1979). It assumes that the porosity distribution may be conveniently represented as a single through thickness crack for the purpose of K_{Ic} measurement, although this may be criticised in that the additional crack size found by Brocklehurst and Kelly is different in bend and tension and therefore is a function of stress distribution. However, as we are presently concerned simply with bend tests the idea is of considerable value. An additional crack size of 0.3 mm is indicated from Figure 6.3. This must be treated with some caution as its choice is mainly based on 6 tests on bars containing 0.4 mm notches. If more of these tests were done then a probability of failure from the notch of less than unity may well be obtained. Therefore, the value of 0.3 mm must be regarded as a lower limit estimate.

A second piece of evidence is available from image analysis studies. Using the technique explained in section 6.2, a polished surface parallel to extrusion, so containing the most probable fracture initiation sites,was examined. All pores having a maximum

chord length > 0.3 mm were analysed. The largest chord length obtained was 1.6 mm and the average was 0.5 ± 0.2 mm. This average cannot be regarded as absolute as it is a function of the lower limit cut off value. In addition, it was deduced from observation of similar large pores in surfaces perpendicular to extrusion that maximum chord lengths were typically near perpendicular to the crack growth direction such that these pores would be relatively ineffectual in acting as cracks. The image analysis of large pores is therefore inconclusive in defining a_1. Rather it is more likely that the additional crack consists of an agglomeration of much smaller pores along the notch root which coalese during the test by easy cleavage of well oriented particles thus acting as a single crack immediately prior to failure.

Equations 5.9 and 5.10 may be further utilised to study the additional crack length. Figure 6.5 shows how additions to the machined notch depth affect the value of K_{Ic} predicted from these equations. A figure of this type has been deduced by Birch et al. (1983) for a wide range of different graphites. The full line represents the case of an un-notched beam, the K_{Ic} value rising rapidly as the assumed additional crack size increases. A selection of the notched beam results are shown as broken lines on the figure. For these, the dependence of K_{Ic} on a_1 is reduced as the additional crack becomes a smaller proportion of the total crack length. The interesting feature of the figure is the approximate cross-over point of the notched and un-notched cases at which the K_{Ic} value from equations 5.9 and 5.10 is independent of machined notch depth. This occurs at $a_1 \approx 0.6$ mm. The independence of the calculated K_{Ic} value to notch depth indicates that notched or un-notched specimens may be used in fracture toughness testing by this method.

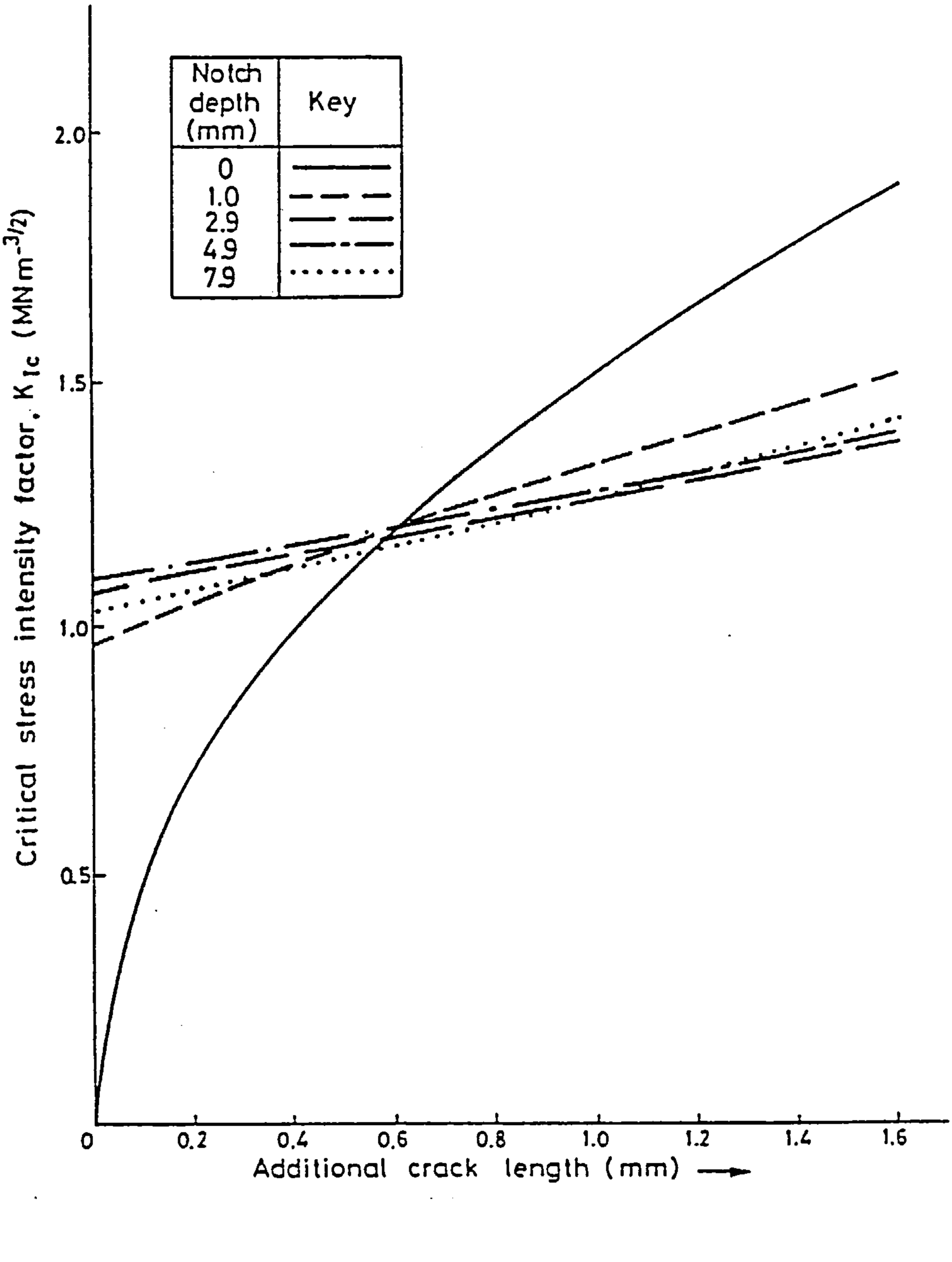

Figure 6.5: K_{Ic} values given by equations 5.9 and 5.10 as a function of the additional crack length added to the machined defect.

The second approach to calculating the critical stress intensity factor requires use of load and deflection measurements at failure to give the critical crack extension force per unit area of crack from equation 6.3. Results are shown in Figure 6.6 and it is seen that the K_{Ic} value is calculated to decrease as the notch depth increases. Physically, this means that the rate of energy release with crack extension is a function of the initial notch depth. There is support for this in the acoustic emission data summarised in Table 6.1. Noise detected prior to failure has been associated with microcracking and hence energy release in addition to that required to form the main failure crack (Pickup et al., 1981). For the 30 un-notched curved beams tested in three-point bending as in Figure 6.1, the onset of noise was detected at a load of 130 N ± 19 N. This is (15 ± 4)% the final failure load and indicates widespread secondary cracking during the test. With a specimen containing a notch, acoustic emission is detected at a lower load which tends to decrease as the notch deepens, although the results are widely scattered. When the fraction onset load/failure load is considered, it is evident that cracking starts later in the test as the notch length increases. If this trend is maintained for deeper notches then no cracking will be detected before failure and all the energy release with crack extension during the test will go towards creating the primary crack. To determine the point at which this occurs, and hence a lower limit fracture toughness value, requires tests on specimens containing notches of aspect ratio greater than 0.5. Equation 6.3 predicts that a lower limit G_{Ic} is obtained at the minimum value of dP'/dx'. This occurs as $x' \rightarrow 1$ that is as the notch depth approaches the specimen thickness. However, such tests are not easy to interpret due to the proximity of the surface towards which the growing crack propagates. Hence there

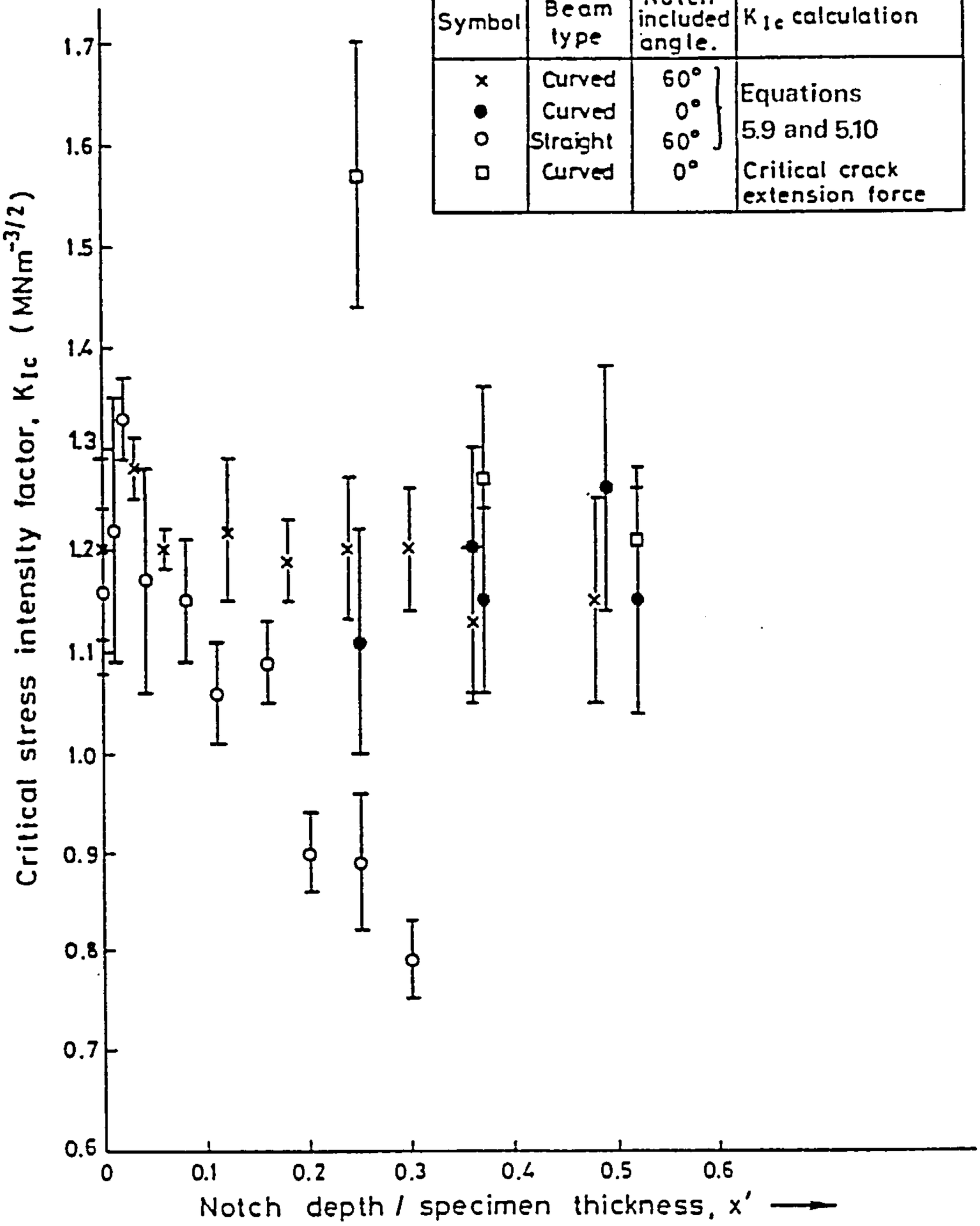

Figure 6.6: The variation of K_{Ic} calculated by different methods as a function of notch depth/specimen thickness ratio.

Table 6.1

Acoustic Emission Response of Notched Graphite Beams in Three-Point Bend

Aspect Ratio of Notch	Load at Onset of Acoustic Emission (N) ± 1 Standard Deviation	Fraction of Failure Load at Onset of Acoustic Emission ± 1 Standard Deviation
0	130 ± 19	0.15 ± 0.04
0.25	80 ± 12	0.25 ± 0.05
0.36	69 ± 19	0.31 ± 0.11
0.48	69 ± 32	0.42 ± 0.27

are considerable experimental difficulties in defining a test to measure a consistent value of critical stress intensity factor using the method of energy release with crack extension.

Figure 6.6 is a plot of critical stress intensity factor K_{Ic}, against notch aspect ratio for all small specimen data as calculated from the two methods described. Following from the discussion above, the values obtained from the critical crack extension force are seen to be a decreasing function of notch aspect ratio. Values calculated from equations 5.9 and 5.10, applied to the 10 mm thick straight beams are also seen to decrease sharply at $x' \geqq 0.2$. In these cases there is 8 mm or less thickness below the notch and the decrease in K_{Ic} is associated with a particle size effect as the reduced section is untypical of bulk behaviour. However, all the curved beams contain a thickness greater than 8 mm beneath the notch and therefore the calculated K_{Ic} values do not show any such decrease. The independence of K_{Ic} to notch depth is noted. The spread of results over ± one standard deviation is approximately 1.2 ± 0.15 MPa $m^{\frac{1}{2}}$, in good agreement with data from large components of pitchcoke graphite (Rose and Tucker, 1982). It appears that the choice of an additional crack length of 0.6 mm below the machined notch compensates well for the decrease in critical crack extension force with increasing notch depth throughout the range examined.

6.5 Application of Two-Dimensional Model

6.5.1 Stress distribution

In undefected beams the elastic stress distribution is given by equation 4.1 but this is not valid in the presence of a notch. To overcome this, finite element stress distributions have been determined for unit loads on notches 1, 2 and 3 mm deep and 0.5 mm root radius in a beam of depth 10 mm (Watson, 1984). The 1 mm case is given as an

example in Figure 6.7 together with the specimen and loading geometries. Using matrix methods these stress distributions are well represented by the general expression

$$\sigma(x) = -0.1\,x(x' + 1) + 0.1(x' + 7) + 0.22/x + 0.06/x^2$$

$$0.1 \leqslant x' \leqslant 0.3, \qquad (6.4)$$

$\sigma(x)$ being measured in Pascals and x in millimetres. This equation is unsuitable at small x as $\sigma(x) \to \infty$ as $x \to 0$. However, the peak stress at the notch tip (x = 0) is known from the finite element analysis and may be represented by the equation

$$\sigma(0) = 26x' + 4.7 \qquad 0.1 \leqslant x' \leqslant 0.3. \qquad (6.5)$$

Equations 6.4 and 6.5 may be solved graphically to give x_o, the value of x at which $\sigma(x) = \sigma(0)$, which is found to vary with x' according to the expression

$$x_o = -0.16x' + 0.13 \qquad 0.1 \leqslant x' \leqslant 0.3. \qquad (6.6)$$

Thus it is appropriate to regard the stress to be given by equation 6.5 for $x < x_o$ and by equation 6.4 for $x > x_o$. The exact stress distribution ahead of the notch is insensitive to small variations in knife edge spacing and specimen dimensions. Therefore it is assumed that these two equations apply to all notched bend tests for which x' is in the range 0.1 to 0.3.

Use of equations 6.4 and 6.5 in the fracture model presents a difficulty. The very high peak stress at the notch root means that the critical crack size obtained from equations 5.9 and 5.10 becomes less than one particle diameter even at a low applied stress. This results in a much lower predicted strength than that observed. In an analogous manner, elastic theory over-estimates the notch sensitivity of the material, an effect which has been noted by other investigators (Corum, 1967; Brocklehurst, 1974).

Brocklehurst defines the average stress concentration factor

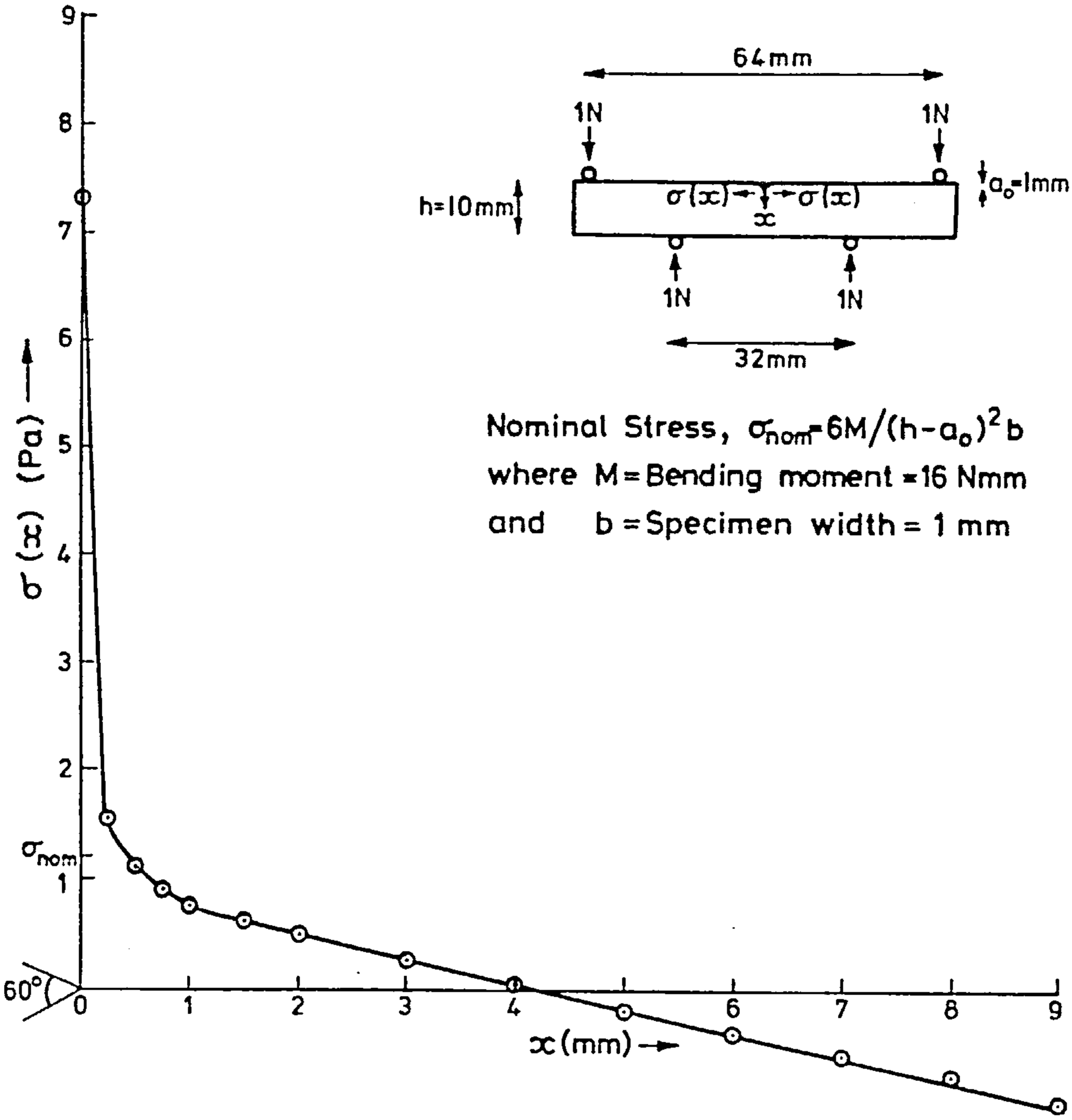

Nominal Stress, $\sigma_{nom} = 6M/(h-a_o)^2 b$

where M = Bending moment = 16 Nmm

and b = Specimen width = 1 mm

Figure 6.7: Crack opening stress obtained from finite element analysis of a notch of depth 1 mm and root radius 0.5 mm in bending. The beam is 10 mm deep and of unit width.

(SCF) in the ligament depth below the root of a notch in bending as

$$SCF = \sigma_b/\sigma_{nom} . \qquad (6.7)$$

where σ_b is the elastic bend strength of an un-notched beam and σ_{nom} is the nominal stress at the notch root as defined in Figure 6.7, the bending moment being obtained from the load at failure. If an un-notched beam of depth h fails at load P_o and a beam of the same geometry but containing a notch of depth a_o fails at load P then

$$\sigma_b \propto P_o/h^2 \quad \text{and} \quad \sigma_{nom} \propto P/(h - a_o)^2$$

giving

$$SCF = P_o(h - a_o)^2/Ph^2. \qquad (6.8)$$

In tests on isotropic Gilsocarbon graphite Brocklehurst found that SCFs as defined by equation 6.8 were always less than two. A <u>local</u> notch root stress concentration (defined as $\sigma(0)/\sigma_{nom}$) of 6.2 is predicted from Figure 6.7 for a notch of $x' = 0.1$ and although this is not strictly comparable with the average SCF obtained from equation 6.8 it is reasonable to assume that the peak stress at the notch root is redistributed over a short distance either by pores or cleaved particles intersecting the notch or by local plastic flow. Figure 6.8 shows an example at $x' = 0.3$ of the assumed form of redistribution of $\sigma(x)$. The 'flow stress' is taken to be the SCF multiplied by σ_{nom} and the elastic stress at $x < x_1$ is transferred to an area under the curve in the region $x_1 < x < x_2$ such that the elastic strain energy remains constant. Hence it is assumed that the stress ahead of the notch is uniform in the region $x < x_2$, falls discontinuously to the elastic stress distribution at $x = x_2$ and then follows this distribution for $x > x_2$. In practice the discontinuity is obviously unrealistic but smoothing the stress distribution whilst maintaining the elastic strain energy constant does not significantly

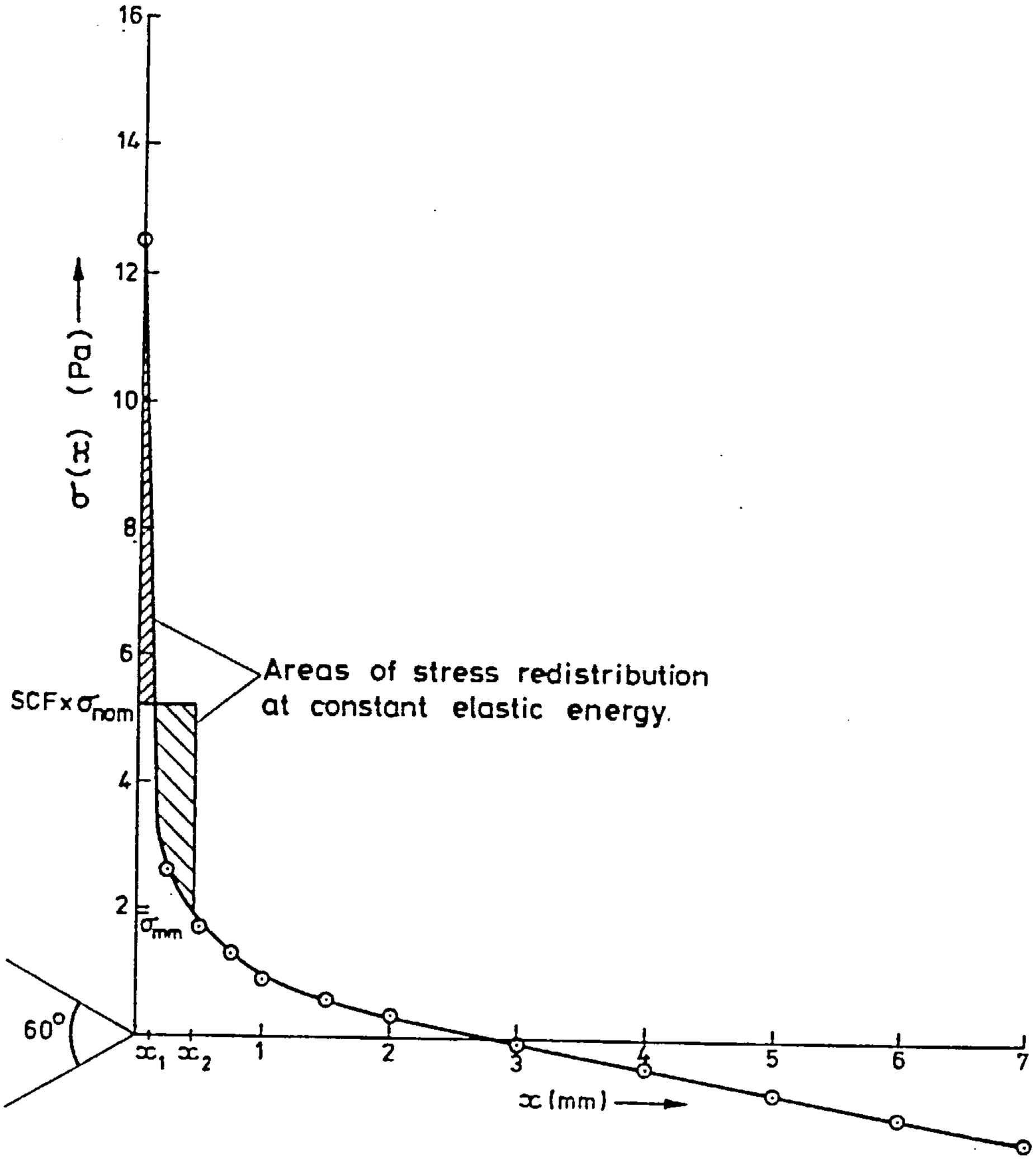

Figure 6.8: Crack opening stress obtained from finite element analysis of a notch of depth 3 mm and root radius 0.5 mm in bending. The assumed form of stress redistribution ahead of the notch used in the fracture model is shown.

affect the failure probability predictions. This is because the reduced volume at maximum stress is balanced by the increased amount of material in the region $x > x_2$ where the stress is increased.

It remains to calculate average stress concentration factors from the data of Figure 6.3. Values are shown as a function of x' in Figure 6.9. At $x' < 0.03$ the notch has no effect on the fracture load and failure does not always occur from the notch. Therefore equation 6.8 does not apply. In the region $0.03 < x' < 0.25$ SCFs rise from unity to a maximum of 1.76 ± 0.12. Error bars shown represent ± one standard deviation in P but assume a single value of P_o. For increasing x' in the region $0.25 < x' < 0.52$ the SCF drops approximately linearly due to the competing effects in equation 6.8 of the decreases in P and $(h - a_o)^2$. Although there is considerable scatter in SCFs for pitchcoke graphite, the overall trends are clear. Further data from IM1-24 beams containing notches of root radius ~ 0.003 mm (Brocklehurst, 1974) which confirms the pitchcoke results is also shown on Figure 6.9. Results from tests performed by Corum (1967) on beams of coarser AGOT graphite (specification given in Table 3.2) cut perpendicular to the extrusion direction show lower SCFs although the same trend with x' is observed. Hence, SCFs are a function of the material texture, the sensitivity to notches decreasing as the particle size increases.

It is found that the observed SCFs in pitchcoke graphite follow the equations

$$\begin{aligned} SCF &= 1.00 && x' < 0.03 \\ &= -17.50(x'-0.03)^2 + 6.95(x'-0.03) + 1.00 && 0.03 \leqslant x' \leqslant 0.25 \\ &= -0.96x' + 1.91 && 0.25 \leqslant x' \leqslant 0.52. \end{aligned} \qquad (6.9)$$

Care is required in the use of the lowest limit on x' in that for

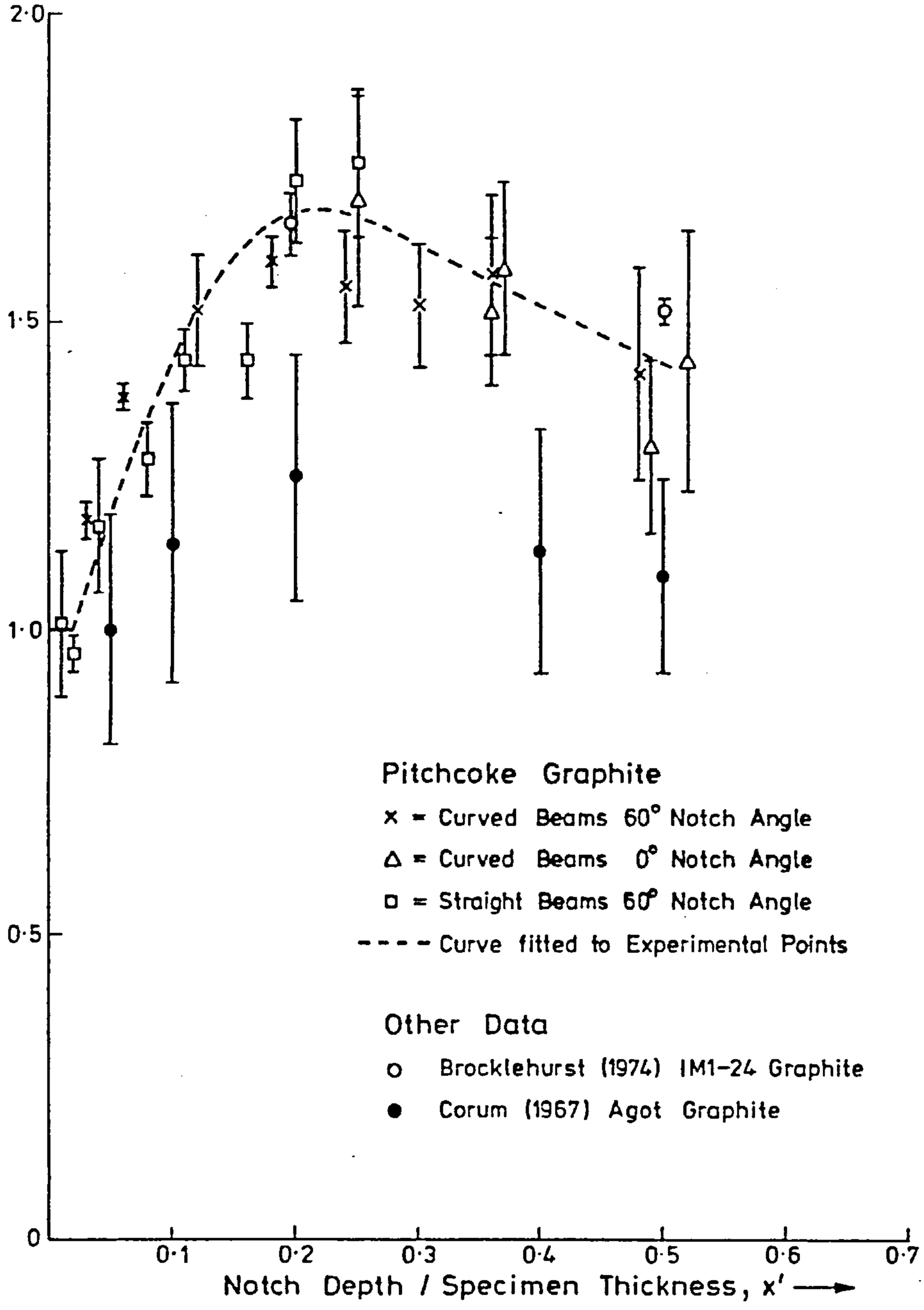

Figure 6.9: Experimental stress concentration factors ahead of 'sharp' notches for a range of graphites as a function of notch aspect ratio.

beams of large depth there may be a stress concentration at $x' < 0.03$. However, with the range of specimen sizes examined this reservation does not apply.

To summarise, for $x < x_2$ the stress ahead of the notch $\sigma(x)$ is uniform and equal to σ_{nom} multiplied by the SCF from equation 6.9. For $x > x_2$, $\sigma(x)$ is given by equation 6.4 or 6.5 which are valid in the range $0.1 \leqslant x' \leqslant 0.3$.

6.5.2 Number of initiation sites

It is reasonable to assume that fracture initiation from the notch may only occur in those particles immediately below the notch root at a stress greater than the particle cleavage stress. Thus, the number of initiation sites is $mb/2A$, where m is defined in equation 5.7. It is desired that the model be continuous in its application from notched to un-notched specimens. Therefore the probability P_b of fracture occurring in the bulk must be considered, the number of initiation sites in this case being given by equation 5.8 minus the $mb/2A$ sites already counted. Hence if P_n is the probability of failure from the notch, the overall failure probability P_F is

$$P_F = 1 - (1 - P_n)(1 - P_b). \qquad (6.10)$$

For small notches both P_n and P_b contribute to P_F however as the notch depth increases $P_b \to 0$.

Apart from this modification to the number of initiation sites and the single particle size, the failure statistics are exactly as in section 4.3.

6.5.3 Choice of critical crack size

Equations 5.9 and 5.10 with σ equal to σ_{nom} multiplied by the SCF are used to determine the critical crack radius. Use of this value is consistent with the stress distribution ahead of the notch deduced in section 6.5.1 and satisfies the relevant condition 5.11

for all the tests performed. The critical crack extends from the notch root to a radius c into the specimen but for simplicity the stress is taken to be a function of x only, that is the variation of stress around the surface of the notch is not considered.

6.5.4 Comparison of theory and experiment

The two-dimensional model prediction of normalised failure load P' as a function of notch aspect ratio x' is included on Figure 6.3. The shape of the experimental curve is followed well although the mean strength is slightly over-predicted at all values of $x' > 0.03$. Strictly, the notch failure model is applicable only to the range $0.1 \leqslant x' \leqslant 0.3$ for which the expressions 6.4 and 6.5 have been validated against finite element stress distributions. However, at lower x' the agreement with the P' curve is very good, the model predictions being continuous from fracture in an un-notched beam through fracture from very small notches ($x' < 0.03$) to fracture from deep notches. The reason for good agreement at $x' < 0.1$ is the dominating effect of the maximum stress (σ_{nom}.SCF) considered. This is the uniform stress immediately ahead of the notch and influences the choice of critical crack radius. Thus it is the controlling parameter in the model and as it is based on experimental determination of the SCF a good representation of the observed mean strengths in the wider range $0 \leqslant x' \leqslant 0.3$ is obtained. Similarly, although not shown on Figure 6.3, the model prediction is close to experiment for $0.3 < x' \lesssim 0.5$. At $x' \gtrsim 0.5$, for the value of σ_{nom} at failure the stress ahead of the notch $\sigma(x)$ used in the model decreases to a value below the particle cleavage stress within the critical crack radius due to the proximity of the surface opposite the notch. For failure to be predicted therefore a much larger σ_{nom} than observed must be applied. This restriction is eased for deeper specimens but there

is always an upper limit on x' at which the model breaks down. However, few components are designed with sharp notches having x' > 0.5 such that this limitation is not prohibitive.

This analysis is based on an assumed stress distribution, however it has been developed in conjunction with experimental observation of fracture from a notch. The most striking omission is the effect of crack interaction. Effectively the configuration of the critical defect is decided in the model before any sub-critical cracking occurs. On particle cleavage, particularly ahead of a stress concentrator, the probability of cleavage of neighbouring particles is considerably enhanced. This is a major weakening mechanism and its neglect causes the overprediction of material strength in the presence of a notch. However, the consistent description of fracture in bending in the range $0 \leqslant x' \leqslant 0.5$ is a notable achievement.

The earlier sections of this chapter demonstrated for pitchcoke graphite that an additional crack of length 0.6 mm must form before failure in a bend test can occur. Knowing this, it is possible to use the converse of the method of section 5.3 to predict σ_{nom} and hence the P' curve of Figure 6.3. This LEFM approach is capable of predicting mean failure stresses of sound or notched beams in bend but would require a larger value of additional crack size to predict mean failure stresses in tension (Brocklehurst, 1974). In contrast, the two-dimensional model needs no alteration of input data to predict tensile failure in un-notched specimens. More experiments to determine fracture stresses of notched beams in tension are required to enable further comparison with theory, as the method of section 6.5 may be readily developed to cover tensile failure.

6.6 Conclusions

From the work presented in this chapter the following conclusions

may be drawn.

(i) K_{Ic} may be determined for a given graphite from bend tests on notched or un-notched beams of depth greater than approximately ten particle diameters subject to a knowledge of the effective additional crack size in bending.

(ii) The two-dimensional model of fracture may be used to predict failure from a sharp notch in bending.

(iii) The model slightly over-estimates such failure stresses due to the simplifying assumption that there is no interaction between sub-critical cleavage cracks and neighbouring particles.

(iv) Experiments on notched tensile specimens are necessary to test the model further.

CHAPTER 7

EFFECT OF IRRADIATION ON STRENGTH AND MODULUS

7.1 Mechanisms of Irradiation Damage

7.1.1 Within crystal changes

The effectiveness of graphite as a moderator material relies on its ability to retard energetic neutrons. This process involves elastic collisions between nuclei and carbon atoms causing up to 1000 atomic displacements per incident fast neutron such that damage may be assumed to be uniformly distributed. Low dose irradiations show the effects of these displacement cascades without the complication of changes in the macrostructure. The types of lattice defect produced have been discussed in detail by Kelly (1978, 1981) and Brocklehurst et al. (1981). Initially, sub-microscopic groups of mobile interstitials and immobile vacancies are formed. These reach an equilibrium concentration which is lower, the greater the irradiation temperature and is essentially zero above $\sim 300^{o}C$. The next stage is the formation of interstitial and vacancy loops. The single crystal elastic stiffness constant C_{44}, controlled by inter-layer forces, increases by a factor up to 16, although C_{33} is unaffected due to the ease of out of plane bending. As a result, below $300^{o}C$ Young's modulus increases to a peak of 2.5 times the virgin value. Above $300^{o}C$ the magnitude of the increase is smaller (Kelly, 1981) as there are no isolated vacancy/interstitial pairs. Jenkins (1973) considers that the dramatic increase in C_{44} is due to covalent bonding between interstitial groups and the basal planes, but in evaluating all the evidence Kelly (1981) concludes that pinning of basal plane dislocations by the irradiation induced defects is the dominant process.

The carbon atom displacements outlined above cause an overall

volume shrinkage at a decreasing rate even though individual crystals change shape at constant volume by a-axis shrinkage and c-axis growth. The net shrinkage occurs because the c-axis growth is accommodated by the filling in of pores in the c-direction, mostly generated on cooling after graphitisation. During this pore closure Young's modulus increases but more gradually than the initial rise. Strength also increases, as discussed in more detail below, by up to the same fractional amount as the modulus.

The variation of thermal expansion coefficient with irradiation must be determined from experiment for individual graphites at required temperatures but virgin values can be used to predict the initial dimensional stability of a new graphite (Kelly, 1981). Thermal conductivity tends to decrease on irradiation. This is explained by a simple model of lattice defects increasing the thermal resistance (Kelly, 1981).

7.1.2 Bulk changes

At higher doses, as pores in the c-direction become filled, the shrinkage rate decreases and a reversal to growth occurs. Reversal is seen earlier, the higher the irradiation temperature. Dose units are conventionally expressed in neutrons per square centimetre DIDO Nickel Equivalent (DNE), that is the experimental equivalent damage dose in a standard position in the DIDO test reactor defined by the nickel-activation reaction ^{58}Ni (n/p) ^{58}Co. For example, in PGA graphite perpendicular to extrusion a net zero dimensional change is obtained at approximately 1.9×10^{22} n/cm^2 DNE for irradiations between 300 - 350^{o}C and at $\sim 1.2 \times 10^{22}$ n/cm^2 DNE at a temperature between 600 - 700^{o}C (Kelly, 1978). The United Kingdom Magnox reactors use PGA graphite as a moderator and operate at a maximum core temperature of approximately 350^{o}C to an end of life dose of approximately

5×10^{21} n/cm^2 DNE. Hence the core is in net shrinkage for its entire life. The more recent CAGR reactors are designed to run at much higher temperatures (maximum core temperature approximately 550°C) and to higher fluences ($\sim 2.5 \times 10^{22}$ n/cm^2 DNE) such that the dimensional stability of PGA graphite is unacceptable. The requirement is for an isotropic graphite of high initial thermal expansion coefficient ($\sim 5 \times 10^{-6}$/°C) and hence low initial shrinkage rate. In addition, a delayed progression to the expansion phase must be established by accelerated irradiation experiments in a test reactor. A Gilsocarbon graphite which at 650°C shrinks to a maximum of 2-3% at a neutron dose of $\sim 1 \times 10^{22}$ n/cm^2 DNE and shows approximately zero net dimensional change at end of reactor life was developed to meet the required specification for the CAGR core (Kelly, 1978; Carpenter and Norfolk, 1984).

Growth is associated with intercrystalline reactions resulting in the generation of large scale porosity which jacks the c-axis apart. The determining factors in the process are not quantitatively understood but key parameters are crystal strain and/or strain rate together with density and degree of anisotropy (Brocklehurst et al., 1983). During growth Young's modulus, strength and thermal conductivity all decrease such that finally the material disintegrates. It is important to note that shrinkage and growth are the result of two distinct processes occuring consecutively. Hence the mechanism of growth is not the reverse of shrinkage.

7.2 Strength and Modulus Changes

7.2.1 Mean Values

Brocklehurst (1974) has shown that for the entire period of irradiation before material breakdown, tensile or bend strength changes $\Delta\sigma$, lie between limits of proportionality to modulus changes

of $\propto \Delta E^{\frac{1}{2}}$, failure at constant elastic strain energy and $\propto \Delta E$, failure at constant elastic strain. Irradiation data from available literature sources is listed in Table 7.1. This may be summarised in that high temperatures (> 1000°C, with consequent early turnaround to growth) favour $\Delta\sigma \propto \Delta E$, intermediate temperatures show $\Delta\sigma \propto \Delta E^{\frac{1}{2}}$ and low temperatures may exhibit either relation dependent on the graphite grade.

Several of these literature sources argue, on the basis of the Griffith relation (equation 2.4), that at low doses a $\Delta\sigma \propto \Delta E^{\frac{1}{2}}$ relationship is expected. This assumes that there is no change in the critical crack size or the effective surface energy but there is no data available to validate these assumptions. Again, as mentioned in Chapter 2, care must be taken to distinguish between the maximum pore size and the critical crack size. At higher doses, after turnaround in dimensional changes, large pores are generated and bulk density decreases. In a converse analogy to this, studies involving successive impregnations of reactor graphite (Losty and Orchard, 1962) have shown that bend strength increases proportionally to modulus ($\Delta\sigma \propto \Delta E$) with failure occurring at constant strain. This is consistent with a model of failure at constant strain energy within individual crystals and the impregnant acting as an additional load bearing material in parallel. Irradiation growth may be envisaged as a reverse impregnation process such that a $\Delta\sigma \propto \Delta E$ relationship might be expected. In short, for any new graphite the proportionality between strength and modulus changes must be determined, in advance of reactor operation, by irradiation experiments in a high neutron flux test reactor. The expected performance must then be monitored from the start of reactor life by testing samples at specified neutron dose intervals.

Table 7.1

The Effect of Irradiation on Strength and Young's Modulus of Various Graphites

REFERENCE	GRAPHITE GRADE	TEMPERATURE (^{o}C)	CHANGE IN STRENGTH PROPORTIONAL TO CHANGE IN	MAXIMUM DOSE (n/cm^2 DNE)
Sato and Miyazono (1964)		30 and 80	E	7×10^{20}
Birch and Bacon (1983)	Gilsocarbon	50	E	1.14×10^{19}
Losty and Orchard (1962)	'Reactor'	60	$\sqrt{E}$	1×10^{19}
Taylor et al. (1967)	'Isotropic'	150	E	1.15×10^{21}
Taylor et al. (1967)	'Anisotropic'	150	$\sqrt{E}$	1.15×10^{21}
Platonov et al. (1973)	'Reactor'	100	E	$5\text{-}8 \times 10^{21}$
Platonov et al. (1973)	'Reactor'	570	$\sqrt{E}$	$5\text{-}8 \times 10^{21}$
Matthews (1974)	AXF-5Q	400	$\sqrt{E}$	3×10^{21}
Engle et al. (1974)	H-451	600	$\sqrt{E}$	6×10^{21}
Engle et al. (1974)	H-451	1300	E	6×10^{21}
Eto (1975), Eto and Oku (1975)	Needlecoke	820 - 920	E	9.8×10^{20}
Eto (1975), Eto and Oku (1975)	Gilsocarbon	820 - 920	E	9.8×10^{20}
Eto (1975), Eto and Oku (1975)	Fine Grain Isotropic	820 - 920	E	9.8×10^{20}
Brocklehurst (1974)	IM1-24	900	$\sqrt{E}$	2.5×10^{21}
Everett and Ridealgh (1972)	Gilsocarbon	900 - 1200	E	3×10^{21}

7.2.2 Distribution of strengths

Matthews (1974) and Lungagnani and Krefeld (1972) suggest that although the mean strength on irradiation in the region of shrinkage is always higher than the virgin value, Weibull statistical analysis indicates a greater failure risk at the 1 in 10^6 level, thereby implying an increase in heterogeneity of the microstructure. There are obvious difficulties in extrapolation of limited data which throw doubt on this conclusion. In a series of tests on a total of 50 samples of IM1-24 graphite Brocklehurst (1974) found that the overall effect is to shift the bend strength distribution to higher values whilst maintaining the same shape. Hence, there is no evidence for greater scatter in strength prior to large scale pore generation.

7.3 Experimental

As part of this project measurements were made of three-point bend strength and dynamic Young's modulus of pitchcoke bars machined from components irradiated to fast neutron doses in the range $0.40 - 1.84 \times 10^{21}$ n/cm^2 DNE under CAGR conditions (temperature $\sim 400^{\circ}$C, atmosphere mainly CO_2). Two competing processes occur in the samples within this dose range. Fast neutron damage, described earlier in this chapter, tends to increase strength and Young's modulus, and radiolytic oxidation, caused by reaction of the graphite with an activated species of CO_2 to form CO (Wood and Wickham, 1980), tends to decrease both quantities. In order to separate these effects half the samples in each batch were annealed to remove the radiation damage component whilst leaving the radiolytic oxidation unchanged. Brocklehurst et al. (1970) have suggested from Young's modulus and thermal conductivity measurements on PGA and isotropic graphites that for design purposes the combined effect of radiation damage and radiolytic oxidation may be written in terms of the separate changes as

Combined effect = (effect of neutron irradiation) x

(effect of radiolytic oxidation). (7.1)

Thus the separate changes on the right hand side of the equation are independent of each other. This equation could break down at high doses if removal of material by oxidation interacts with irradiation-induced changes, for example by creating more porosity capable of absorbing c-axis expansion, but in the dose range examined such interactions are not significant.

Simulations of the effects of radiolytic oxidation alone on strength have been reported in the literature by 'profiling' specimens (Metcalfe, 1982), and on strength and Young's modulus by drilling small holes (Adam and Brocklehurst, 1983) to represent particular weight losses and oxidation gradients.

7.3.1 Specimen details

Cutting specimens from irradiated components must be done remotely in a shielded facility. Ease of machining is therefore an overriding priority. As the component here is a hollow cylinder, the easiest specimen to produce is a full thickness 'finger', which is a curved beam of dimensions as in Figure 6.1 (a) but without a notch. This has advantages over the more conventional straight beam in that the component inner wall itself acts as the tensile surface in subsequent bend tests such that the test is the nearest possible to reactor conditions, and fracture occurs in a mode of technological interest. Also a thicker, and hence more representative, section than any straight beam machined from the component is under test. The disadvantage is that there is no standard method for dynamic modulus testing of curved bars but a technique has been developed as described below in section 7.3.3.

7.3.2 Three-point bend tests

The test geometry is detailed in Figure 6.1 (a). As mentioned in Chapter 6, from standard elastic theory the outer ligament tensile stress in a beam of this curvature is 5% greater than a straight beam of equivalent section under identical loading. Therefore the three-point bend fracture stress σ is given by

$$\sigma = 1.05 \quad 6M/h^2b \qquad (7.2)$$

where M is the bending moment at failure and h and b are as defined in Figure 6.1 (a).

7.3.3 Dynamic Young's modulus tests

The dynamic Young's modulus is determined from measurement of the fundamental resonant frequency, which is a function of specimen dimensions and material properties. In the flexural mode, the specimen is placed on supports which are located at the fundamental transverse nodal points (0.224 of the specimen length from each end) as in Figure 7.1 and a sprung plunger is dropped onto its top surface. The resulting fundamental frequency of vibration f, is picked up by a standard audio magnetic cartridge, stored in a transient amplifier and a permanent record made on a chart recorder. For a straight beam of rectangular cross-section, the dynamic modulus E, is given by (ASTM, 1974)

$$E = A_R \, mf^2/b \qquad (7.3)$$

where A_R is a dimensionless constant depending on the specimen geometry and Poisson's ratio, m is the sample mass and b is the specimen width. Values of A_R are tabulated by ASTM as a function of the ratio beam depth h, to specimen length L. They are fairly insensitive to Poisson's ratio and in the tabulation a value of 1/6 is used which is appropriate to most graphites.

For a curved beam there is an uncertainty in the resonating length

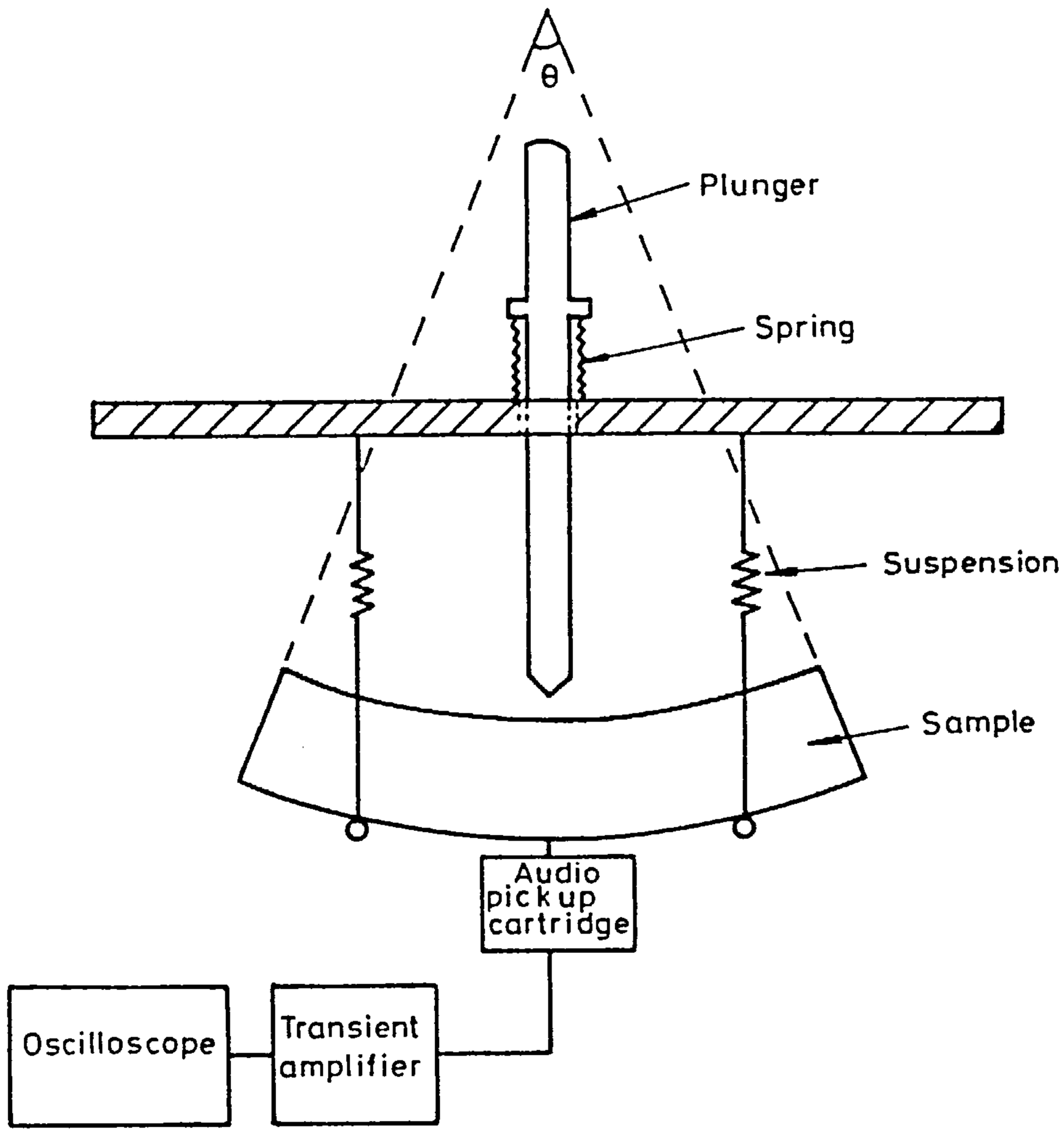

Figure 7.1: A schematic diagram of apparatus used for dynamic modulus determination.

and hence A_R. In order to accommodate this a series of experiments were carried out on perspex. Firstly, two rectangular bars were cut from a perspex sheet and the resonant frequency in the flexural mode determined. The dynamic modulus was calculated from equation 7.3 and ASTM tables as 5.14 ± 0.03 GPa. Next, a specimen of identical width and radius of curvature to the pitchcoke segments was cut from the same perspex sheet. The initial maximum chord length was 119.3 mm and this was progressively decreased to 78.0 mm by machining off approximately 4-5 mm after each resonant frequency determination. It is assumed that an expression of the form of equation 7.3 but with a different geometrical constant, A_R^*, applies to the curved bar samples. Figure 7.2 shows a plot of A_R^* against maximum chord length. The error bars represent an estimated worst uncertainty of ± 6% in the experimental determination of A_R^*, arising principally from error in frequency measurement. Also shown for comparison on the figure are values of A_R from ASTM tables for a straight bar of the same depth h, and length equal to the maximum chord length of the curved beam. It is seen that the two curves are of similar form and in fact if the resonating length of the curved bars is taken to be slightly less than the maximum chord length they coincide. Hence the dynamic modulus is obtained from equation 7.3 with A_R replaced by A_R^*, the value of A_R^* being read from Figure 7.2. As an additional check, dynamic moduli calculated from curved and straight beams of virgin pitchcoke graphite cut from the same component were found to be indistinguishable using this method.

7.3.4 Thermal annealing

Annealing is carried out to remove the effects of fast neutron hardening on dynamic modulus. An optimum annealing temperature exists for each graphite at each irradiation temperature and an experiment

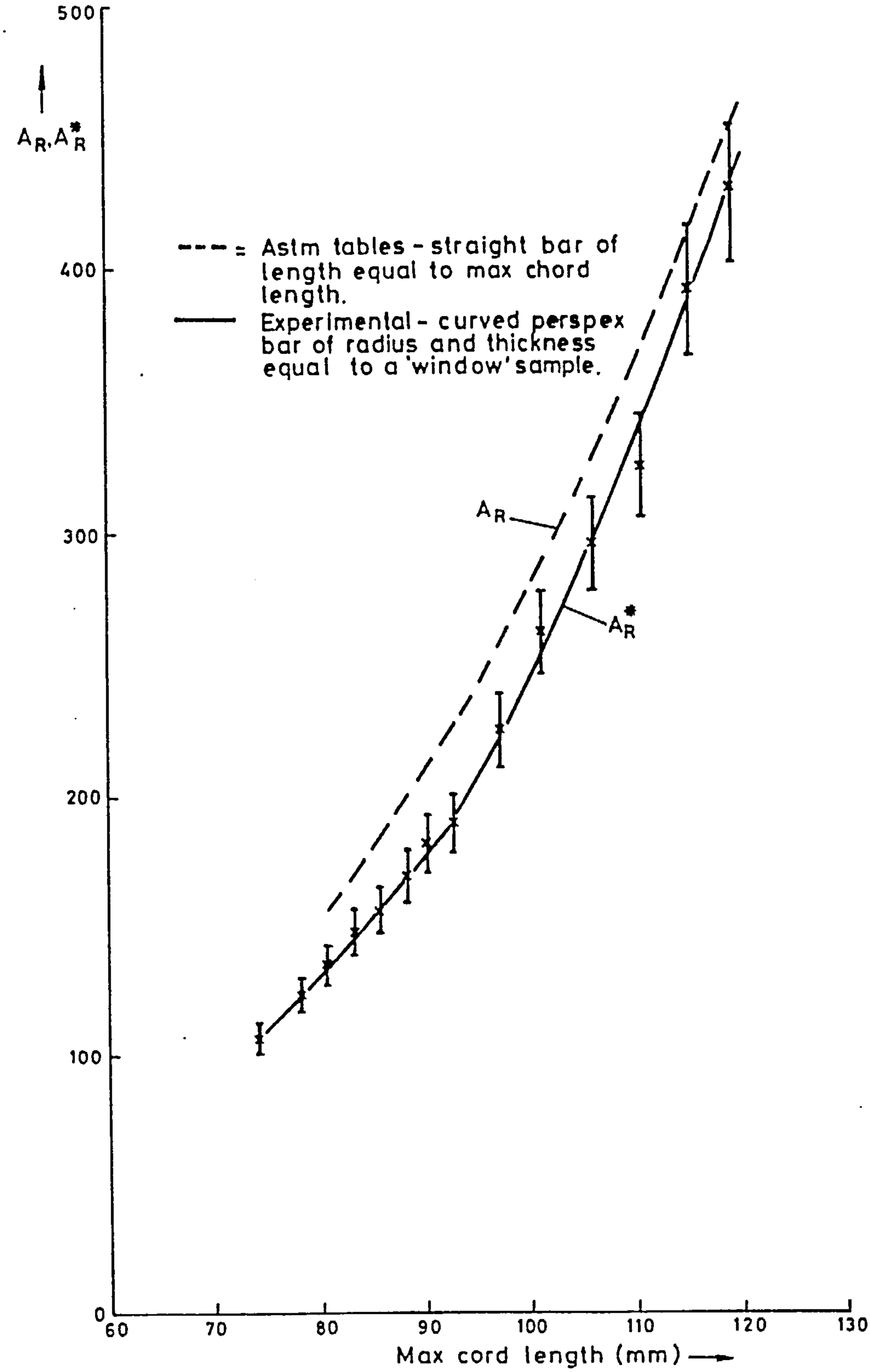

Figure 7.2: The variation of dimensionless constants A_R and A_R^* with maximum chord length of a pitchcoke specimen.

was performed to determine this for pitchcoke samples. Below this annealing temperature strength and modulus remain higher than in virgin material. Above it, values fall below those prior to irradiation and a permanent length change is observed due to structural changes in the material. Brocklehurst et al. (1970) have pointed out that not all damage is removed on full annealing but some remains although it is redistributed such that strength and modulus fall to virgin values.

From previous experiments (Brocklehurst et al., 1970) the optimum annealing temperature lies in the range 1900 - 2500°C. Five sets of six specimens were cut from the same component (coded 3U23/4 as in Table 7.2), which had been irradiated to 1.60×10^{21} n/cm^2. Dynamic moduli were determined for each specimen and for each set a mean value within ± 0.3 GPa of 14.8 GPa was obtained. Annealing experiments were then carried out in a graphite resistance furnace, one set at a time, with one hour at temperatures of 1900°C, 2100°C, 2300°C and 2500°C respectively. The final set was not annealed but used to determine the as-received three-point bend strength. Temperature measurement was achieved with an optical pyrometer accurate to ± 10°C. After annealing, tests were performed on several specimens to determine if pitchcoke graphite was subject to boron pick-up from the lower specification furnace graphite (Smith, 1982). This would adversely affect strength and modulus. However, no difference in boron content between virgin and annealed samples was obtained.

Figure 7.3 shows the measured dynamic moduli of the annealed specimens ± one standard deviation. The expected range of fully annealed values, 8.2 ± 0.2 GPa, shown on the figure is based on average virgin properties, the predicted weight loss due to radiolytic oxidation (Prince and Rossiter, 1982) and the predicted fractional decrease in modulus with weight loss (Birch et al., 1982). The

Table 7.2

As-Received and Annealed Strength and Modulus Data

COMPONENT CODE	FAST NEUTRON DOSE (DNE) $\times 10^{21}$ n/cm^2	AS-RECEIVED		ANNEALED		σ/σ_{ox}	E/E_{ox}
		MEAN FAILURE STRESS, σ (MPa)	MEAN DYNAMIC MODULUS, E (GPa)	MEAN FAILURE STRESS, σ_{ox} (MPa)	MEAN DYNAMIC MODULUS, E_{ox} (GPa)		
B4058/1	0.56	46.6 ± 1.9	15.4 ± 0.4	35.3 ± 4.2	8.8 ± 0.1	1.32 ± 0.17	1.75 ± 0.05
/2	0.80	41.9 ± 3.2	16.4 ± 0.3	35.8 ± 12.6	9.2 ± 0.3	1.17 ± 0.42	1.78 ± 0.07
/3	0.91	52.1 ± 3.7	17.8 ± 0.5	35.3 ± 8.5	10.6 ± 0.2	1.48 ± 0.37	1.68 ± 0.05
/4	0.91	37.6 ± 2.1	15.6 ± 0.5	40.8 ± 5.8	9.3 ± 0.4	0.92 ± 0.14	1.68 ± 0.08
/5	0.86	51.0 ± 1.8	17.0 ± 0.4	26.7 ± 1.0	10.4 ± 0.4	1.91 ± 0.10	1.63 ± 0.07
/6	0.78	41.4 ± 0.9	16.0 ± 0.5	26.1 ± 1.6	10.1 ± 0.3	1.59 ± 0.11	1.58 ± 0.06
/7	0.74	37.3 ± 2.6	14.8 ± 0.5	21.4 ± 1.2	9.2 ± 0.2	1.74 ± 0.16	1.61 ± 0.06
/8	0.40	36.8 ± 3.7	16.9 ± 0.2	23.8 ± 0.6	10.4 ± 0.2	1.55 ± 0.16	1.63 ± 0.03
4D23/3	1.80	37.5 ± 2.1	15.5 ± 0.4	26.4 ± 0.6	8.7 ± 0.1	1.42 ± 0.09	1.78 ± 0.05
/4	1.84	34.4 ± 1.5	15.1 ± 0.3	23.1 ± 1.2	8.6 ± 0.1	1.49 ± 0.10	1.76 ± 0.04
/5	1.78	32.1 ± 1.8	15.4 ± 0.2	26.7 ± 0.7	8.8 ± 0.1	1.20 ± 0.07	1.75 ± 0.04
3S37/4	1.69	24.2 ± 1.4	14.2 ± 0.4	17.6 ± 1.0	7.3 ± 0.2	1.38 ± 0.11	1.95 ± 0.12
3W29/8	1.27	37.2 ± 0.7	15.8 ± 0.8	25.7 ± 1.7	9.0 ± 0.5	1.45 ± 0.10	1.76 ± 0.14
3U23/4	1.60	25.9 ± 3.0	14.8 ± 0.7	19.1 ± 1.7	8.2 ± 0.4	1.36 ± 0.20	1.80 ± 0.13

All results quoted ± 1 standard deviation.

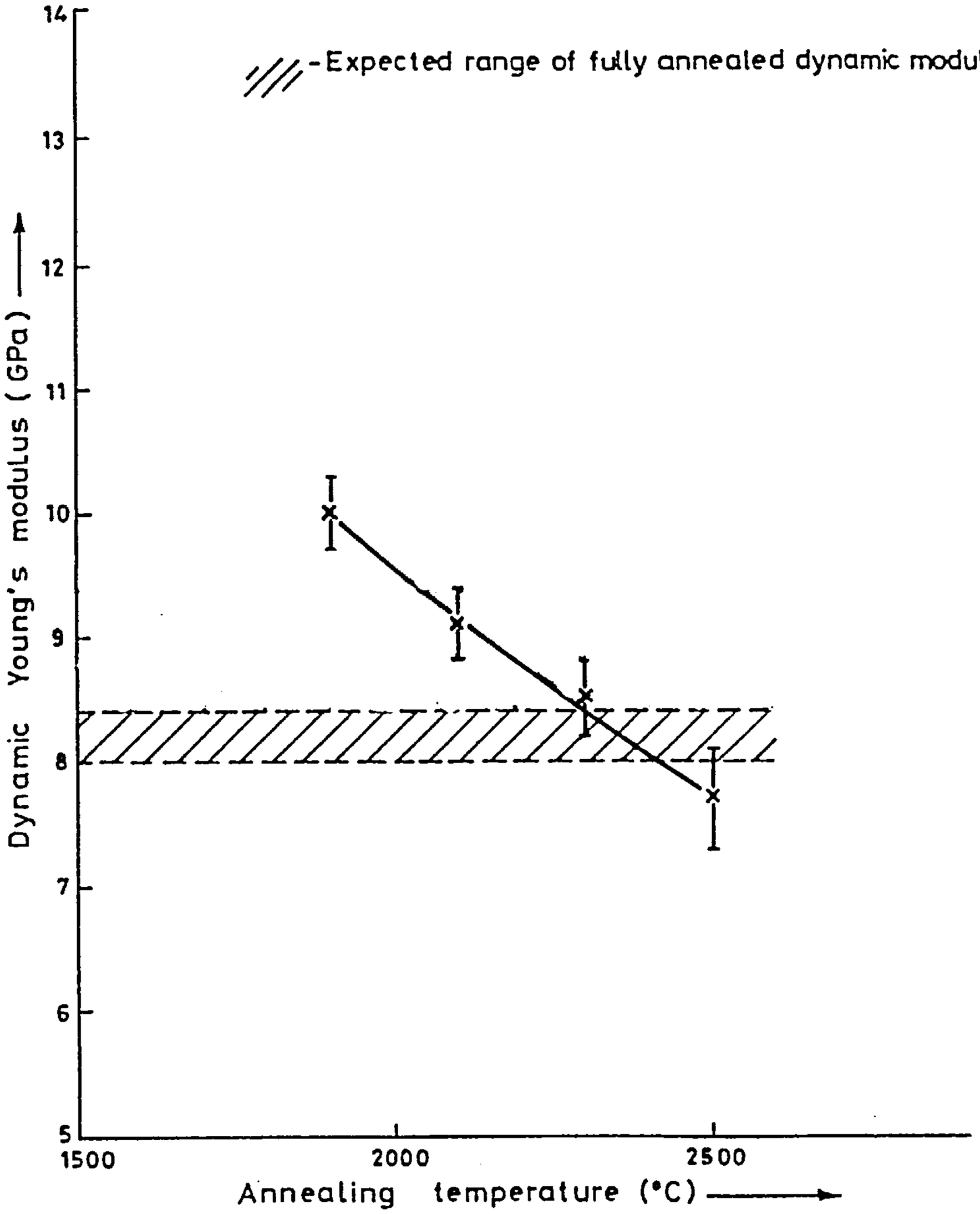

Figure 7.3: Values of dynamic modulus after annealing at temperatures between 1900°C and 2500°C for one hour.

modulus of individual samples could not be measured prior to irradiation as the component would then have been violated before use. Therefore average virgin properties, adjusted for the effects of radiolytic oxidation, are the best available guide to the achievement of full annealing. From Figure 7.3 the optimum temperature is suggested to be 2350^{o}C. This is in agreement with other investigators (Birch and Brown, 1983) and all subsequent anneals were done at this temperature.

The length increase expected on over-annealing is of the order of 0.1% (Brocklehurst et al., 1970). As the specimens were cut remotely, their length could not be measured with sufficient precision to detect any such change after annealing. However, the modulus does continue to decrease below the virgin value indicating a thermally induced change in structure. Using the experimental curve of Figure 7.3, anneals at any temperature within the range 1900 - 2500^{o}C may be adjusted to give equivalent values at an annealing temperature of 2350^{o}C. This gives a comparable measurement of modulus for all annealed specimens.

7.4 Results and Discussion

Table 7.2 lists all measurements made. With the exception of component 3U23/4 from which 30 specimens were available as above, 12 specimens were cut from each component. In the as-received state, the dynamic modulus E, of each specimen in the set of 12 was determined and 6 were then broken in three-point bend and the failure stress σ, recorded. The remaining 6 were annealed for one hour and the dynamic modulus E_{ox} and three-point bend strength σ_{ox} determined. Both as-received and annealed specimens from the same component have identical amounts of radiolytic oxidation such that the effect of fast neutron irradiation alone on strength and modulus is given by the ratios (σ/σ_{ox})

and (E/E_{ox}) respectively. These ratios are listed in Table 7.2 and plotted on Figure 7.4. Standard deviations of low dose strength measurements have been omitted from the figure for clarity but may be read from the table. The solid line (E/E_{ox}) drawn on the figure has been deduced from samples irradiated at doses up to 4×10^{21} n/cm^2 in an accelerated test reactor (Birch and Brown, 1983). The measured moduli agree well with this curve confirming that the component performance in reactor is as expected. The strength ratios are widely scattered particularly for the low dose irradiations. Drawn on the figure is the ratio $(E/E_{ox})^{\frac{1}{2}}$ which strength measurements follow if the constant elastic strain energy at fracture criterion is valid. Table 7.1 indicates that this relation is expected as the irradiation temperature was 400^{o}C. Most of the strength data lie above the $(E/E_{ox})^{\frac{1}{2}}$ curve but three results lie below the curve. The low point at 0.80×10^{21} n/cm^2 is a consequence of the large uncertainty in σ_{ox}, which from Table 7.2 is 35.8 ± 12.6 MPa. The six samples tested gave three very high and three very low strength results. It is possible that this arose from the nature of the three-point bend test such that the unique position of maximum tensile stress coincided with a particularly strong or weak area of the graphite. Only by testing more specimens could a greater precision in σ_{ox} be obtained, but unfortunately none were available. The other two low (σ/σ_{ox}) points are a consequence of higher σ_{ox} values than the norm rather than low σ values such that no serious in-reactor weakening is indicated. In all three low (σ/σ_{ox}) cases the respective values of (E/E_{ox}) are in agreement with all other data, so lending support to the above explanation of greater scatter in strength measurements. However, it may be concluded that the $(E/E_{ox})^{\frac{1}{2}}$ curve is a reasonable representation of the strength variation due to fast neutron

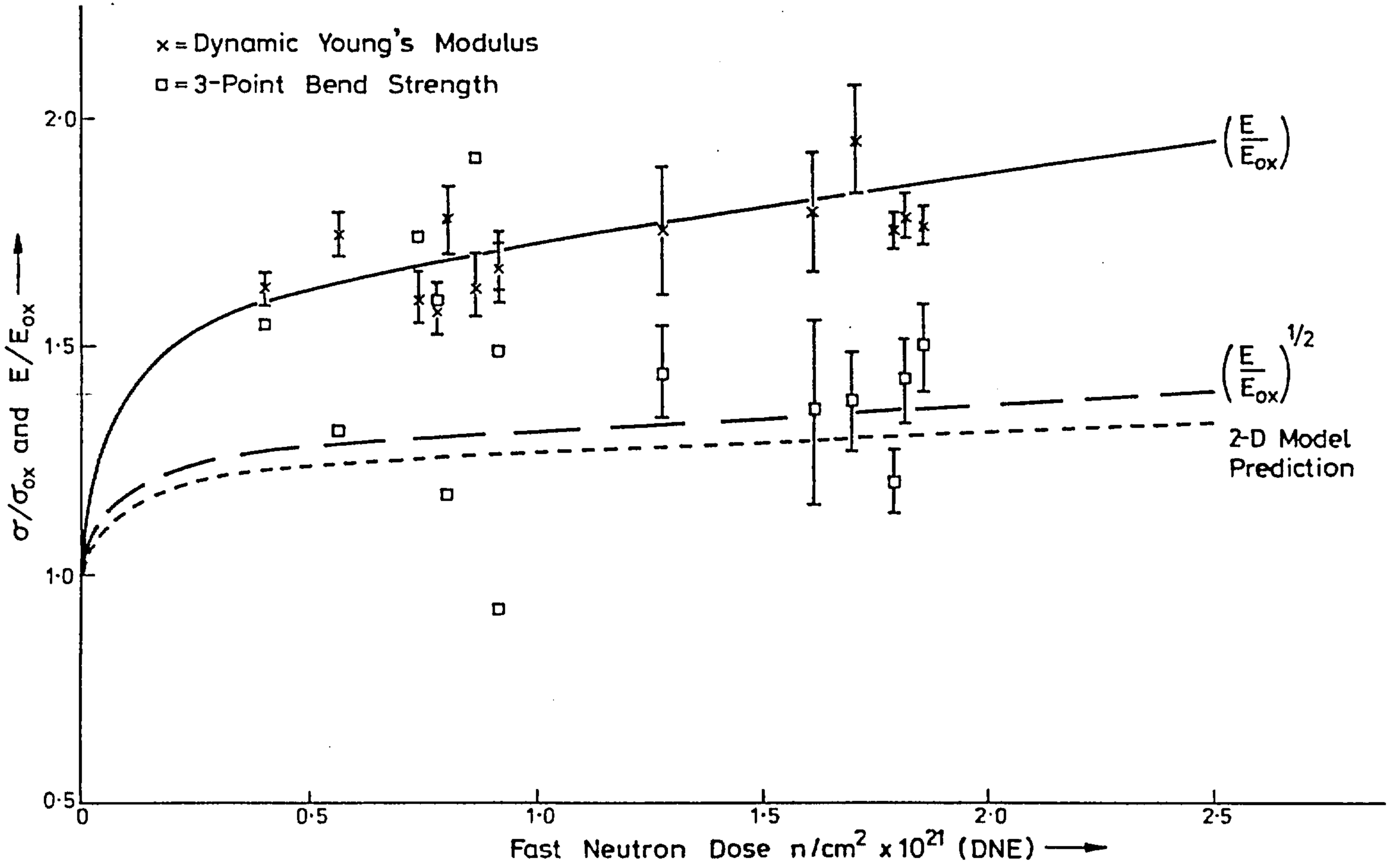

Figure 7.4: A comparison of measured and predicted fractional changes in Young's modulus and bend strength due to fast neutron irradiation alone.

irradiation alone, with provisos on the small number of specimens tested and the large scatter in the data.

7.5 Application of Two-Dimensional Model

The input parameters for virgin pitchcoke are shown in Figure 5.4 and it is by considering changes in these that the two-dimensional model may be applied to the irradiated results.

No measurements of the critical stress intensity factor K_{Ic} of irradiated material have been made. In principle, the method of section 6.4 may be applied to bend tests on notched and un-notched beams to determine the additional crack length a_1, as a function of fast neutron dose and hence deduce K_{Ic}. Such experiments on notched irradiated beams are high on the priority list of future work.

All the dose range considered is in the region of dimensional shrinkage in which the maximum pore size is expected to remain constant. Therefore, if a correlation exists between a_1 and the maximum pore size, a_1 will also remain unchanged. However, radiolytic oxidation, although preferentially attacking small pores, may lead to a continuous slight increase in a_1. In the absence of experimental data, the best assumption is that a_1 is constant and that the change in K_{Ic} on irradiation is the same as the change in strength, that is K_{Ic} is proportional to $\sqrt{E}$. This implies that the effective surface energy γ (equation 2.4) is constant.

Other input parameters are now considered. The increase in fractional porosity may be readily included in the model, the resultant fall in predicted mean fracture stress being as in Figure 5.4. Acoustic emission measurements on several specimens at doses $< 1 \times 10^{21}$ n/cm^2 show no effect of irradiation on particle cleavage stress. It therefore remains at 4.5 MPa. Particle radius is also taken to be constant at 0.5 mm.

The resultant two-dimensional model prediction of mean failure stress is shown on Figure 7.4 and is seen to fall just below the $(E/E_{ox})^{\frac{1}{2}}$ line. The porosity variation is a second order effect and has only a small influence on the prediction. As is the case for virgin material, K_{Ic} is the dominant variable. From Figure 5.4, a given percentage increase in K_{Ic} produces a slightly lower percentage increase in mean failure stress and this explains why the model prediction is slightly lower than the $(E/E_{ox})^{\frac{1}{2}}$ curve. However, with this simple approach the agreement of theory and experiment is promising and is to be investigated further by experimental measurement of K_{Ic}.

7.6 Conclusions

The variation of dynamic Young's modulus and three-point bend strength with fast neutron dose to 1.84×10^{21} n/cm^2 (DNE) for pitchcoke graphite has been determined. The modulus change is in agreement with accelerated test reactor results and the strength change is reasonably represented by the square root of the modulus change, indicating fracture occurs at constant elastic strain energy.

The two-dimensional model of previous chapters has been applied to predict mean failure strength as a function of neutron dose assuming that K_{Ic} is proportional to $\sqrt{E}$. The model predicts a strength increase slightly less than the $(E/E_{ox})^{\frac{1}{2}}$ curve but the strength data show too much scatter to enable a distinction between the two predictions to be made. Further experiments on irradiated beams of pitchcoke graphite containing sharp notches are necessary to determine the variation of additional crack size with irradiation and hence establish the variation of K_{Ic} as a function of irradiation dose.

CHAPTER 8

CONCLUSIONS AND FURTHER WORK

At the outset, the objective of this thesis was defined as being to contribute to the prediction of graphite fracture under general loading. What has been achieved is the development of a model of fracture which is capable of explaining behaviour in bend and tensile tests. The model is applicable to un-notched or sharply notched beams and explains the observed fractional change in flexural strength of pitchcoke graphite on irradiation. Most importantly, the methodology used, in principle, permits prediction of component fracture probabilities.

The model may be criticised for its simplicity. It has been tested against literature data in a wide variety of stress conditions and while it has generally performed well, this exacting assessment has indicated several areas where improvement is required. These may be listed as follows.

(i) The predicted distribution of strengths from a number of identical specimens subjected to the same mechanical test is underestimated. This is perhaps to be expected as only a single value of each input parameter is considered. In practice there is a distribution of pore and particle sizes, cleavage stresses and critical stress intensity factors. Pickup et al. (1981) incorporated a ± 5% random variation in input values to the Buch model. This empirical method could be refined by basing the variation in each parameter on experimental observation, for example by use of quantitative image analysis to determine pore size distributions and preferred shape and orientation of pores.

(ii) The volume dependence of strength at low specimen volumes is not well predicted. There is no weakening mechanism in the model to

account for this 'particle size' effect, as it is assumed that cleavage of a particle does not enhance the stress on its neighbours. In the real material there is a redistribution of stress following each cleavage event. If there is only a small number of particles present the cleavage probability of any particle will be significantly increased on failure of one of its neighbours. A treatment of such crack interactions is a priority in further development of the fracture model.

(iii) The approach to fracture from a sharp notch is not ideal. The acoustic emission evidence obtained indicates that there is sub-critical cracking during bend tests on notched beams. This cracking must necessarily change the stress distribution ahead of the notch, but in the analysis of Chapter 6 only an initial stress distribution is considered. Again a treatment of crack interactions is required.

(iv) There is a difficulty in extending the treatment of fracture at a sharp notch to a general component. Using the method of Chapter 6, the elastic stress distribution is modified to reduce the high theoretical stress concentration immediately below the notch root to a lower, experimental value of average stress concentration. However, it is impracticable to determine the average stress concentration factor in an actual component under operating stresses. A pessimistically high value could be assumed but this would result in an over-conservative failure prediction with consequent loss of operating margins. Again, a model based on crack interactions and a stress distribution obtained from finite element methods, taking account of extension of the notch prior to failure, may solve this problem.

(v) There is an incomplete understanding of the highest ranked variable in the model, the critical stress intensity factor. From

microstructural observation, fracture proceeds by easy cleavage of particles well orientated to the applied stress, followed by considerable tearing through the finely graphitised binder to link up cracked particles. The energy required for this tearing is included implicitly in the value of K_{Ic}. There is scope for improving the representation of microstructure in the model and placing less reliance on, or obtaining a better physical understanding of, K_{Ic}.

(vi) Only a random distribution of cleavage planes has been considered to date. Buch (1976) in his model of tensile failure included basal plane orientation functions to represent material texture. An analysis of this type could be incorporated into the model to predict anisotropy of strength.

Nevertheless, the fracture model developed is most versatile. It is feasible to extend the treatment to cover fracture in compression. Particle failure would then occur due to the resolved shear stress on the cleavage plane. Another common stress state which may be studied with the model is tension or bending with an imposed hydrostatic pressure. Thus the ideal model would predict fracture probabilities in any stress distribution.

There is also more experimental work required. Three items which have been mentioned earlier in the text are further investigation of the variation of four-point bend strength with stress gradient, tensile tests on notched beams and determination of K_{Ic} from notched beams of irradiated pitchcoke. In addition, the following areas may be identified.

(i) Extension of irradiated pitchcoke strength and Young's modulus data to higher fast neutron doses.

(2) Quantitative image analysis of virgin graphites to determine size, shape and orientation of pores and particles.

(3) Optical metallography and study of preferred crack growth directions in bend tests on irradiated pitchcoke. This is to determine the effects of neutron irradiation and radiolytic oxidation on the mechanism of failure.

All these are currently being tackled as part of a joint project between the University of Bath and Berkeley Nuclear Laboratories. The combined theoretical and experimental approach will be maintained to extend the understanding of graphite fracture under different stress conditions.

REFERENCES

Adam R.W. and Brocklehurst J.E., (1983). Mechanical tests on graphite with simulated oxidation gradients. Proc. 16th Biennial Conference on Carbon, San Diego, pp 398-399.

ASTM, (1984). Standard method of test for moduli of elasticity and fundamental frequencies of carbon and graphite materials by sonic resonance. C747-74.

Batdorf S.B. and Crose J.G., (1974). A statistical theory for the fracture of brittle structures subjected to non-uniform polyaxial stresses. J. Applied Mechanics, 41, 459-464.

Bazaj D.K. and Cox E.E., (1969). Stress concentration factors and notch-sensitivity of graphite. Carbon, 7, 689-697.

Birch M. and Bacon D.J., (1983). The effect of fast neutron irradiation on the compressive stress-strain relationships of graphite. Carbon, 21, No.5, 491-496.

Birch M. and Brocklehurst J.E., (1983). The impact endurance of polycrystalline graphite. Carbon, 21, No.5, 497-510.

Birch M., Brocklehurst J.E., Miller W.N. and Kelly B.T., (1982). UKAEA internal document.

Birch M. and Brown R.G., (1983). Impact tests on irradiated graphites. Proc. 16th Biennial Conference on Carbon, San Diego, pp 542-543.

Birch M., Brown R.G. and Brocklehurst J.E., (1983). Defining the inherent defect size of graphite for fracture mechanics applications. Proc. 16th Biennial Conference on Carbon, San Diego, pp 404-405.

Brocklehurst J.E., (1974). Fracture in polycrystalline graphite. Chemistry and Physics of Carbon eds. P.L. Walker Jr. and P.A. Thrower, 13, pp 145-283, New York, Dekker.

Brocklehurst J.E., Birch M. and Kelly B.T., (1983). Factors determining the irradiation shrinkage of graphite to high doses. Proc. 16th Biennial Conference on Carbon, San Diego, pp 546-547.

Brocklehurst J.E., Brown R.G., Gilchrist K.E. and Labaton V.Y., (1970). The effect of radiolytic oxidation on the physical properties of graphite. J. Nuclear Materials, 35, 183-194.

Brocklehurst J.E. and Darby M.I., (1974). Concerning the fracture of graphite under different test conditions. Materials Science and Engineering, 16, 91-106.

Brocklehurst J.E. and Kelly B.T., (1979). Graphite structure and its relation to mechanical engineering design. Proc. 'Mechanical Behaviour of Graphite for HTRs', Gif-sur-Yvette, pp 42-50.

Brocklehurst J.E., Kelly B.T. and Gilchrist K.E., (1981). The effect of substitutional boron on irradiation damage in graphite. Chemistry and Physics of Carbon eds. P.L. Walker Jr. and P.A. Thrower, 17, pp 175-231, New York, Dekker.

Broutman L.J., Krishnakumar S.M. and Mallick P.K., (1970). Effects of combined stresses on alumina and graphite. J. American Ceramic Society, 53, No. 12, 649-654.

Brown W.F. and Srawley J.E., (1966). Plane strain crack toughness testing of high temperature materials. ASTM Special Technical Publication 410.

Burchell T.D., (1984). The effects of radiolytic oxidation on the mechanical properties and fracture of C.A.G.R. outer fuel sleeve graphite. MSc to PhD Transfer Report, University of Bath.

Burchell T.D., Cooke R.G., McEnaney B. and Pickup I., (1984). Acoustic emission - the effect of texture. Proc. 'Carbone '84', Bordeaux, pp 110-111.

Buch J.D., (1976). Mechanical behaviour model for graphites. In: Properties Related to Fracture Toughness. ASTM Special Technical Publication 605, pp 124-144.

Buch J.D., (1982). Fracture mechanics of nuclear graphite. Aerospace Report No. ATR-81(7750)-1.

Carpenter E.W. and Norfolk D.J., (1984). Lattice of power: graphite core life. Nuclear Energy, 23, No.2, 83-96.

Chapman E.S., (1982). UKAEA internal document.

Chell G.G., (1977). FRACPAC: A computer program for calculating elastic and post-yield fracture mechanics parameters. CEGB Report No. RD/L/N/170/77.

Cooke R.G., (1978). Brittle fracture of polyphase ceramics. Science of Ceramics, 9, 527-534.

Cords H., Kleist G., Monch J., Schuster W. and Zimmermann R., (1977). A contribution to fracture criteria for graphite. Proc. 4th SMIRT Conference, San Francisco, D5/f, 1-12.

Corum J.M., (1967). A determination of the fracture toughness of EGCR-type AGOT graphite. J. Nuclear Materials, 22, 41-54.

Darby M.I., (1976). A fracture mechanics approach to the failure of graphite in laboratory tests. International J. of Fracture, 12, No.5, 745-757.

Darby M.I., (1978). Effect of stress gradient on the fracture of graphite. Engineering Fracture Mechanics, 10, 687-688.

Davidge R.W. and Tappin G., (1968). The effective surface energy of brittle materials. J. Materials Science, 3, 165-173.

Diefendorf R.J., (1959). The effect of atmosphere on the strength of graphite. Proc. 4th Carbon Conference, Buffalo, pp 489-496.

Ely R.E., (1968). Strength of magnesium silicate and graphite under biaxial stresses. Ceramic Bulletin, 47, No.5, 489-492.

Engle G.B., Price R.J., Johnson W.R. and Beavan L.A., (1974). Properties and irradiation behaviour of near-isotropic graphites for large HTGRs. Proc. 4th London Carbon Conference, Paper 20, pp 757-768.

Eto M., (1975). The residual strain of polycrystalline graphite (II). J. Nuclear Materials, 57, 205-211.

Eto M. and Oku T., (1975). The residual strain of polycrystalline graphite (I). J. Nuclear Materials, 57, 198-204.

Evans A.G., (1976). On the formation of a crack tip microcrack zone. Scripta Metallurgica, 10, 93-97.

Everett M.R. and Ridealgh F., (1972). The stress-strain characteristics of non-irradiated and irradiated nuclear graphites. Proc. Carbon '72, Baden-Baden, pp 191-193.

Fitzer E., Mueller K. and Schaeffer W., (1971). The chemistry of the pyrolytic conversion of organic compounds to carbon. Chemistry and Physics of Carbon eds. P.L. Walker Jr. and P.A. Thrower, 7, pp 237-383, New York, Dekker.

Gilchrist K.E. and Wells D., (1969). Acoustic emission from graphite under stress. Carbon, 7, 627-631.

Gillin L.M., (1967). Deformation characteristics of nuclear grade graphites. J. Nuclear Materials, 23, 280-288.

Glendinning A. and Stacey R.D., (1981). UKAEA internal document.

Green L., (1951). The behaviour of graphite under alternating stress. J. Appl. Mech., 18, pp 345-348.

Green W.V., Weertman J. and Zukas E.G., (1970). High temperature creep of polycrystalline graphite. Materials Science and Engineering, 6, No.3, 199-211.

Griffith A.A., (1920). The phenomena of rupture and flow in solids. Phil. Trans. Roy. Soc. A 221, 163-198.

Ho F., (1979). A four parameter Weibull theory for the strength of granular brittle material. Proc. 14th Biennial Conference on Carbon, Penn. State, pp 338-339.

Hoagland R.G., Embury J.D. and Green D.J., (1975). On the density of microcracks formed during the fracture of ceramics. Scripta Metallurgica, 9, 907-909.

Jenkins G.M., (1962). Fracture in reactor graphite. J. Nuclear Materials, 5, 280-286.

Jenkins G.M., (1973). Deformation mechanisms in carbons. Chemistry and Physics of Carbon eds. P.L. Walker Jr. and P.A. Thrower, 11, pp 189-242, New York, Dekker.

Jortner J., (1972). Biaxial mechanical properties of AXF-5Q graphite to 4000^{o}F. Proc. Conference on continuum aspects of graphite design, Gatlinburg, pp 514-532.

Kelly B.T., (1978). Radiation damage in graphite and its relevance to reactor design. Progress in Nuclear Energy, 2, 219-269.

Kelly B.T., (1981). Physics of Graphite. London, Applied Science Publishers.

Kelly B.T. and Brocklehurst J.E., (1977). UKAEA reactor group studies of irradiation-induced creep in graphite. J. Nuclear Materials, 65, 79-85.

Kennedy C.R., (1983). The effect of steam oxidation on the fracture mechanics of graphite. Proc. 16th Biennial Conference on Carbon, San Diego, pp 396-397.

Kennedy C.R., Engle G.B., Price R.J. and Morris E.G., (1984). Correlation between tensile strength and sonic attenuation in a structural graphite. Proc. 'Carbone '84', Bordeaux, pp 98-99.

Knibbs R.H., (1967). Fracture in polycrystalline graphite. J. Nuclear Materials, 24, 174-187.

Kraus G. and Semmler J., (1978). Characterising the mechanical properties of carbon and graphite materials using acoustic emission analysis methods (in German). Carbon, 16, 185-190.

Liu H.W., (1982). On the fundamental basis of fracture mechanics. Engineering Fracture Mechanics, 17, No.5, 425-438.

Logsdail D.H., (1968). The effect of gaseous environment on the flexural strength of graphite. AERE Report 5721.

Losty H.H.W. and Orchard J.S., (1962). The strength of graphite. Proc. 5th Carbon Conference, Penn. State, pp 519-532.

Lungagnani V. and Krefeld R., (1972). Statistical considerations on the strength of nuclear graphites: characterisation, irradiation and design. Proc. Conference on Continuum Aspects of Graphite Design, Gatlinburg, pp 663-675.

Marsh H., (1978). In: Analytical methods for coal and coal products. Ed. C. Karr, New York Academic Press.

Marshall P. and Priddle E.K., (1973a). The influence of specimen size and mode of loading on the fracture of graphite. Carbon, 11, 627-631.

Marshall P. and Priddle E.K., (1973b). Room temperature fatigue crack propagation in reactor graphites. Carbon, 11, 541-546.

Matthews R.B., (1974). Statistical aspects of fracture of irradiated graphite. J. American Ceramic Society 57, No.5, 225-226.

Metcalfe M.P., (1981). Mechanical properties of Dungeness 'B' moderator graphite. CEGB Report SE/SSD/M/81/056.

Metcalfe M.P., (1982). Modelling of radiolytically corroded commercial AGR graphite fuel bricks. Nuclear Energy, 21, No.1, 57-62.

Meyer R.A., Zimmer J.E. and Almon M.C., (1974). Micromechanics of failure in carbon systems. Aerospace Report No. ATR-74(7408)-2.

Mrozowski S., (1956). Mechanical strength, thermal expansion and structure of cokes and carbons. Proc. 1st and 2nd Conf. on Carbon, Buffalo, pp 31-45.

Pickup I.M., (1984). The influence of thermal corrosion upon the mechanical properties of nuclear graphites. PhD Thesis, University of Bath.

Pickup I.M., Cooke R.G. and McEnaney B., (1981). The influence of thermal corrosion upon the fracture of nuclear graphites. Proc. 15th Biennial Conference on Carbon, Philadelphia, pp 556-557.

Pickup I.M., McEnaney B. and Cooke R.G., (1982). Fracture processes in thermally oxidised nuclear graphites. Proc. Carbon '82, London, pp 320-322.

Platonov P.A., Virgil'ev Y.S., Karpukhin V.I., Zaitsev A.L. and Novobratskaya I.F., (1973). Changes in the strength characteristics of graphite due to neutron irradiation. Soviet Atomic Energy, 35, No.3, 805-808.

Price R.J., (1975). Mechanical properties of graphite for high temperature gas-cooled reactors: a review. General Atomic Report GA-A13524 UC-77.

Price R.J., (1976). Statistical study of the strength of near isotropic graphite. General Atomic Report GA-A13955 UC-77.

Prince N., (1979). Technology of graphite moderator structures. Nuclear Energy, 18, No.4, 267-275.

Prince N. and Rossiter F., (1982). UKAEA internal document.

Ragan S. and Marsh H., (1983). Review: science and technology of graphite manufacture. J. Materials Science, 18, 3161-3176.

Rodig M., Kleist G., Schiffers H. and Nickel H., (1978). Fracture mechanical behaviour of reactor graphite. Proc. 5th London Carbon Conference, pp 51-62.

Roscoe C. and Thomas J.M., (1966). The identification and some physico-chemical consequences of non-basal edge and screw dislocations in graphite. Proc. Royal Society A297, 397-407.

Rose A.P.G. and Tucker M.O., (1982). A fracture criterion for nuclear graphite. J. Nuclear Materials, 110, Nos. 2 and 3, 186-195.

Rowe G.H., (1962). High temperature strength of clean graphite. Nuclear Engineering, 7, 102-103.

Sakai M., Bradt R.C. and Fischbach D.B., (1984). Fracture toughness of pyrolytic carbon. Proc. 'Carbone '84', Bordeaux, pp 122-123.

Sato S., Awaji H. and Akuzawa H., (1978). Fracture toughness of reactor graphite at high temperature. Carbon, 16, No.2, 95-102.

Sato S. and Miyazono S., (1964). Studies of elastic modulus of irradiated graphite by an ultrasonic pulse method. Carbon, 2, 103-114.

Smith A., (1982). CEGB unpublished work.

Smith M.C., (1964). Effects of temperature and strain rate on transverse tensile properties of H4LM graphite tested in helium and in vacuum. Carbon, 1, 147-153.

Smith M.C., (1972). The deformation and fracture mechanisms in polycrystalline graphites. Proc. Conference on continuum aspects of graphite design, Gatlinburg, pp 475-481.

Stephen W., (1984). The inhibition by carbon monoxide of the reaction between graphite and carbon dioxide at high pressures. PhD Thesis, University of Bath.

Stevens R., (1971). Fracture behaviour and electron microscopy of a fine grained graphite. Carbon, 9, 573-578.

Taylor R., Brown R.G., Gilchrist K., Hall E., Hodds A. T., Kelly B.T. and Morris F., (1967). The mechanical properties of reactor graphite. Carbon, 5, 519-531.

Timoshenko S. and Goodier J.N., (1951). 'Theory of Elasticity', 2nd Edition, McGraw Hill, New York, p 61.

Tucker M.O., (1979). The application of fracture mechanics to the notch sensitivity of graphite. Proc. 'Mechanical Behaviour of Graphite for HTRs', Gif-sur-Yvette, pp 88-96.

Tucker M.O. and Webster S.J., (1982). The impact resistance of CAGR graphite sleeves. Proc. 'Gas Cooled Reactors Today', British Nuclear Energy Society, London.

Turnbull J.A. and Stagg M.S., (1966). Isothermal annealing studies on vacancy and interstitial loops in single crystal graphite. Phil. Mag., 14, No.131, 1049-1066.

Turner C.E., (1973). Fracture toughness and specific fracture energy: a re-analysis of results. Materials Science and Engineering, 11, 275-282.

Tzung F.K., Kao B., Ho F. and Tang P., (1981). The effect of couple-stress on the pure bending of a prismatic bar. Proc. 6th SMIRT Conf., Paris, Paper L3/6.

von Mises R., (1928). Mechanik der plastischen formänderung von kristallen. Zeitschrift für Angewandte Mathematik und Mechanik, 8, No.3, 161-185.

Watson M.B., (1984). CEGB unpublished work.

Weibull W.J., (1951). A statistical distribution function of wide applicability. Applied Mechanics, 18, 293-297.

Wood C.J. and Wickham A.J., (1980). Graphite oxidation and coolant chemistry in CEGB AGRs. Nuclear Energy, 19, No.4, 277-282.

Yahr G.T. and Valachovic R.S., (1972). Geometrical parameters affecting the fracture toughness of graphite. Proc. Conference on Continuum Aspects of Graphite Design, Gatlinburg, pp 533-546.

Yahr G.T., Valachovic R.S. and Greenstreet B.L., (1973). Deformation and fracture of thin-walled graphite tubes under biaxial states of stress. Proc. 11th Biennial Conference on Carbon, pp 227-228.